NASA
Technical
Paper
2230

February 1984

Wind-Tunnel Free-Flight Investigation of a Model of a Forward-Swept-Wing Fighter Configuration

Daniel G. Murri,
Luat T. Nguyen,
and Sue B. Grafton

NASA

NASA
Technical
Paper
2230

1984

Wind-Tunnel Free-Flight Investigation of a Model of a Forward-Swept-Wing Fighter Configuration

Daniel G. Murri,
Luat T. Nguyen,
and Sue B. Grafton

Langley Research Center
Hampton, Virginia

National Aeronautics
and Space Administration

**Scientific and Technical
Information Branch**

SUMMARY

A wind-tunnel free-flight investigation was conducted to study the stability and control characteristics of a model of a forward-swept-wing fighter-airplane configuration at high angles of attack. Other wind-tunnel techniques employed in the study included static- and dynamic- (forced-oscillation) force tests, free-to-roll tests, and flow-visualization tests. A unique facet of the study was the extreme level of static pitch instability (in excess of negative 32-percent static margin) inherent in the airframe design which precluded free-flight testing without stability augmentation in pitch.

The results of the captive (fixed model) wind-tunnel tests indicated that the lateral-directional stability characteristics of the model were determined primarily by the forward-swept wing and vertical tail at low to moderate angles of attack and by the fuselage forebody at the higher angles of attack. However, component interactions were also found to influence these characteristics significantly.

The results of the free-flight study showed that with stability augmentation in the pitch, roll, and yaw axes, the model exhibited good dynamic stability characteristics up to 40° angle of attack, above which the free-flight tests could not be conducted because of lack of yaw-control effectiveness. The pitch stability augmentation system (SAS) was found to be effective in providing the required level of stability as long as there was sufficient pitch control available. With the roll SAS deactivated, the model exhibited large-amplitude undamped roll oscillations (wing rock) above 25° angle of attack. The roll SAS acting through the powerful flaperons effectively suppressed the wing rock throughout the test angle-of-attack range.

INTRODUCTION

The potential advantages of the forward-swept wing have been known for some time. However, application of the concept has not been practical because of the structural weight penalty required to overcome the aeroelastic divergence problem. Recent advances in composite materials and aeroelastic tailoring indicate that a forward-swept wing can now be built with little or no weight penalty. (See ref. 1.) To explore this promising new technology, the Defense Advanced Research Projects Agency (DARPA) has sponsored the development of a research airplane (designated as the X-29A) to demonstrate by flight tests the application of the forward-swept-wing concept to a fighter-class airplane.

As a part of the effort in developing forward-swept-wing technology, DARPA, the Grumman Aerospace Corporation, and the Langley Research Center are involved in a broad cooperative research program to investigate the high-angle-of-attack, stall, and spin characteristics associated with this advanced airplane-design concept. A primary objective is to determine how these characteristics are influenced by the unique stall progression of the forward-swept wing. Other objectives of the program are to study the effects of several other interesting features of the design including: (1) a very high level of airframe static pitch instability, (2) a fuselage forebody tailored for high-angle-of-attack directional stability, (3) a close-coupled

canard with large-deflection capability, (4) full-span flaperons, and (5) an aft-fuselage strake flap for pitch-control augmentation.

The present wind-tunnel free-flight investigation was conducted to determine the stability and control characteristics of the X-29A configuration in the low-speed, high-angle-of-attack (α) range up to the stall ($\alpha \approx 40°$). The study involved wind-tunnel tests of a 0.16-scale model and included static- and dynamic- (forced-oscillation) force tests, free-to-roll tests, flow-visualization tests, and free-flight tests. Results are presented which emphasize the component effects of the various design features on the high-angle-of-attack aerodynamics and the resulting flight characteristics.

SYMBOLS

All longitudinal aerodynamic coefficients are referred to the stability-axis system, and all lateral-directional data are referred to the body-axis system. (See fig. 1.) All force-test data are referred to a moment reference center located 7 percent in front of the wing mean aerodynamic chord.

b wing span, ft

C_A axial-force coefficient, $\frac{\text{Axial force}}{q_\infty S}$

C_D drag coefficient, $\frac{\text{Drag}}{q_\infty S}$

C_L lift coefficient, $\frac{\text{Lift}}{q_\infty S}$

C_l rolling-moment coefficient, $\frac{\text{Rolling moment}}{q_\infty Sb}$

C_m pitching-moment coefficient, $\frac{\text{Pitching moment}}{q_\infty S\bar{c}}$

C_N normal-force coefficient, $\frac{\text{Normal force}}{q_\infty S}$

C_n yawing-moment coefficient, $\frac{\text{Yawing moment}}{q_\infty Sb}$

C_Y side-force coefficient, $\frac{\text{Side force}}{q_\infty S}$

c chord line, ft

$\bar{c}$ mean aerodynamic chord, ft

f frequency of oscillation, Hz

g acceleration due to gravity, 32.152 ft/sec^2

I_X, I_Y, I_Z	moments of inertia about X, Y, and Z axes, respectively, slug-ft^2
j	imaginary number, $(-1)^{1/2}$
K_{ARI}	aileron-to-rudder interconnect gain
K_p	roll-rate feedback gain to aileron, sec
K_{pr}	roll-rate feedback gain to rudder, sec
K_q	pitch-rate feedback gain to canard, sec
K_r	yaw-rate feedback gain to rudder, sec
K_α	angle-of-attack feedback gain to canard
k	reduced-frequency parameter, $\omega b/2V$ or $\omega \bar{c}/2V$
p	roll rate, rad/sec
q	pitch rate, rad/sec
q_∞	free-stream dynamic pressure, lb/ft^2
r	yaw rate, rad/sec
S	wing reference area, ft^2
t	time, sec
$t_{1/2}$	time to one-half amplitude, sec
t_2	time to double amplitude, sec
V	free-stream velocity, ft/sec
X, Y, Z	body reference axes
α	angle of attack, deg
$\dot{\alpha}$	rate of change of angle of attack, rad/sec
β	angle of sideslip, deg
$\dot{\beta}$	rate of change of angle of sideslip, rad/sec
ΔC_l	incremental rolling-moment coefficient
ΔC_n	incremental yawing-moment coefficient
ΔC_Y	incremental side-force coefficient
$\Delta\theta$	amplitude of pitch oscillation, deg
$\Delta\phi$	amplitude of roll oscillation, deg

$\Delta\psi$ amplitude of yaw oscillation, deg

δ_a effective aileron-deflection angle, $\frac{\delta_{f,right} - \delta_{f,left}}{2}$, deg

δ_c canard incidence, positive with trailing edge down, deg

$\delta_{c,t}$ canard incidence required for trim, deg

δ_f flaperon-deflection angle, positive with trailing edge down, deg

δ_{ps} pilot stick input, percent of maximum

δ_r rudder-deflection angle, positive with trailing edge left, deg

δ_s strake-flap-deflection angle, positive with trailing edge down, deg

ζ damping ratio, $\sqrt{1 - \omega_d^2/\omega_n^2}$

σ $= \zeta\omega_n$, rad/sec

ω angular frequency, $2\pi f$, rad/sec

ω_d damped frequency, rad/sec

ω_n natural frequency, rad/sec

Stability derivatives:

$$C_{l_\beta} = \frac{\partial C_l}{\partial \beta} \qquad C_{n_\beta} = \frac{\partial C_n}{\partial \beta} \qquad C_{Y_\beta} = \frac{\partial C_Y}{\partial \beta}$$

$$C_{l_{\delta a}} = \frac{\partial C_l}{\partial \delta_a} \qquad C_{n_{\delta a}} = \frac{\partial C_n}{\partial \delta_a}$$

$$C_{l_{\delta r}} = \frac{\partial C_l}{\partial \delta_r} \qquad C_{n_{\delta r}} = \frac{\partial C_n}{\partial \delta_r}$$

$$C_{l_p} = \frac{\partial C_l}{\partial \frac{pb}{2V}} \qquad C_{n_p} = \frac{\partial C_n}{\partial \frac{pb}{2V}} \qquad C_{Y_p} = \frac{\partial C_Y}{\partial \frac{pb}{2V}}$$

$$C_{l_{\dot\beta}} = \frac{\partial C_l}{\partial \frac{\dot\beta b}{2V}} \qquad C_{n_{\dot\beta}} = \frac{\partial C_n}{\partial \frac{\dot\beta b}{2V}} \qquad C_{Y_{\dot\beta}} = \frac{\partial C_Y}{\partial \frac{\dot\beta b}{2V}}$$

$$C_{l_r} = \frac{\partial C_l}{\partial \frac{rb}{2V}} \qquad C_{n_r} = \frac{\partial C_n}{\partial \frac{rb}{2V}} \qquad C_{Y_r} = \frac{\partial C_Y}{\partial \frac{rb}{2V}}$$

$$C_{m_q} = \frac{\partial C_m}{\partial \frac{q\bar{c}}{2V}} \qquad C_{N_q} = \frac{\partial C_N}{\partial \frac{q\bar{c}}{2V}} \qquad C_{A_q} = \frac{\partial C_A}{\partial \frac{q\bar{c}}{2V}}$$

$$C_{m_{\dot{\alpha}}} = \frac{\partial C_m}{\partial \frac{\dot{\alpha}\bar{c}}{2V}} \qquad C_{N_{\dot{\alpha}}} = \frac{\partial C_N}{\partial \frac{\dot{\alpha}\bar{c}}{2V}} \qquad C_{A_{\dot{\alpha}}} = \frac{\partial C_A}{\partial \frac{\dot{\alpha}\bar{c}}{2V}}$$

$$C_{n_{\beta,dyn}} = C_{n_\beta} \cos \alpha - \frac{I_Z}{I_X} C_{l_\beta} \sin \alpha$$

Abbreviations:

ARI	aileron-to-rudder interconnect
c.g.	center of gravity
SAS	stability augmentation system
T.E.D.	trailing edge down
T.E.U.	trailing edge up

MODELS AND TESTING TECHNIQUES

Models

Two models were tested to obtain the data presented in this report: a flat-plate 16-percent-scale model of the X-29A wing planform and a 16-percent-scale model of the complete X-29A (referred to as the basic model). The geometry of the models is presented in figure 2. The flat-plate wing model was constructed of 1/2-in-thick plywood and had a 1/4-in-radius leading edge and a sharp, beveled trailing edge. The basic model was constructed primarily of molded fiberglass and is shown in figure 3. A spin-chute canister that was tested in three locations is shown in figure 4, and a set of 40° nose strakes that was developed during testing is shown in figure 5. These strakes were tested in addition to the standard nose strakes which are labeled in figure 2(b). Presented in table I is a summary of the weight and inertias, geometric characteristics, and control-surface deflections of the basic model.

The longitudinal control surfaces included the canard, wing trailing-edge flaperons, and the fuselage-mounted strake flaps. The canard provided the primary pitch control of the configuration and had a deflection range from -60° to 30°. The strake flaps are designed to augment pitch trim and are deflected to the full

trailing-edge-down position above about 18° angle of attack. In the current investigation, the model was tested with the strake flaps fixed at various deflections. The full-span flaperons were designed to hinge simultaneously at the 75- and 90-percent-chord lines according to the relationship presented in figure 6. With the model in the high-angle-of-attack configuration, the flaperons and strake flaps were deflected to their full-down positions (17.5° and 30°, respectively). However, the data presented on dynamic stability derivatives were measured with the flaperons deflected to 20°. Unless otherwise noted, all data presented in this report were measured with the model in the high-angle-of-attack configuration.

Lateral-directional control was provided by the use of a conventional rudder for yaw control and asymmetrically deflected flaperons for roll control. Since the model was tested in the high-angle-of-attack configuration, the flaperons were at their full-down position (17.5°) and roll control was provided by a single flaperon deflecting up from that position.

Captive Wind-Tunnel Tests

Extensive captive (fixed model) wind-tunnel tests were conducted prior to testing the model in free flight. The purpose of these tests was to define the predominant aerodynamic characteristics of the configuration at high angles of attack and to develop a data base to aid in the analysis of the free-flight test results. These tests included static- and dynamic- (forced-oscillation) force tests, free-to-roll tests, and flow-visualization tests.

The static- and dynamic- (forced-oscillation) force tests were conducted in the Langley 30- by 60-Foot Tunnel at a dynamic pressure of 10 lb/ft^2, corresponding to a wing mean-chord Reynolds number of about 0.68×10^6. In these tests, body-axis forces and moments were measured by using a conventional strain-gage balance and were resolved into the appropriate aerodynamic coefficients. The static-force tests included component buildup tests and measurements of control effectiveness and were made over an angle-of-attack range from -90° to 90° and an angle-of-sideslip range from -30° to 30°. Data are presented in this report over an angle-of-attack range from 0° to 90° and an angle-of-sideslip range from -5° to 5°. To determine the dynamic stability derivatives, forced-oscillation testing was conducted in pitch, roll, and yaw. These measurements were made at an oscillation frequency of 1 Hz which resulted in values of the reduced-frequency parameter k of 0.15 for the rolling and yawing tests and of 0.040 for the pitching tests.

To explore the dynamic roll stability of the model further, a series of wind-tunnel tests were performed with the model mounted on a free-to-roll apparatus. This test technique allowed the model to rotate freely about its roll axis and was used to assess the susceptibility of the configuration to undamped roll oscillations at high angles of attack (wing rock). The data from these tests were primarily qualitative; that is, the observer visually identified the presence and relative magnitude of the oscillations. A more detailed discussion of this test technique is contained in reference 2.

Limited flow-visualization tests were also conducted by using both tuft- and helium-bubble techniques. The tuft techique was used to study surface airflow over the model, whereas the helium-bubble technique was used to study portions of the surrounding flow field. These tests were conducted in the Langley 12-Foot Low-Speed Tunnel.

Free-Flight Tests

The free-flight test technique involves flying the model unrestrained in the open-throat test section of the Langley 30- by 60-Foot Tunnel. A photograph of the model in free flight is shown in figure 7, and a schematic diagram of the test setup is shown in figure 8. Steady 1g flights were made at angles of attack from 13° to 40° by varying the tunnel speed from 96 ft/sec (q = 11 lb/ft^2) to 58 ft/sec (q = 4 lb/ft^2). The model was remotely controlled by three pilots: a roll/yaw pilot, a pitch pilot, and a thrust operator. Pneumatic and electric power and control signals were supplied to the model through a flexible umbilical cord which was made up of wires and light plastic tubes. The umbilical chord also incorporated a 1/8-in-steel safety cable that passed through a pulley above the test section. The safety cable was used to catch the model when an uncontrollable motion or mechanical failure occurred. The entire umbilical cord was kept slack during the flights by a safety-cable operator using a high-speed winch.

The model was instrumented with a three-axis rate gyroscope to measure angular rates and a miniaturized boom-mounted α/β vane sensor (fig. 9) to measure angle of attack and sideslip. These data, along with pilot control inputs and control-surface deflections, were recorded in time-history form on strip-chart recorders. Also, qualitative assessments of the model flight characteristics were taken in the form of motion pictures and pilot comments. The flight-control laws which included stability augmentation in all three axes were programmed into a digital computer which processed sensor data and pilot control inputs to generate command signals to drive the pneumatic control-surface actuators on the model. A more detailed discussion of the free-flight test technique can be found in reference 3.

RESULTS AND DISCUSSION OF CAPTIVE TESTS

Static Longitudinal Characteristics

The static longitudinal characteristics of the configuration are presented in figures 10 to 13. The canard-off data of figure 10 indicate that the wing initially stalled at about 12° angle of attack. The wing stall pattern was visualized by using tufts which showed stalled flow beginning at the wing root and progressing outward with increasing angle of attack. The tufts also indicated that small regions of attached flow were maintained at the wing tips to angles of attack well above that for maximum lift (α = 40°). The pitching-moment data show that the configuration without the canard exhibits neutral to slightly unstable static stability in the angle-of-attack range of primary interest in the free-flight tests (α = 15° to 40°). Except for large positive canard deflections, addition of the canard significantly increases the level of instability for angles of attack up to 30° to 60°, depending on canard incidence. This is followed by a stable break, which occurs at an angle of attack between 35° to 60°, again depending on canard incidence. The data also show the canard to be a very effective pitch-control device over a wide angle-of-attack range by virtue of its large range of travel. As shown in figure 11, the model in the high-angle-of-attack configuration with the c.g. at $-0.07\bar{c}$ can be trimmed through an angle-of-attack range from about 10° to 70°. For the angle-of-attack range of primary interest in the free-flight tests (α = 15° to 40°), trimmed-canard incidence varied from about 5° to -35°.

The data of figures 12 and 13 show the effect of strake-flap and symmetric flaperon deflections. As expected, trailing-edge-down strake-flap deflections increased lift and, because of the long moment arm, generated large nose-down pitching moments.

These devices are shown to provide remarkably constant pitch-control-moment increments across the entire angle-of-attack range. Figure 13 shows that deflecting the flaperons to 17.5° increased lift for angles of attack up to 30° and produced small nose-down pitching moments because of the relatively short moment arm.

Static Lateral-Directional Stability Characteristics

The static lateral-directional stability characteristics of the configuration are presented in figures 14 to 22. The static stability derivatives C_{Y_β}, C_{n_β}, and C_{l_β} were computed using a sideslip range from -5° to 5°. The data of figure 14 indicate that the vertical tail began to lose effectiveness in providing static directional stability $\left(C_{n_\beta}\right)$ at an angle of attack between 20° to 25°, depending on canard incidence. The loss in vertical-tail effectiveness was due to a blanketing effect of the tail in the low-energy stalled wake of the wing. This resulted in near-zero to slightly negative values of static directional stability in the angle-of-attack range from 30° to 40°. Above 40°, however, the data show a strong reestablishment of static directional stability which is obviously not caused by the vertical tail. It was found that this phenomenon was a result of the aerodynamics associated with the long slender forebody with a relatively flat elliptical cross section. At high angles of attack, two strong vortex sheets were shed from the pointed nose. Under sideslip, the leeward vortex was displaced above the nose, whereas the windward vortex was close to the surface. (See fig. 23.) This flow pattern probably produced suction pressures on the windward side of the nose which, acting through the long moment arm, produced the stabilizing yawing moments. This phenomenon was observed in past investigations (refs. 4 and 5, for example) where a similar type of forebody was tested.

Also shown in figure 14 are the static lateral stability $\left(C_{l_\beta}\right)$ characteristics of the configuration. The data indicate a low or unstable dihedral effect up to an angle of attack between about 5° and 10°, but very strong lateral stability at the higher angles of attack. As expected, the vertical tail was stabilizing at low angles of attack before losing effectiveness by $\alpha = 30°$.

A comparison of the lateral stability characteristics of the flat-plate wing model with those of the complete configuration (fig. 15) indicates that the forward-swept wing dominated the static lateral stability characteristics of the complete configuration below about 30° angle of attack. That is, the wing exhibited an unstable dihedral effect because of the negative sweep effect, when experiencing primarily attached flow ($\alpha \lesssim 10°$), and a stable dihedral effect, when separated vortex flow was dominant ($10° \lesssim \alpha \lesssim 30°$). Above 30° angle of attack, component buildup tests indicated that a favorable aerodynamic interaction between the forebody and the canard-wing combination was responsible for the high levels of static lateral stability exhibited.

The effect of canard deflection on the static lateral-directional stability characteristics of the model is presented in figure 16. When deflected to lower settings ($\delta_c = 0°$), the presence of the canard significantly enhanced both lateral and directional stability up to about 30° angle of attack. In this angle-

of-attack range, tuft-flow photographs (fig. 17) indicated that for low deflections, the canard improved the flow field at the vertical tail. At the higher deflections (δ_c = -60°), however, the canard contributed to the blanketing effect of the wing, thus causing a degradation in both lateral and directional stability. Between 30° and 45° angle of attack, the data of figure 16 show that canard deflection primarily affected directional stability. In the angle-of-attack range from 30° to 45°, the lower canard deflections (δ_c = 0° and -25°) resulted in a degradation in directional stability, as compared with the canard-off configuration.

Presented in figures 18 and 19 are the effects of flaperon and strake-flap deflections, respectively, on the static lateral-directional stability characteristics. Symmetric flaperon deflection (fig. 18) is shown to have a minimal effect on both lateral and directional stability. On the other hand, the data of figure 19 indicate that strake-flap deflections have a significant effect on directional stability up to about 55° angle of attack. Below 25° angle of attack, trailing-edge-up strake-flap deflections degraded directional stability characteristics, probably as a result of adverse interference with the vertical-tail flow field. Between 25° and 55° angle of attack, however, trailing-edge-up deflections improved directional stability.

The static stability characteristics of the configuration with the spin-chute canister are presented in figure 20. The data indicate that the spin-chute canister has a minor effect on lateral-directional stability below 45° angle of attack for all three locations tested.

Presented in figure 21 are the effects of adding the 40° nose strakes on the static lateral-directional stability. As will be discussed later, these strakes were developed to increase roll damping in the region of maximum lift. Figure 21 indicates, however, that they have a very detrimental effect on static directional stability. With the 40° nose strakes added, a reduction in directional stability was measured above 5° angle of attack and negative values of C_{n_β} were measured at angles of attack above 20°. This would indicate that the 40° nose strakes inhibited the formation of the directionally stabilizing vortex flow field normally produced by the forebody. Also, a reduction in lateral stability above 50° angle of attack suggests that the 40° nose strakes degrade the favorable flow-field interaction between the forebody and the canard-wing combination.

The effect of the boom-mounted α/β vane sensor (fig. 9) used in the free-flight tests on the static lateral-directional stability is presented in figure 22. The data indicate that the primary effect of the sensor and attachment boom was to degrade slightly the directional stability above 25° angle of attack.

Generally, the results of the static wind-tunnel tests indicate that the lateral-directional stability characteristics of the configuration were not dominated by any one configuration feature throughout the angle-of-attack range. The directional stability was found to be strongly influenced at the lower angles of attack by the vertical tail and canards, whereas the forebody design was found to dominate at high angles of attack. The forward-swept wing was primarily responsible for the lateral stability characteristics up to about 30° angle of attack; however, the characteristics above 30° angle of attack appeared to be strongly influenced by interaction between the forebody and the canard-wing flow fields.

Lateral-Directional Control Characteristics

The results of tests conducted to determine the effectiveness of the lateral-directional control surfaces are presented in figures 24 to 27. The data are in the form of incremental forces and moments produced by aileron or rudder deflections. Because the lateral-directional control effectiveness was found to be somewhat dependent on canard incidence, data are presented for several canard deflections. Shown in figure 24 are the effects of full and intermediate aileron (differential flaperon) deflections. As expected, the data show that at low angles of attack the full-span flaperons provided large amounts of roll control; however, as wing stall developed at about $\alpha = 10°$, aileron effectiveness was sharply reduced. Nonetheless, for the full deflection a significant and nearly constant level of roll-control effectiveness was maintained at an angle of attack from 25° up to 60°. During tuft-flow studies, regions of attached flow were observed at the wing tips at angles of attack as high as 60°. Thus, it is apparently the nature of the forward-swept-wing stall progression to allow the ailerons to maintain effectiveness up to very high angles of attack. Comparison of the two sets of deflection data indicate that the aileron effectiveness was fairly linear with deflection up to about $\alpha = 30°$. Above 30°, however, the data show that, proportionately, the smaller deflection was much less effective than the larger deflection. The yawing-moment results show that the ailerons produced adverse yaw above 15° angle of attack; however, the level of the adverse yawing moments remained relatively small throughout the high-angle-of-attack range.

As would be expected, the effect of canard deflection on aileron effectiveness was found to result from changes in the wing flow field. Comparison of data for $\delta_c = 0°$ to canard-off data in figure 25 indicates that the canard significantly enhances the aileron effectiveness in the angle-of-attack range from 10° to 60°. This effect was probably due to the canard improving the flow over the inboard portion of the wing. The data for $\delta_c = -25°$ and $-60°$ indicate that the higher canard deflections reduced or eliminated this beneficial effect either by directly blanketing the inboard section of the wing with stalled flow from the canard or by simply promoting wing stall by increasing upwash.

Presented in figure 26 are the incremental forces and moments due to one-half and full rudder deflections. The data show that the rudder effectiveness deteriorated as wing stall developed, and it reached very low values by approximately 40° angle of attack. As discussed previously, this effect was primarily due to the blanketing of the vertical tail in the low-energy stalled wake of the wing. The effect of the canard on rudder power (fig. 27) appears to be very consistent with the canard effects on directional stability discussed earlier. The canard at zero incidence significantly enhanced rudder effectiveness by suppressing wing stall and therefore improving the flow at the vertical tail. Unloading (downloading) the canard reduced this beneficial effect.

Dynamic Stability Derivatives

The effects of the canard on the dynamic longitudinal stability derivatives obtained during pitching-oscillation tests are shown in figure 28. The canard-off configuration exhibited stable pitch-damping characteristics up to $\alpha = 70°$, which suggests that the fuselage strakes provided much of the damping exhibited by the complete configuration. Addition of the canard had the strongest effect at low angles of attack ($\alpha < 15°$) and less significant effects at higher angles of attack.

The dynamic lateral-directional stability derivatives obtained during forced-oscillation tests in roll are presented in figures 29 to 31. The data of figure 29 show that the roll damping decreased above $\alpha = 10°$ with the onset of wing stall such that unstable damping was encountered above 20° angle of attack. With the canard removed, the data show highly unstable values of $C_{l_p} + C_{l_\beta} \sin \alpha$ that were measured in the angle-of-attack range from 30° to 45°, where the slender forebody produced the strong vortex flow field that dominated static stability characteristics as discussed earlier. As expected because of delayed wing-tip stall, the data of figure 30 show stable roll damping for the flat-plate forward-swept wing in the angle-of-attack range from 30° to 40°. The severe loss of roll damping exhibited by the complete configuration above $\alpha = 20°$ is, therefore, not attributable to the wing planform. Comparison of these results with those of past investigations (see, for example, ref. 4) of other configurations having a similar forebody strongly suggests that the forebody aerodynamics dominated the roll damping at high angles of attack and caused the unstable characteristics. The data of figure 29 indicate that addition of the canard at appropriate deflections can reduce the severity of the instability but not eliminate it.

In an attempt to find solutions to this roll-damping problem, a number of forebody strakes were investigated with the idea that they could significantly alter the vortex flow field shed from the forebody and therefore improve roll damping. The design that provided the most improvement was the 40° nose strake discussed earlier. (See fig. 5.) As shown in figure 31, this strake enhanced roll damping in the angle-of-attack range from 20° to 40°; nonetheless, overall damping remained very low in this angle-of-attack range.

The poor roll-damping characteristics coupled with strong static lateral stability and a high inertia ratio of yaw to roll ($I_Z/I_X \approx 10$) would be expected to make the study configuration susceptible to undamped roll oscillations, referred to as wing rock, above 20° angle of attack. To explore this phenomenon further, free-to-roll tests were conducted and a summary of the results obtained is presented in table II. The roll motions of the complete configuration were found to be lightly damped by $\alpha = 20°$. As angle of attack was further increased, limit cycle (undamped) wing rock was observed which began at $\alpha = 25°$ and reached large amplitudes ($\Delta\phi > \pm 25°$) above $\alpha = 35°$. Also, removal of the canard, vertical tail, or wing individually did not fundamentally alter the wing-rock characteristics. These results provide further evidence that the aerodynamics of the fuselage were the source of the unstable roll damping exhibited by the test configuration. Tests with the 40° nose strakes showed that although the strake reduced the amplitude of the wing rock, it did not eliminate it.

The results of the forced-oscillation tests in yaw are presented in figures 32 and 33. Figure 32 shows that with the canard deflected to -25°, the vertical tail provided a stabilizing increment to the yaw-damping derivative $C_{n_r} - C_{n_\beta} \cos \alpha$ throughout the angle-of-attack range tested. The data of figure 33 show that the canard had the greatest effect on yaw damping between angles of attack of about 25° and 50°. In this angle-of-attack range, the best yaw-damping characteristics were obtained at the moderate canard deflections ($\delta_c = -25°$), probably as a result of increased vertical-tail effectiveness.

FREE-FLIGHT-MODEL CONTROL LAWS

Based on the static and dynamic wind-tunnel data discussed earlier, it was obvious that the model would be unflyable without stability augmentation in the pitch axis and that it could benefit greatly from augmentation in roll and yaw. As a result, a three-axis stability augmentation system (SAS) was developed. The SAS gains were defined for the full-scale airplane by using standard linear-analysis techniques, and then they were dynamically scaled for implementation in the model control system. Although the handling-quality specifications of MIL-F-8785B(ASG) (ref. 6) do not apply directly to high-angle-of-attack flight conditions, these specifications were used in the SAS design process as rough guidelines for defining desired frequency and damping characteristics. For example, figure 34 illustrates the procedure used to define the pitch-axis augmentation for 1g flight at 30° angle of attack. Note that the results presented correspond to the full-scale airplane characteristics. Because of the highly unstable static characteristics, the basic airframe short-period mode was aperiodic with a time to double amplitude of 0.85 sec. As shown in the root-locus plot, a SAS using angle of attack and pitch-rate feedbacks can provide the desired short-period frequency and damping characteristics. The feedback gains shown (K_α = -2.0 and K_q = -1.0 sec) were scaled and used in the baseline pitch SAS throughout the free-flight tests. A discussion on the linear-analysis technique and the use of the root-locus plot can be found in reference 7.

A corresponding example for augmentation of the Dutch roll mode is shown in figure 35. At α = 30°, the basic airframe Dutch roll mode was undamped, primarily because of the unstable roll-damping characteristics discussed earlier. The root-locus plot indicates that the desired Dutch roll characteristics could be obtained through roll-damping augmentation by deflecting the ailerons with roll-rate feedback at a fairly high gain.

The three-axis stability augmentation system developed for the free-flight tests is summarized in figure 36 and is given in the following table:

Augmentation system	Feedback	Gain	
		Full scale	Model scale
Pitch SAS	K_α K_q, sec	-2.0 -1.0	-2.0 -.4
Roll SAS	K_p, sec	1.0	0.4
Yaw SAS	K_r, sec K_{pr}, sec	2.0 -.4	0.8 -.16
ARI	K_{ARI}	2.3	2.3

In addition to the pitch and roll channels discussed previously, a yaw SAS comprising yaw and roll-rate feedbacks was also implemented. The yaw-rate feedback (K_r = 2.0 sec) augmented yaw damping, and the roll-rate feedback (K_{pr} = -0.4 sec) enhanced roll coordination. An aileron-to-rudder interconnect (ARI) was also implemented to improve roll coordination at high angles of attack by causing the model to roll more nearly about its velocity vector. The effect of the ARI on

roll response can be appraised by using the lateral control divergence parameter (LCDP) given as follows:

$$LCDP = C_{n_\beta} - C_{l_\beta}\left(\frac{C_{n_{\delta a}} + K_{ARI}C_{n_{\delta r}}}{C_{l_{\delta a}} + K_{ARI}C_{l_{\delta r}}}\right)$$

Positive values of this parameter indicate a normal roll response, and negative values indicate a reversed response. The data of figure 37 indicate that without the ARI, the model would exhibit a reversed response to a lateral-control input above about 30° angle of attack because of aileron adverse yaw. With the addition of the ARI ($K_{ARI} = 2.3$), however, the data indicate that normal response could be achieved up to 40° angle of attack. The reduction in the ARI-on LCDP values above $\alpha = 30°$ was due to the combination of aileron adverse yaw and loss in rudder effectiveness. Based on these results, it would be expected that the lateral-directional control of the model in yaw and roll in free flight would degrade rapidly above 30° angle of attack and be marginal by $\alpha = 40°$.

It should be noted that the aforementioned control laws were developed to meet only the requirements dictated by the restricted test conditions of the free-flight test technique - that is, relatively small motion perturbations about a 1g wings-level flight condition. As a result, the control laws derived are fairly simple. The design of control laws for the full high-angle-of-attack envelope of a highly maneuverable airplane such as the X-29A requires that many other factors be addressed which will inherently complicate the final design. A detailed discussion of some of the factors involved in the design of high-angle-of-attack control laws is presented in reference 8.

RESULTS AND DISCUSSION OF FREE-FLIGHT TESTS

Baseline Configuration

The primary configuration investigated in the free-flight tests will be referred to as the baseline configuration and is defined as follows:

c.g. = $-0.12\bar{c}$

$\delta_f = 17.5°$

$\delta_s = 30°$

SAS on; ARI on

Longitudinal characteristics.- The longitudinal stability and control characteristics of the baseline configuration were found to be good at angles of attack from 20° up to the maximum attained in the tests (40°). The model was easy to fly and appeared to the pilot to have good static stability and damping characteristics. These results verified that the pitch SAS was effective in masking the high level of inherent instability of the basic airframe. The only indications to the pilot that he was flying a highly unstable configuration were the variation of trimmed-canard deflection with angle of attack and the unusual level of canard activity apparent at all flight conditions. It was observed that during flight, the canards were

constantly undergoing relatively small deflections about the trim setting, even during periods without pilot pitch inputs. This characteristic resulted from the fact that the high-gain pitch SAS was totally responsible for the airplane pitch stability and therefore had to respond to all disturbances, such as those caused by turbulence or coupling from the roll/yaw axes.

Despite the constant motion, however, the canard-deflection (slew) rates observed in the free-flight tests were not high. Maximum slew rates did not exceed 100°/sec (40°/sec full scale). It should be noted, however, that the 1g flight condition of the tests did not provide the most severe test of canard slew-rate requirements. It would be expected that much higher rates would be needed during rapid, large-amplitude maneuvers such as those encountered during close-in air-to-air combat.

An undesirable characteristic noted in the flight tests was a lack of adequate nose-up pitch control at angles of attack below 20°. The trimmed-canard setting for these conditions was approximately zero and, as shown in figure 10, very little nose-up pitching moment could be generated by trying to increase lift on the canard (load the canard further) since that would only promote canard stall. A possible solution to this problem would be to obtain additional nose-up control moment by making the strake flap an active pitch-control device. As discussed earlier, the strake flaps provide a nearly constant level of control effectiveness throughout the angle-of-attack range. Further improvements could also be obtained by modifying the strake-flap deflection schedule so that full nose-down deflection is not reached until α is approximately 30°.

In closing the discussion of longitudinal characteristics, it is appropriate to note that the accomplishment of the free-flight tests of the X-29A model represents several firsts for the stall/spin research program at Langley. This work is the first time that a dynamically scaled, remotely piloted free-flight model has been successfully flown up through the stall with such a high level of airframe pitch instability (in excess of -32 percent). It is also the first time that such a high level of dependence has been placed on the automatic stability augmentation system for satisfactory flight characteristics. The results of the tests indicate that airplane design is feasible for very high levels of airframe pitch instability as long as there is adequate pitch-control power and sensor information to provide the necessary levels of stability augmentation.

Lateral-directional characteristics.- The possibility of directional divergence during flight at high angles of attack is normally examined by means of the dynamic directional stability parameter $C_{n_{\beta,dyn}}$. (See ref. 9.) Negative values of this parameter indicate the existence of a directional divergence. Values of $C_{n_{\beta,dyn}}$ calculated from the static wind-tunnel data discussed earlier are presented in figure 38. Because canard setting had a significant effect on C_{n_β}, the $C_{n_{\beta,dyn}}$ values were computed based on the canard deflection required for trim at each angle of attack. It is seen that $C_{n_{\beta,dyn}}$ remained positive throughout the test angle-of-attack range, thus indicating that a directional divergence would not be encountered during the free-flight tests.

The lateral-directional stability and control characteristics observed for the baseline configuration are summarized in figure 39. Below about 25° angle of attack,

the model was easy to fly, thus exhibiting good stability characteristics and high control effectiveness. It was noted, however, that the yaw motions were somewhat unsteady, as if the model was always being excited by small disturbances in yaw. These disturbances could have resulted from several factors such as tunnel turbulence; however, it is felt that the constant canard motion discussed earlier may also have contributed because of the strong influence of the canard on the vertical-tail flow field. In the angle-of-attack range from 25° to 35°, mild nose wandering was encountered, probably as a result of loss of static directional stability. (See fig. 16.) The nose wandering, coupled with degrading rudder effectiveness (see fig. 27), increased the pilot work load required to fly the model. Nonetheless, the flight motions remained well-damped and there was still sufficient lateral-directional control effectiveness. Above 35° angle of attack, however, the rudder effectiveness had degraded to a point where control of the model became marginal and pilot work load was very high. Generally, near 40° angle of attack, control of the model was lost in a slow lateral translation out of the jet against full corrective control. To eliminate the possibility that the aileron adverse yaw was causing the departure, flights were made with the aileron deactivated so that the rudder was the only lateral-directional control. Loss of control was also experienced near 40° angle of attack, thus further confirming that loss of rudder effectiveness was the primary cause of the divergence.

Effect of Stability Augmentation Systems

Pitch axis.- The effect of the pitch stability augmentation system (SAS) on the longitudinal flying characteristics of the model was evaluated by successively reducing the angle-of-attack and pitch-rate feedback gains. Presented in figure 40 are time histories of flights made with the baseline SAS and with the SAS gains reduced by 50 percent. With the baseline SAS, it is seen that the longitudinal motions of the model were well-behaved. Small perturbations in angle of attack and pitch rate were experienced, and the pitch pilot was required to make only very small inputs to maintain the model in the desired area of the test section. With the SAS gains reduced by 50 percent, however, the time histories show significantly degraded characteristics. Despite numerous rapid pilot inputs, pitch control of the model was very poor as indicated by the large excursions in angle of attack. It was found that the model could be flown with pitch SAS gains less than 50 percent of the baseline values; however, the pilot work load was extremely high and the model pitch excursions were too large to allow effective evaluation of its lateral-directional characteristics.

Roll axis.- The effect of the roll SAS was studied by making flights with reduced roll SAS gains and with the roll SAS deactivated. Figure 41 presents a summary of the model lateral-directional characteristics when flown without the roll SAS. Below 20° angle of attack, the model exhibited good flying characteristics, although damping in roll was noticeably lower than that of the baseline configuration. Above 20° angle of attack, small-amplitude, undamped roll oscillations were encountered which increased pilot work load. Control of the model became marginal above about 25° angle of attack, and loss of control usually occurred by 30° angle of attack because of large-amplitude wing rock.

The rapid buildup of the wing rock was studied by making flights in which the roll SAS was deactivated for short periods of time. During these periods, roll pilot inputs were also kept to a minimum to avoid affecting the damping characteristics of the model. Presented in figure 42 are time histories measured during one of these flights at a trim angle of attack of about 25°. Shortly after deactivation of the

roll SAS ($t \approx 7$ sec), wing rock was encountered with the motions rapidly increasing in amplitude. Comparison of the p and r traces show that the oscillations were primarily about the roll axis and therefore were very similar to those observed in the free-to-roll tests. At $t \approx 18$ sec, reactivation of the roll SAS was necessary to prevent loss of control of the model. It is seen that the roll SAS very quickly suppressed the wing-rock motion. Flights conducted with reduced roll SAS gains showed that satisfactory flying characteristics could not be achieved with more than a 50-percent reduction of the baseline roll SAS gain.

The aforementioned results confirmed the predictions of the forced-oscillation and free-to-roll tests and verified that a high-gain roll SAS could suppress the wing rock inherent in the airframe.

Yaw axis.- As expected, deactivating the yaw SAS significantly reduced the yaw damping of the model which made it more difficult to fly. The unsteadiness of the yaw motions were magnified and pilot work load increased accordingly. However, eliminating the yaw SAS did not significantly alter the wing-rock characteristics or the ability to fly the model up to the maximum lift region before control was lost because of lack of rudder effectiveness.

Configuration Effects

In addition to the baseline configuration, flights were also made to determine the effects of the spin-chute canister (at three locations), the 40° nose strakes, the center-of-gravity location, and the strake-flap deflection.

The flight characteristics of the model with the addition of the spin-chute canister in any of the three locations were found to be very similar to the characteristics of the baseline configuration. This result agrees very well with the small effects seen in the static wind-tunnel tests discussed earlier.

The flight characteristics observed when the 40° nose strakes were added also correlated well with the static wind-tunnel data, which showed that the strakes produced a large degradation in directional stability above 10° angle of attack. (See fig. 21.) In the free-flight tests, this effect was manifested in the form of "nose wandering" in yaw which became quite severe above about 20° angle of attack. The model could not be flown above 25° angle of attack because of this problem. Thus, the 40° nose strakes do not appear to be an acceptable solution to the wing-rock problem.

The free-flight results for the effects of c.g. location and strake-flap setting can best be analyzed by examining the static trimmed-canard variations for these cases. Presented in figure 43 are static trimmed-canard variations with angle of attack for the baseline configuration ($\delta_s = 30°$ and c.g. $= -0.12\bar{c}$) and for two other combinations of strake-flap setting and c.g. location. The data show significant changes in static trimmed-canard settings because of a 5-percent aft c.g. shift or a 30° change in strake-flap setting. As discussed earlier, canard setting had a substantial effect on static directional stability and rudder effectiveness. Unloading the canard had the following effects: (1) It degraded C_{n_β} below $\alpha = 30°$ and enhanced C_{n_β} above 30°; and (2) it degraded $C_{n_{\delta r}}$ throughout the

test angle-of-attack range. The net effect on directional stability is shown in figure 44, which compares trim C_{n_β} for the three configurations discussed previously.

These same effects were observed in the free-flight tests of the aft c.g. location ($-0.07\bar{c}$) and/or of zero strake-flap deflection. For example, for the worst-case configuration combining aft c.g. and $\delta_s = 0°$ (configuration 3), nose wandering in yaw (degradation of C_{n_β}) was observed to begin at a lower angle of attack and to be more severe below $\alpha = 30°$ than that for the baseline configuration. However, above $\alpha = 30°$ a reduction in nose wandering was observed, which reflected the higher levels of C_{n_β} as compared with those of the baseline configuration. (See fig. 44.) Nonetheless, the degraded rudder effectiveness of configuration 3 generally led to loss of control at angles of attack somewhat lower than 40°.

SUMMARY OF RESULTS

The results of a wind-tunnel free-flight investigation of the high-angle-of-attack characteristics of a forward-swept-wing fighter-airplane configuration may be summarized as follows:

1. The model exhibited good dynamic stability characteristics up to 40° angle of attack with stability augmentation in pitch, roll, and yaw. Flight at higher angles of attack was not possible because of lack of yaw-control effectiveness.

2. Because of the very high level of static pitch instability of the airframe, controlled flight was not possible without the pitch stability augmentation system (SAS). With the SAS activated, the model exhibited excellent longitudinal flying characteritics where adequate pitch control was available. These results indicate that it is feasible to design for very high levels of airframe pitch instability as long as there is adequate control power and sensor information to provide the necessary level of stability augmentation.

3. Nose-up pitch control below about 20° angle of attack was found to be marginal because of canard stall. Making the strake flap an active pitch-control device should alleviate this condition.

4. With the roll stability augmentation system deactivated, the model exhibited large-amplitude undamped roll oscillations (wing rock) above 25° angle of attack which made control marginal. The roll SAS acting through the powerful flaperons effectively suppressed the wing rock up to the highest angle of attack achieved (40°).

5. The static lateral-directional stability characteristics of the configuration were not dominated by any one configuration feature throughout the angle-of-attack range. Above about 30° angle of attack, the fuselage forebody produced beneficial contributions to static directional stability, but it also produced unstable values of damping in roll. The forward-swept wing was primarily responsible for the lateral stability characteristics up to about 30° angle of attack; however, the characteristics above 30° angle of attack appeared to be strongly influenced by an interaction between the forebody and the canard-wing flow fields.

6. Canard setting was found to influence significantly the high-angle-of-attack, vertical-tail flow characteristics and hence static directional stability, yaw damping, and rudder effectiveness.

Langley Research Center
National Aeronautics and Space Administration
Hampton, VA 23665
December 2, 1983

REFERENCES

1. Krone, Norris J., Jr.: Divergence Elimination With Advanced Composites. AIAA Paper No. 75-1009, Aug. 1975.

2. Nguyen, Luat T.; Yip, Long P.; and Chambers, Joseph R.: Self-Induced Wing Rock of Slender Delta Wings. AIAA-81-1883, Aug. 1981.

3. Chambers, Joseph R.; Bowman, James S., Jr.; and Malcolm, Gerald N.: Stall/Spin Test Techniques Used by NASA. Stall/Spin Problems of Military Aircraft, AGARD-CP-199, June 1976, pp. 13-1 - 13-12.

4. Grafton, Sue B.; Chambers, Joseph R.; and Coe, Paul L., Jr.: Wind-Tunnel Free-Flight Investigation of a Model of a Spin-Resistant Fighter Configuration. NASA TN D-7716, 1974.

5. Bates, William R.: Static Stability of Fuselages Having a Relatively Flat Cross Section. NACA TN 3429, 1955. (Supersedes NACA RM L9I06a.)

6. Chalk, C. R.; Neal, T. P.; Harris, T. M.; Pritchard F. E.; and Woodcock, R. J.: Background Information and User Guide for MIL-F-8785B(ASG), "Military Specification - Flying Qualities of Piloted Airplanes." AFFDL-TR-69-72, U.S. Air Force, Aug. 1969. (Available from DTIC as AD 860 856.)

7. Etkin, Bernard: Dynamics of Atmospheric Flight. John Wiley & Sons, Inc., c.1972.

8. Nguyen, Luat T.; Gilbert, William P.; and Ogburn, Marilyn E.: Control-System Techniques for Improved Departure/Spin Resistance for Fighter Aircraft. NASA TP-1689, 1980.

9. Moul, Martin T.; and Paulson, John W.: Dynamic Lateral Behavior of High-Performance Aircraft. NACA RM L58E16, 1958.

TABLE I.- MODEL MASS AND GEOMETRIC CHARACTERISTICS

Weight, lb	61.75
Moments of inertia:	
I_X, slug-ft^2	0.484
I_Y, slug-ft^2	4.49
I_Z, slug-ft^2	4.61
Wing:	
Span, ft	4.35
Mean aerodynamic chord, ft	1.15
Area, ft^2	4.74
Aspect ratio	4.0
Sweep (leading edge), deg	-29.27
Sweep (0.25c chord), deg	-33.73
Taper ratio	0.404
Dihedral angle, deg	0
Flaperon area (total), ft^2	0.734
Flaperon deflection, deg	17.5 (T.E.D.) to -27.7 (T.E.U.)
Canard:	
Span, ft	2.18
Area (total), ft^2	0.947
Aspect ratio	1.47
Taper ratio	0.318
Deflection, deg	30 (T.E.D.) to -60 (T.E.U.)
Vertical tail:	
Height, ft	1.07
Area, ft^2	0.864
Aspect ratio	1.32
Taper ratio	0.306
Rudder area, ft^2	0.177
Rudder deflection, deg	±30
Strake flap:	
Area (total), ft^2	0.267
Deflection, deg	±30

TABLE II.- SUMMARY OF FREE-TO-ROLL RESULTS

Configuration	Angle of attack, deg	Results
Complete configuration, $\delta_c = -25°$	20	Lightly damped[a]
	25	Mild wing rock[b]
	30	Moderate wing rock[c]
	35	Large-amplitude wing rock[d]
	40	Large-amplitude wing rock[d]
	45	Large-amplitude wing rock[d]
Body, wing, and tail (canard off)	40	Large-amplitude wing rock[d]
Body and wing (canard and tail off)	40	Large-amplitude wing rock[d]
Body and tail (canard and wing off)	40	Large-amplitude wing rock[d]
Complete configuration, plus 40° nose strakes; $\delta_c = -25°$	40	Mild wing rock[b]

[a]Lightly damped: Roll motions eventually die out.
[b]Mild wing rock: $\Delta\phi < \pm 15°$.
[c]Moderate wing rock: $\pm 15° < \Delta\phi < \pm 15°$.
[d]Large-amplitude wing rock: $\Delta\phi > \pm 25°$.

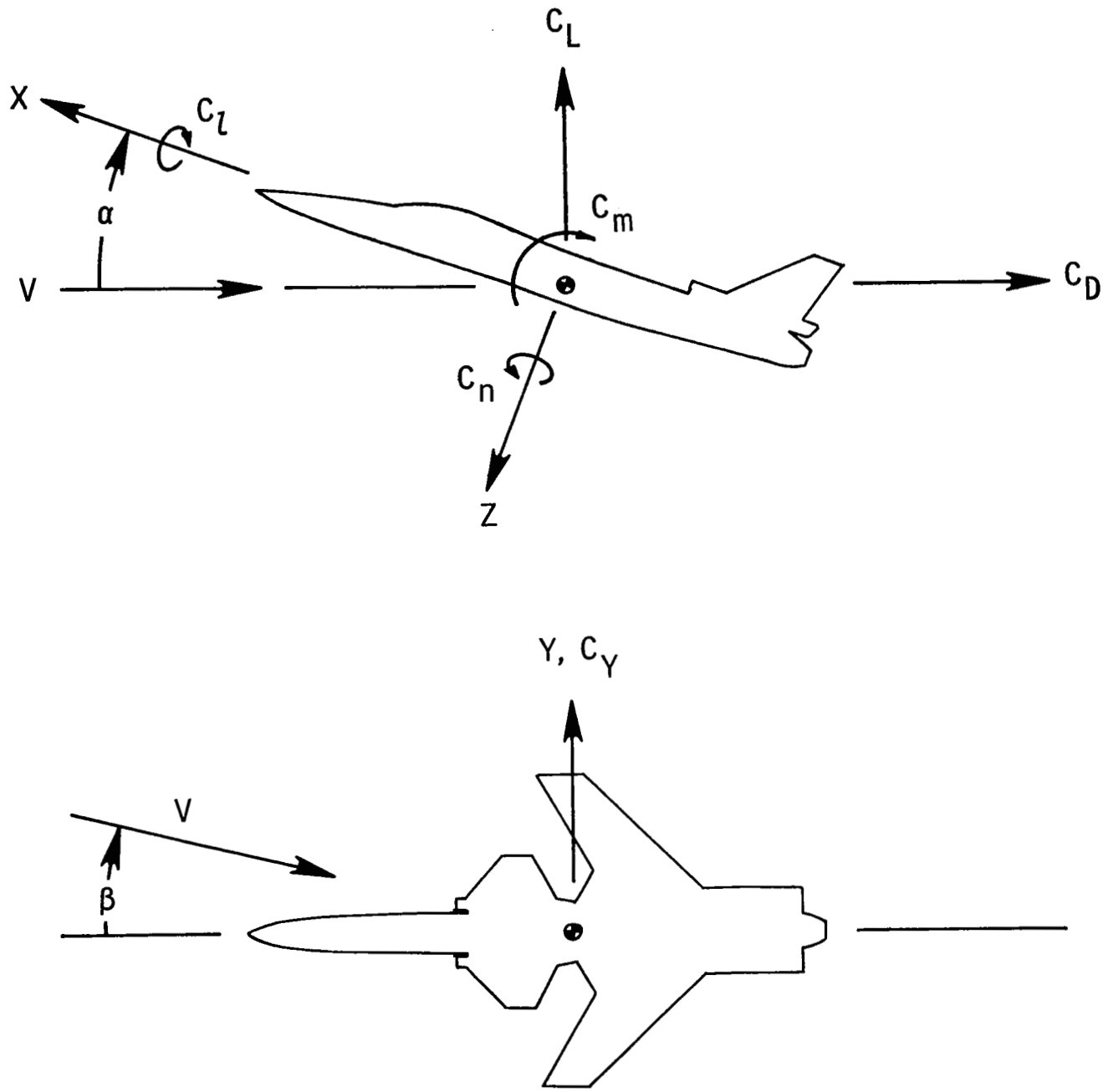

Figure 1.- System of axes.

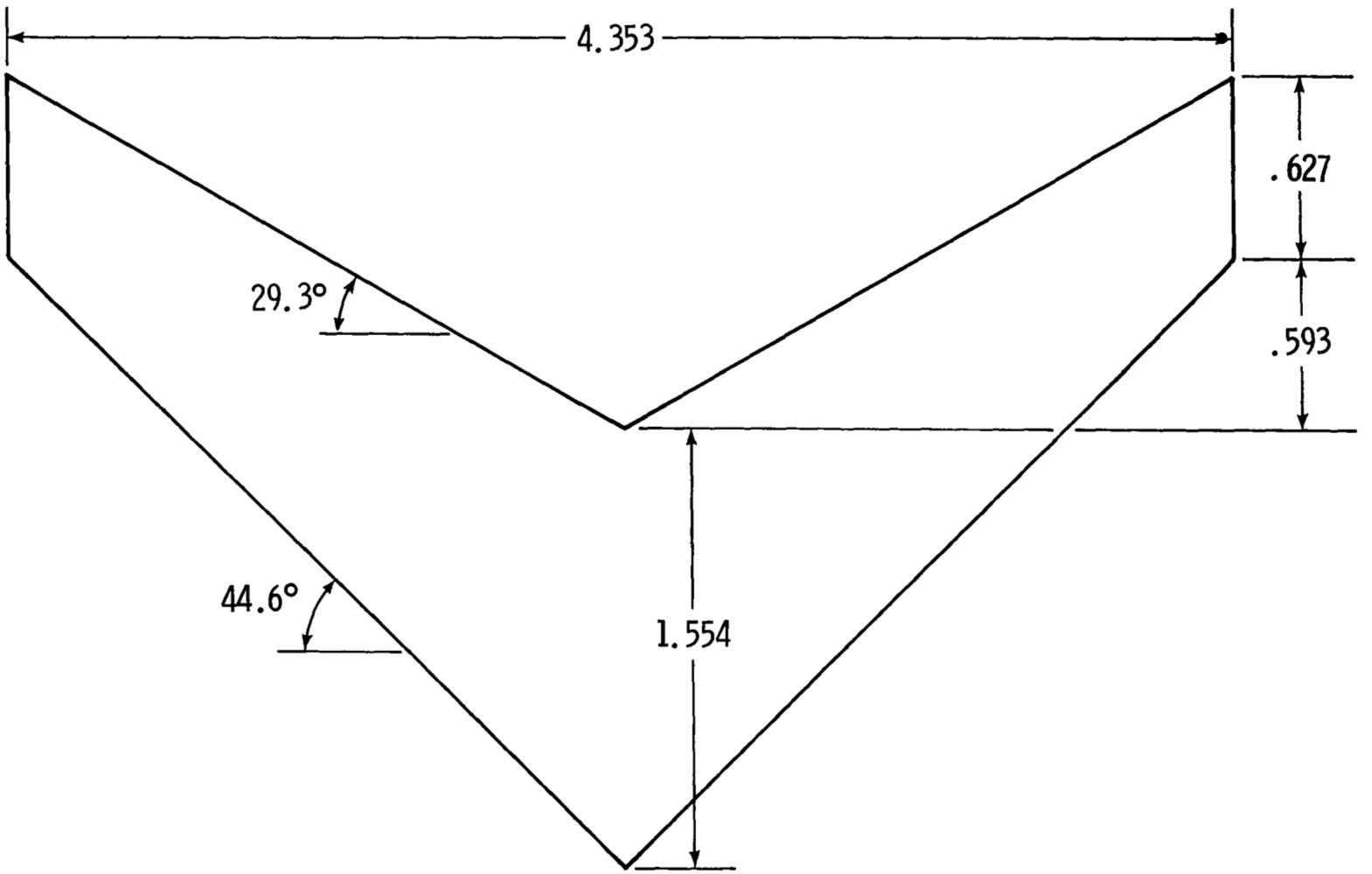

(a) Plan-view sketch of flat-plate wing model.

Figure 2.- Drawings of models. Dimensions are given in feet unless otherwise specified.

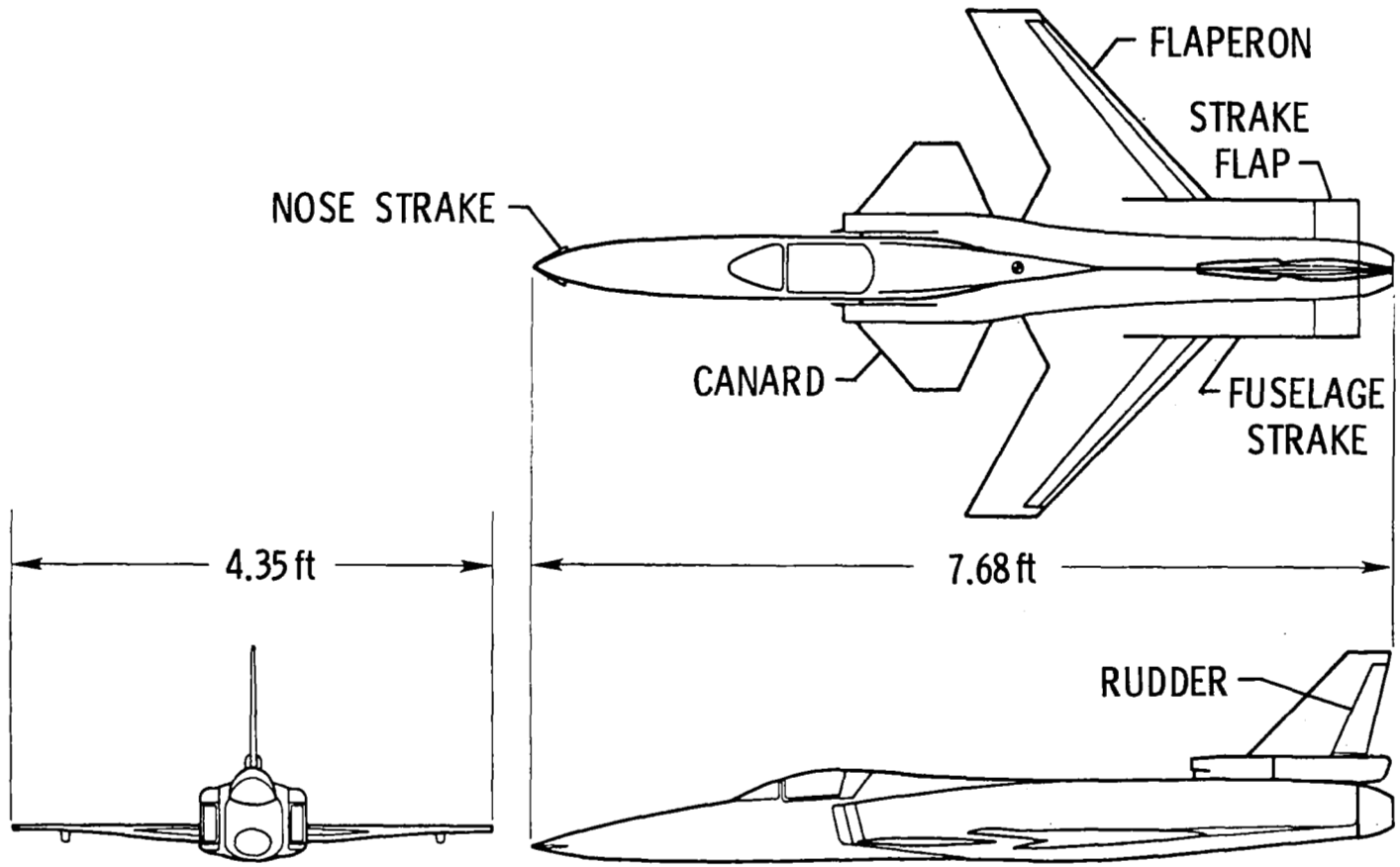

(b) Three-view sketch of basic model.

Figure 2.- Concluded.

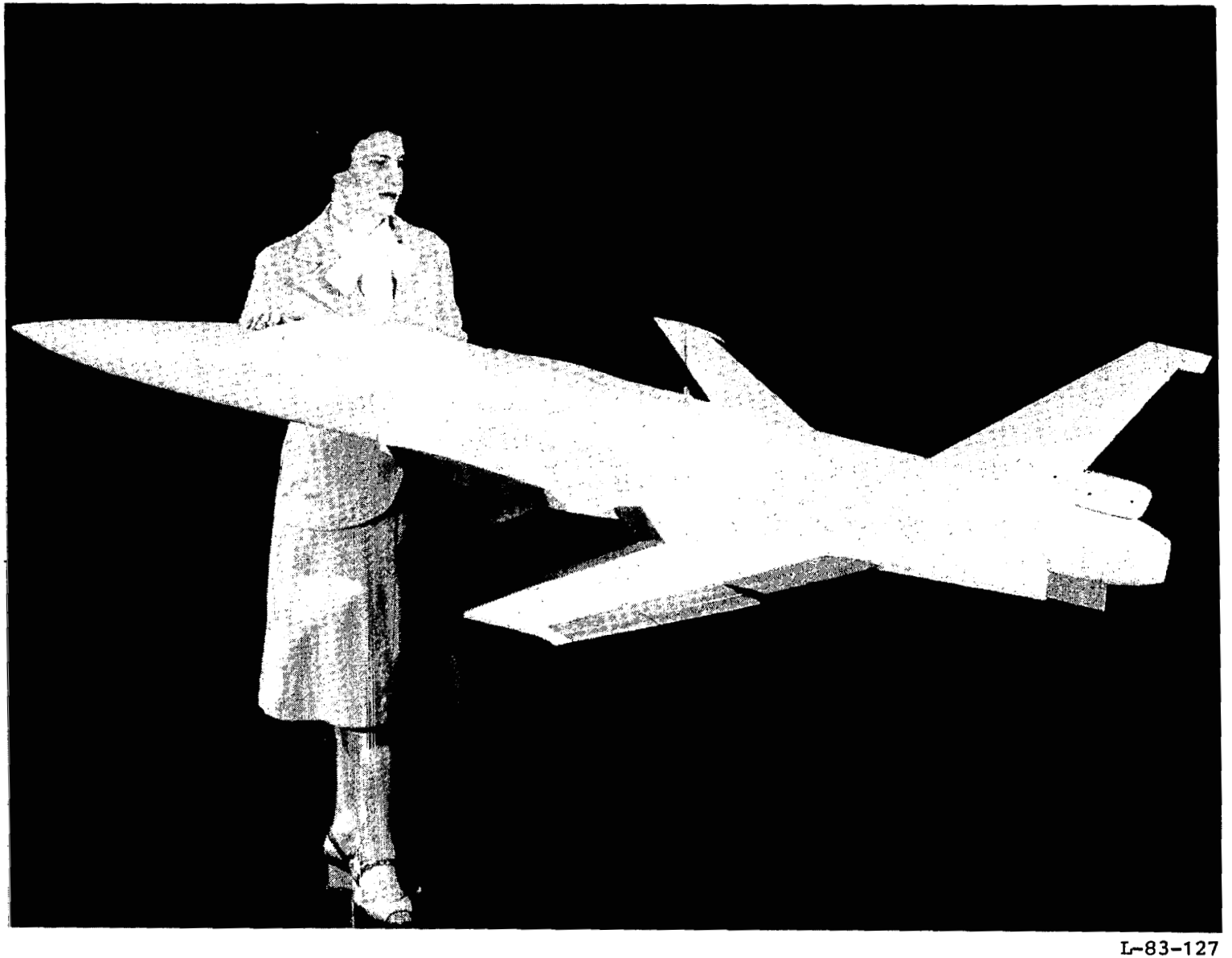

L-83-127

(a) Side view.

Figure 3.- Photographs of basic model.

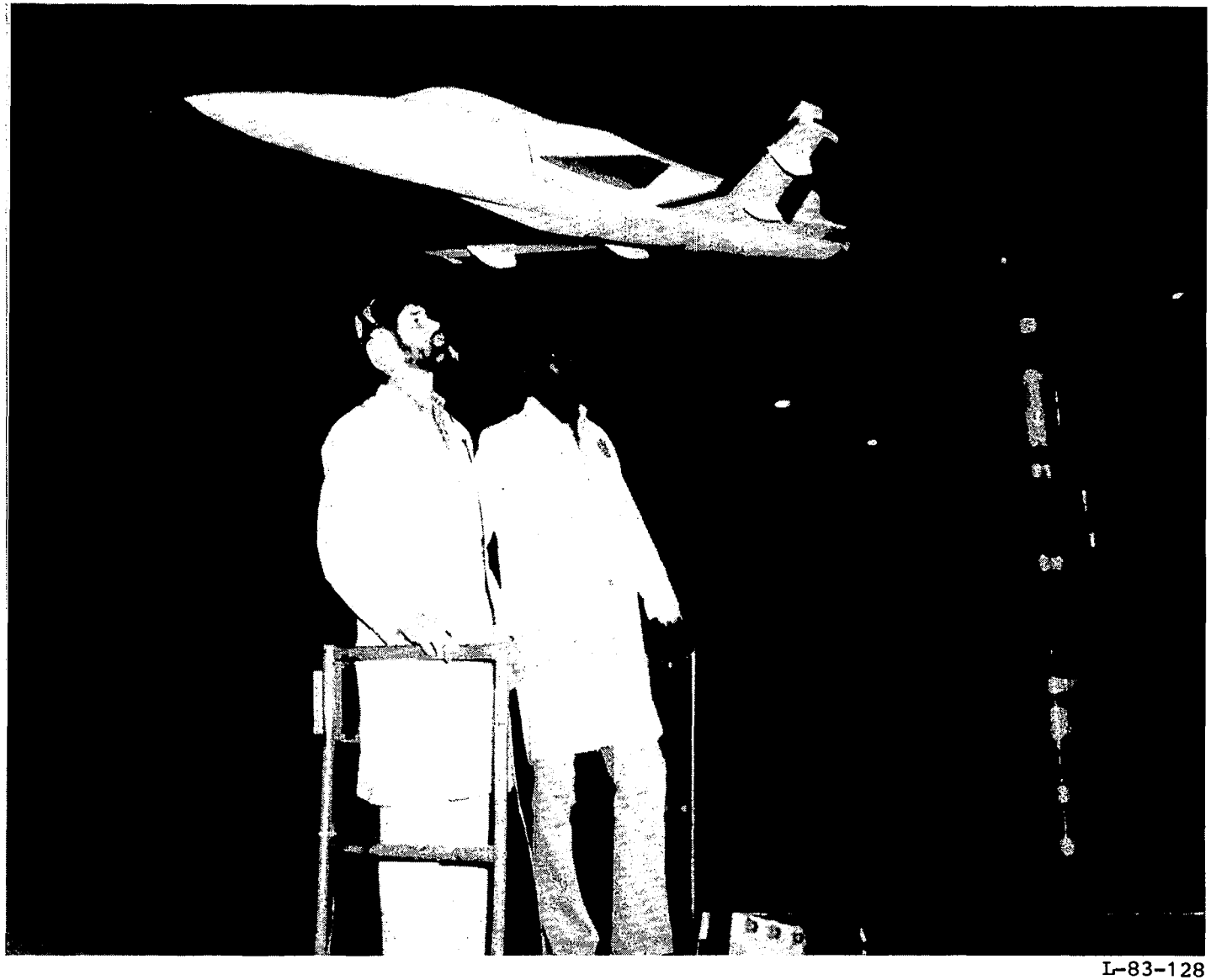

L-83-128

(b) Mounted in the Langley 30- by 60-Foot Tunnel during static-force testing.

Figure 3.- Concluded.

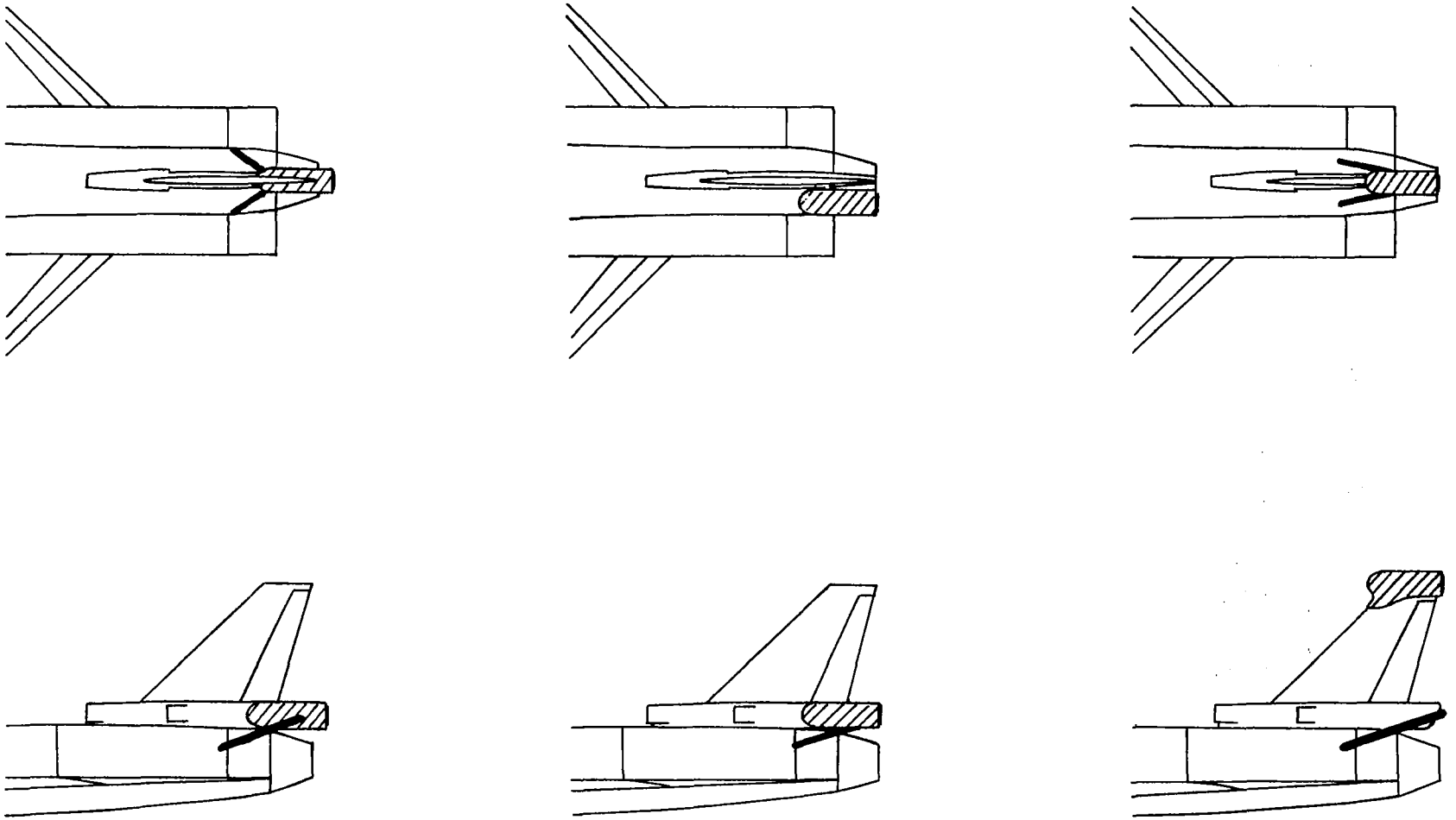

(a) Rear location.

(b) Side location.

(c) Top location.

Figure 4.- Locations of spin-chute canister.

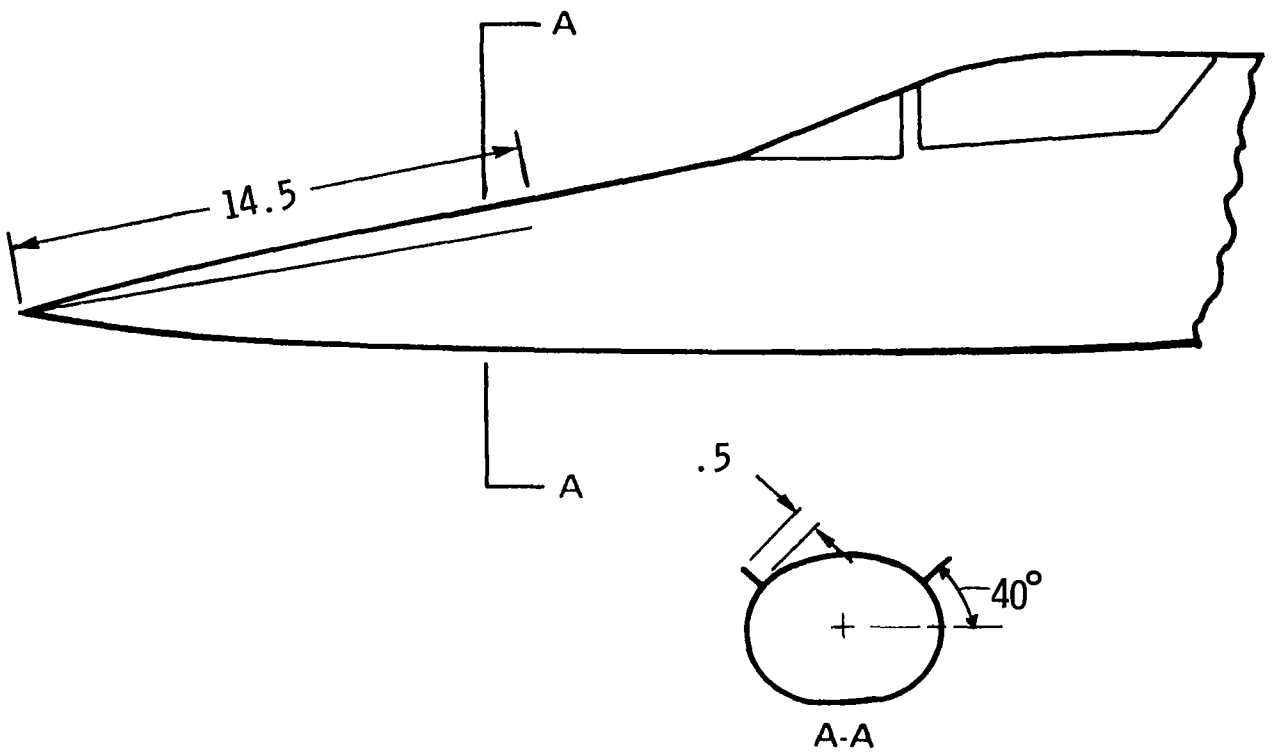

Figure 5.- Geometry of 40° nose strakes. Dimensions are given in inches unless otherwise specified.

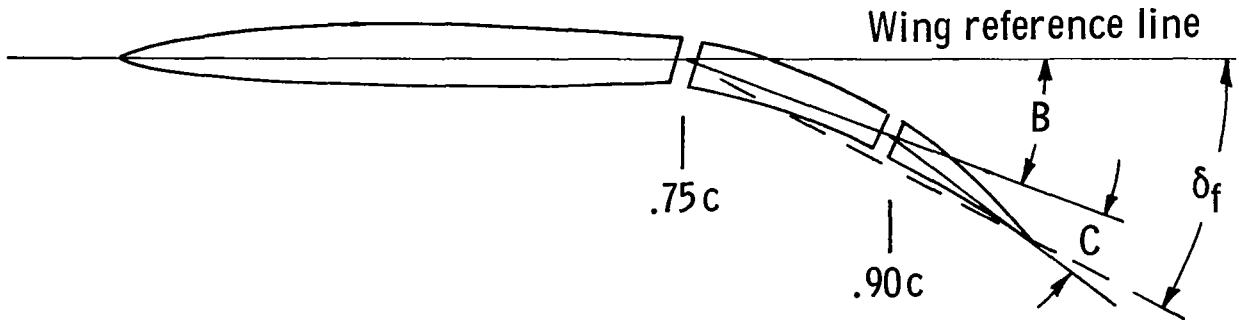

Position	δ_f, deg	B, deg	C, deg
Maximum T.E. D.	17.5	12.3	13.6
Undeflected	0	0	0
Maximum T.E. U.	-27.7	-19.3	-19.9

Figure 6.- Flaperon-deflection definition. All angles are measured perpendicular to 0.75c.

L-83-129

Figure 7.- Photograph of basic model in free flight.

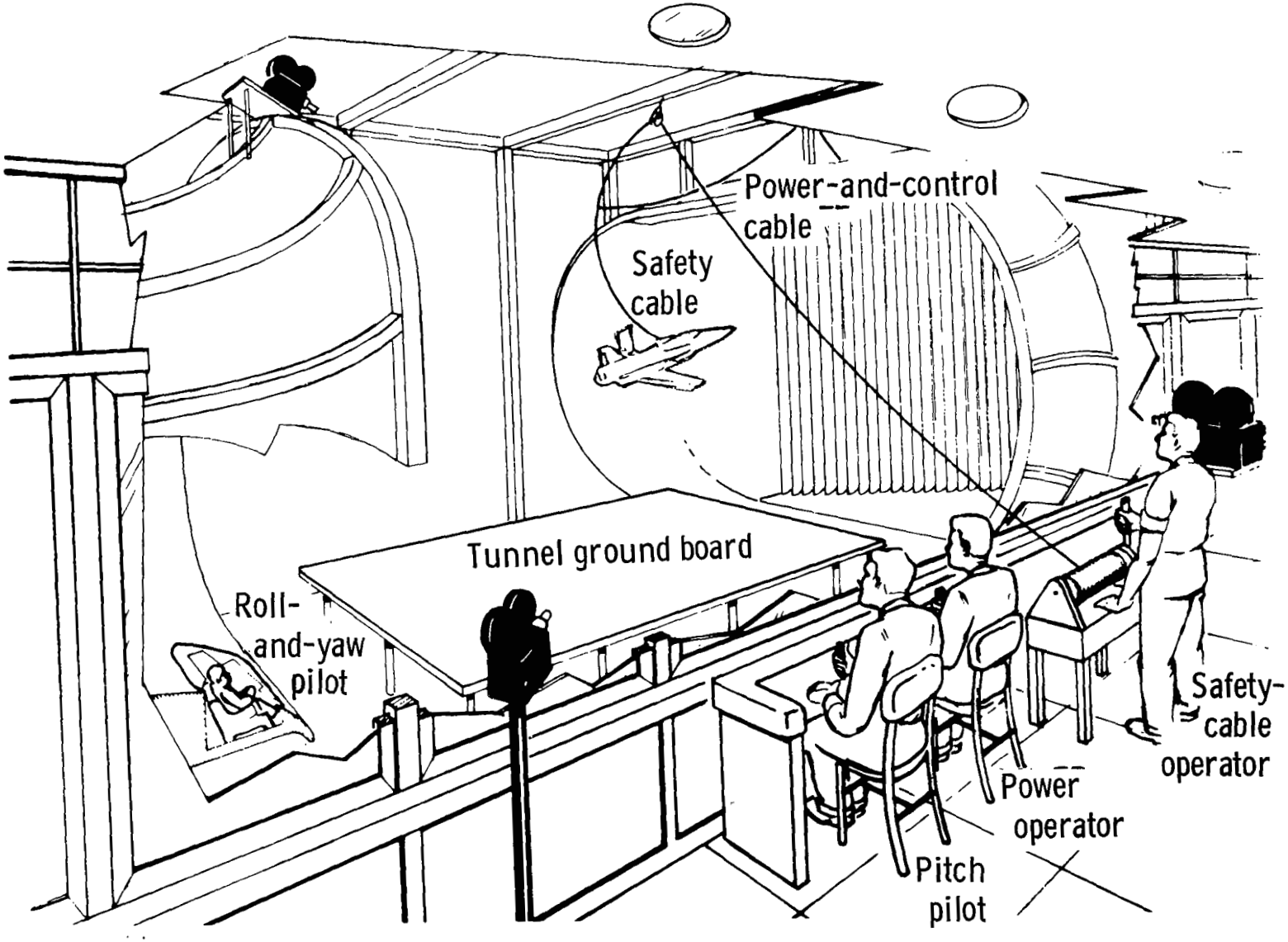

Figure 8.- Test setup for wind-tunnel free-flight tests.

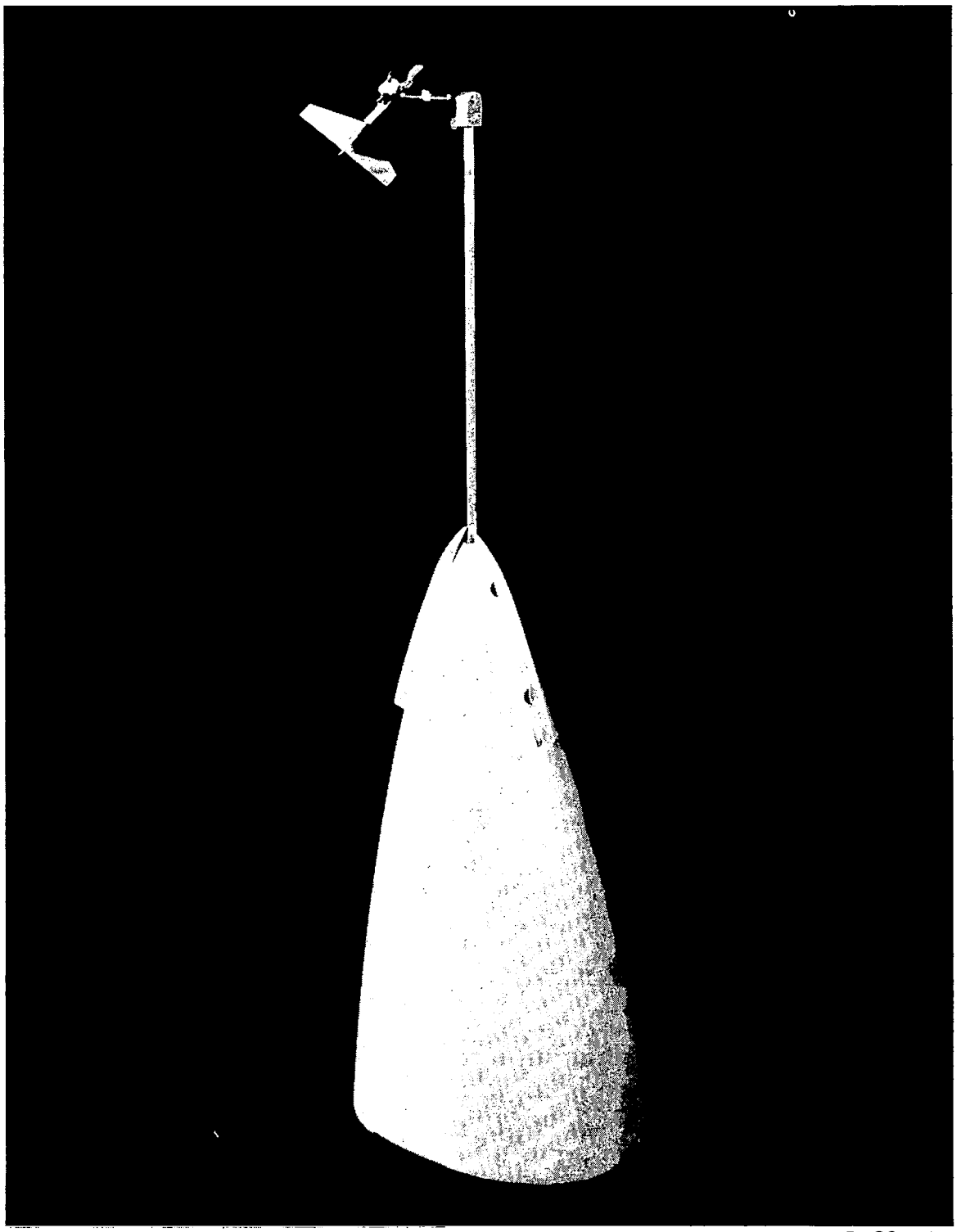

L-83-130

Figure 9.- Boom-mounted α/β vane sensor on model forebody.

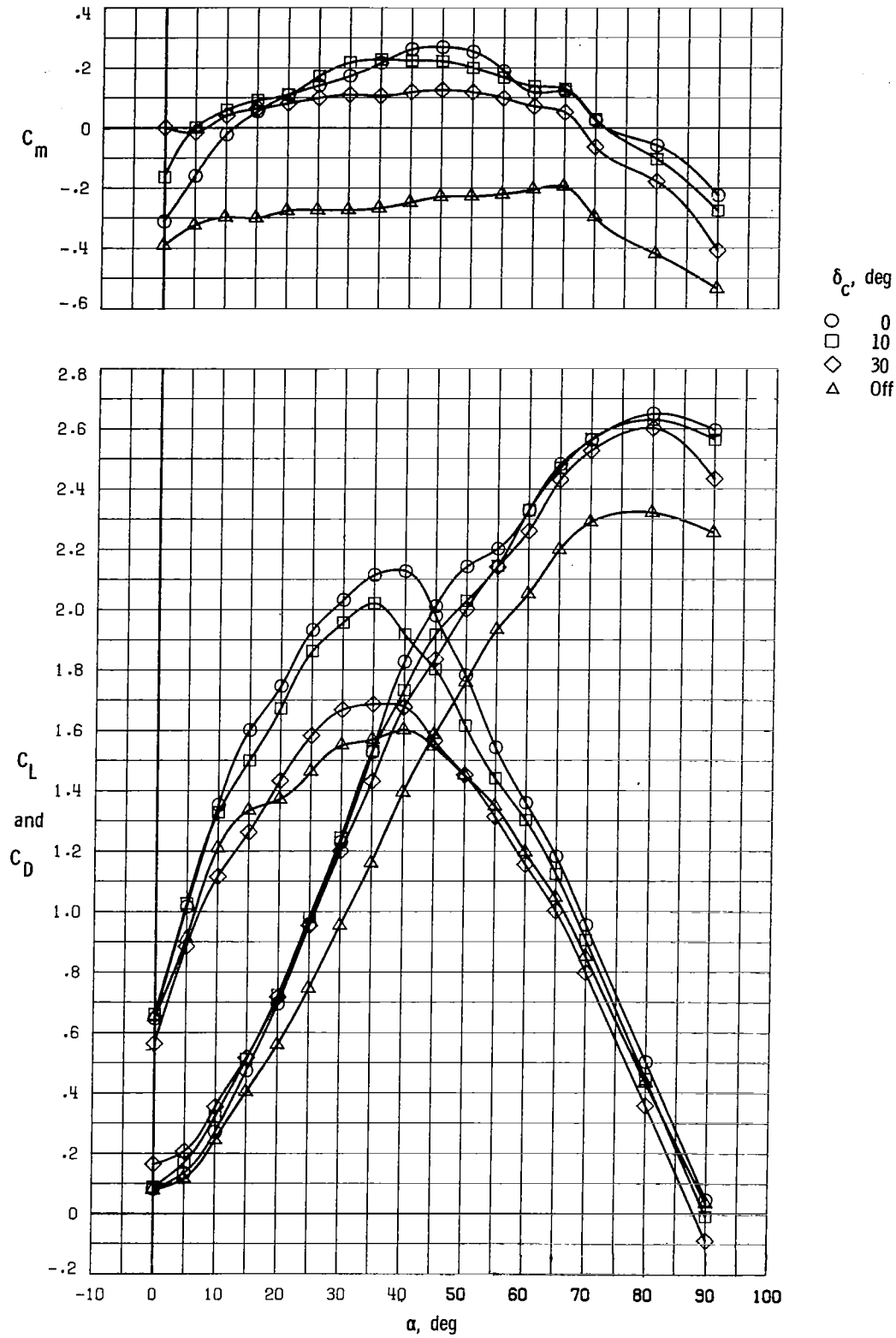

(a) Positive canard deflections.

Figure 10.- Effect of canard deflection on static longitudinal characteristics. $\delta_f = 17.5°$; $\delta_s = 30°$.

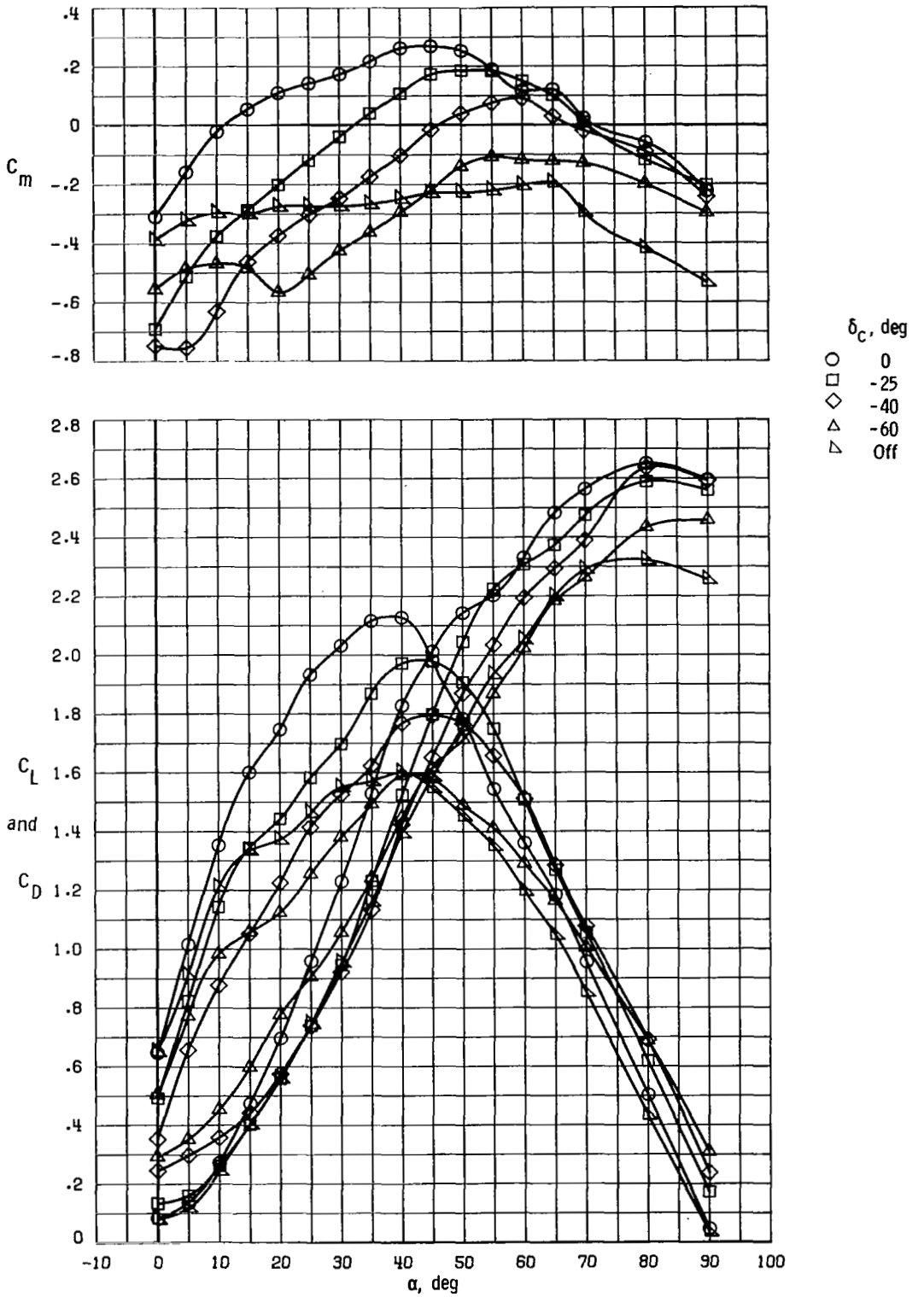

(b) Negative canard deflections.

Figure 10.- Concluded.

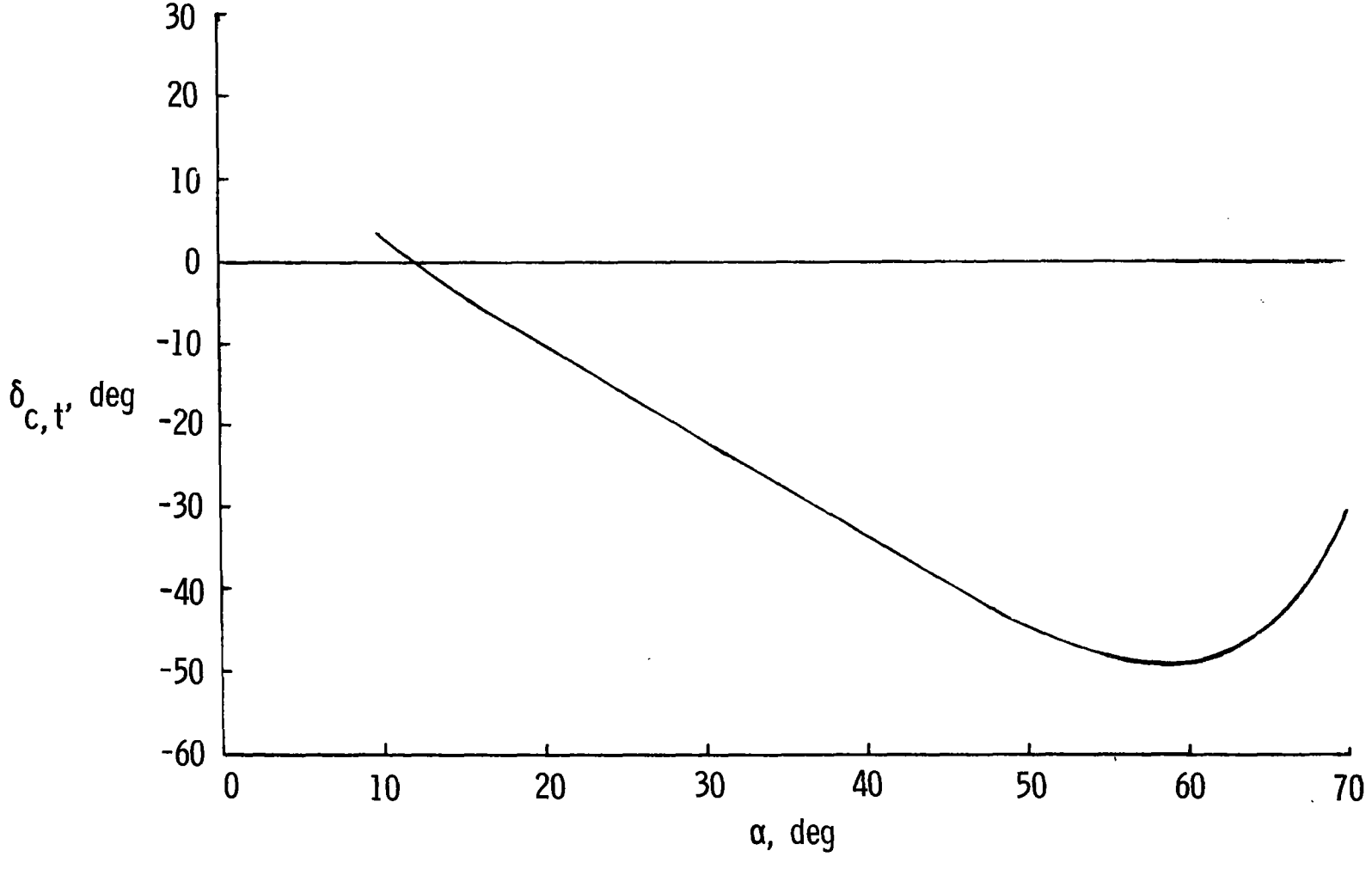

Figure 11.- Canard deflection required for trim. c.g. at $-0.07\bar{c}$; $\delta_f = 17.5°$; $\delta_s = 30°$.

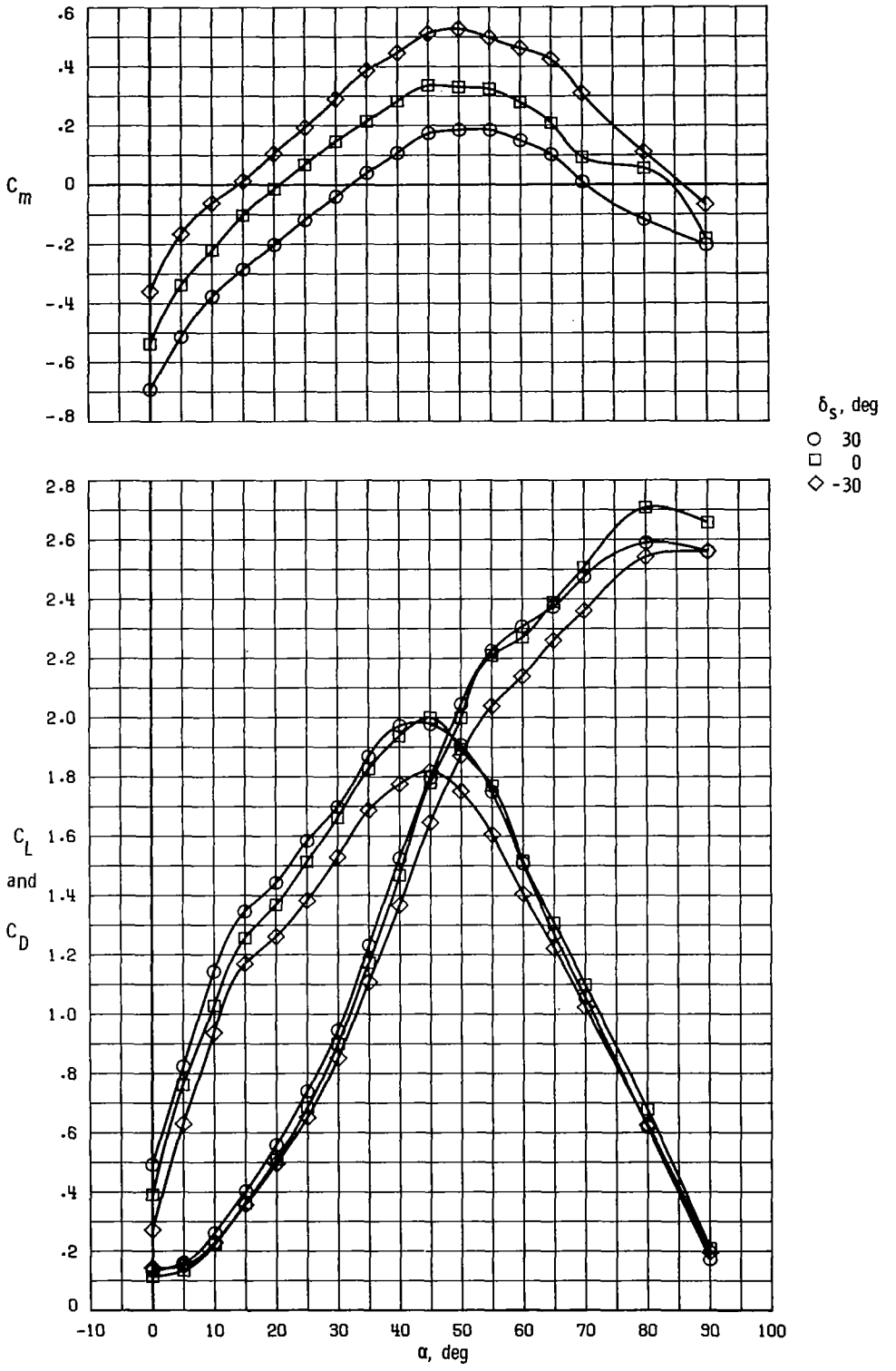

Figure 12.- Effect of strake-flap deflection on static longitudinal characteristics. $\delta_c = -25°$; $\delta_f = 17.5°$.

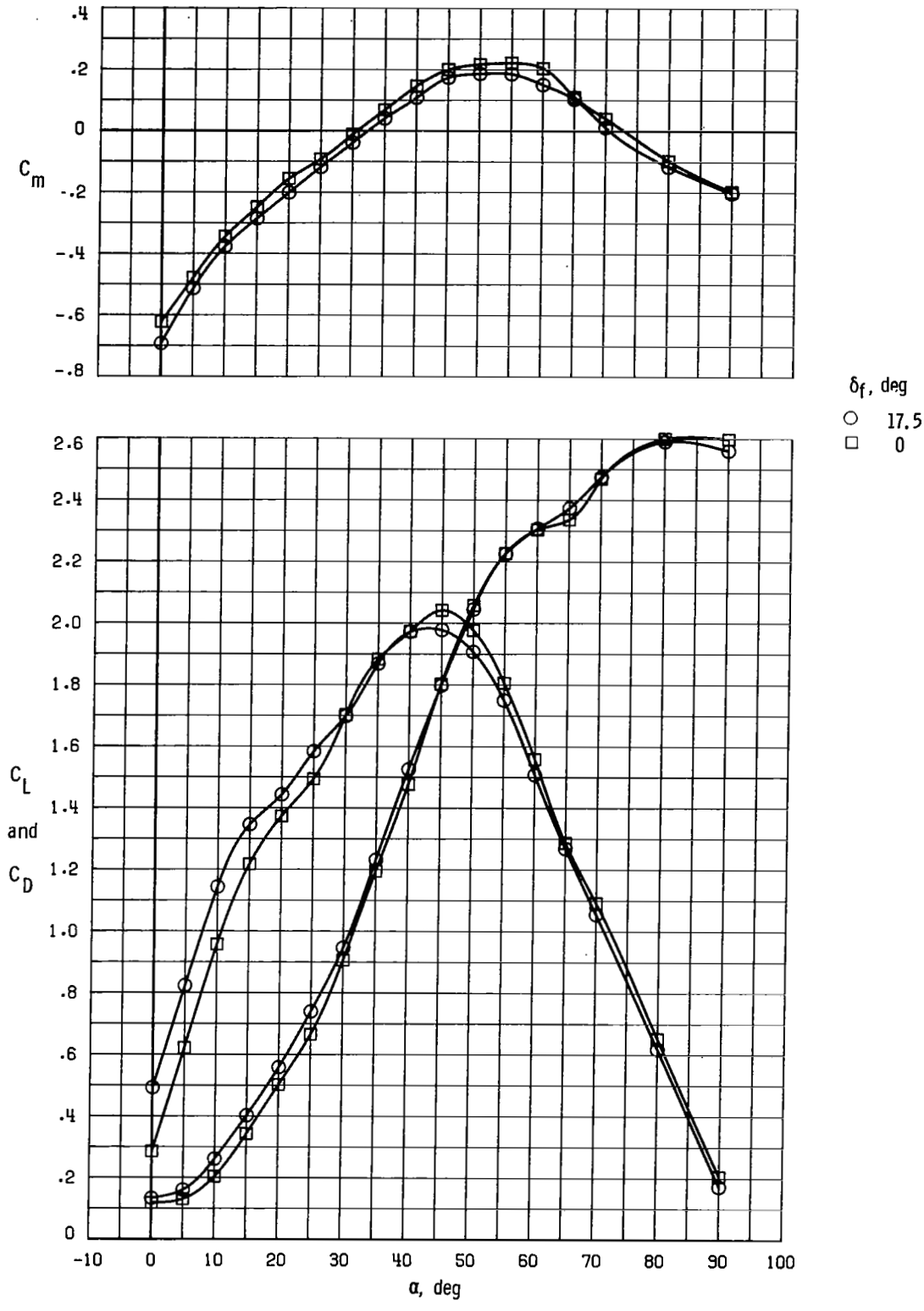

Figure 13.- Effect of flaperon deflection on static longitudinal characteristics. $\delta_c = -25°$; $\delta_s = 30°$.

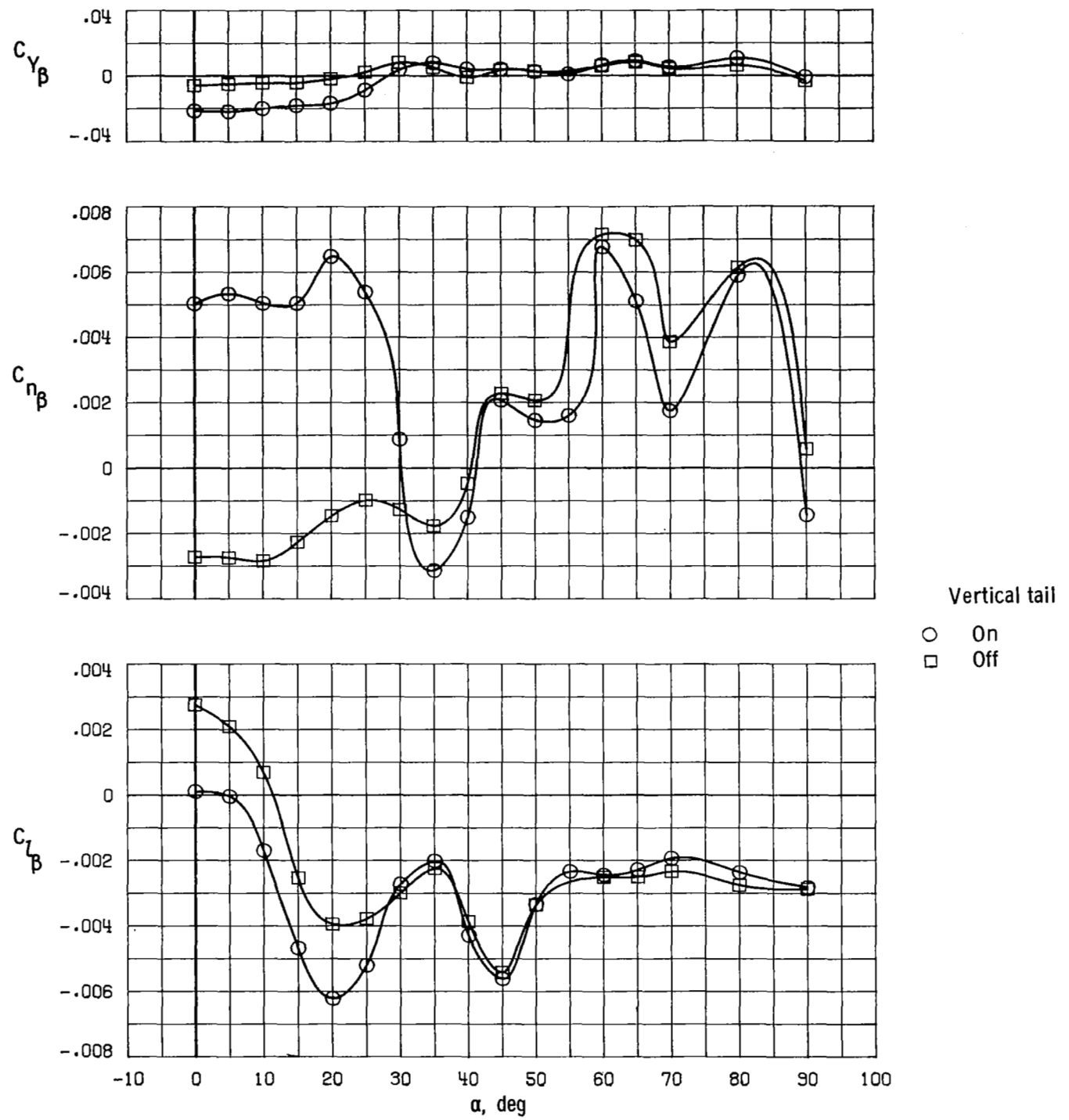

(a) $\delta_c = 0°$.

Figure 14.- Effect of vertical tail on static lateral-directional stability. $\delta_f = 17.5°$; $\delta_s = 30°$.

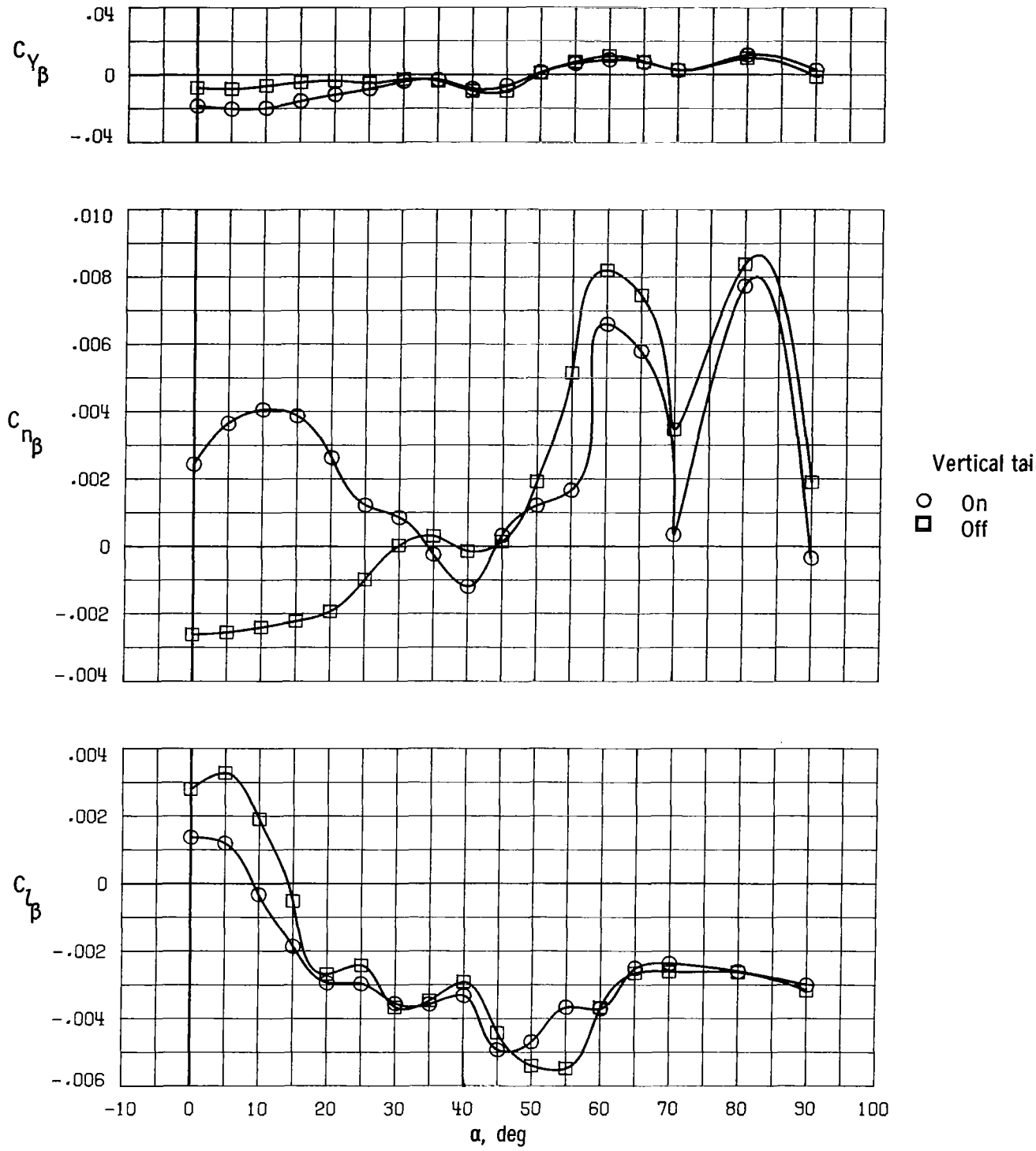

(b) $\delta_c = -25°$.

Figure 14.- Concluded.

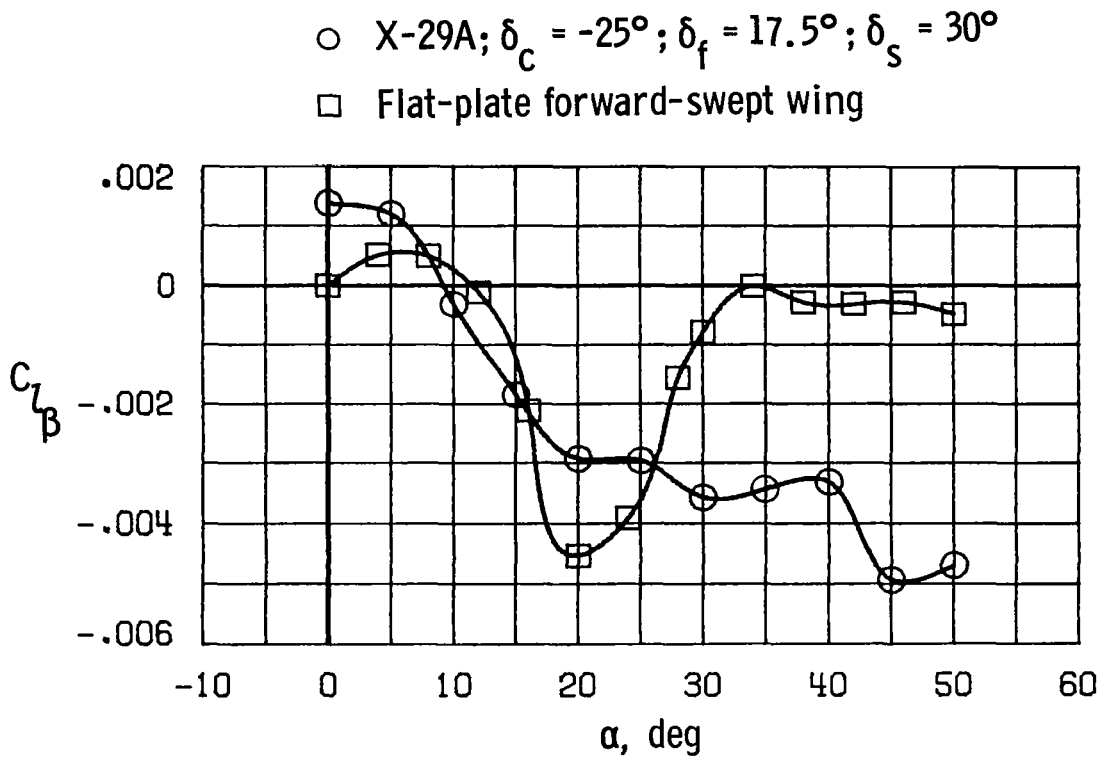

Figure 15.- Comparison of lateral stability characteristics of X-29A and flat-plate forward-swept wing.

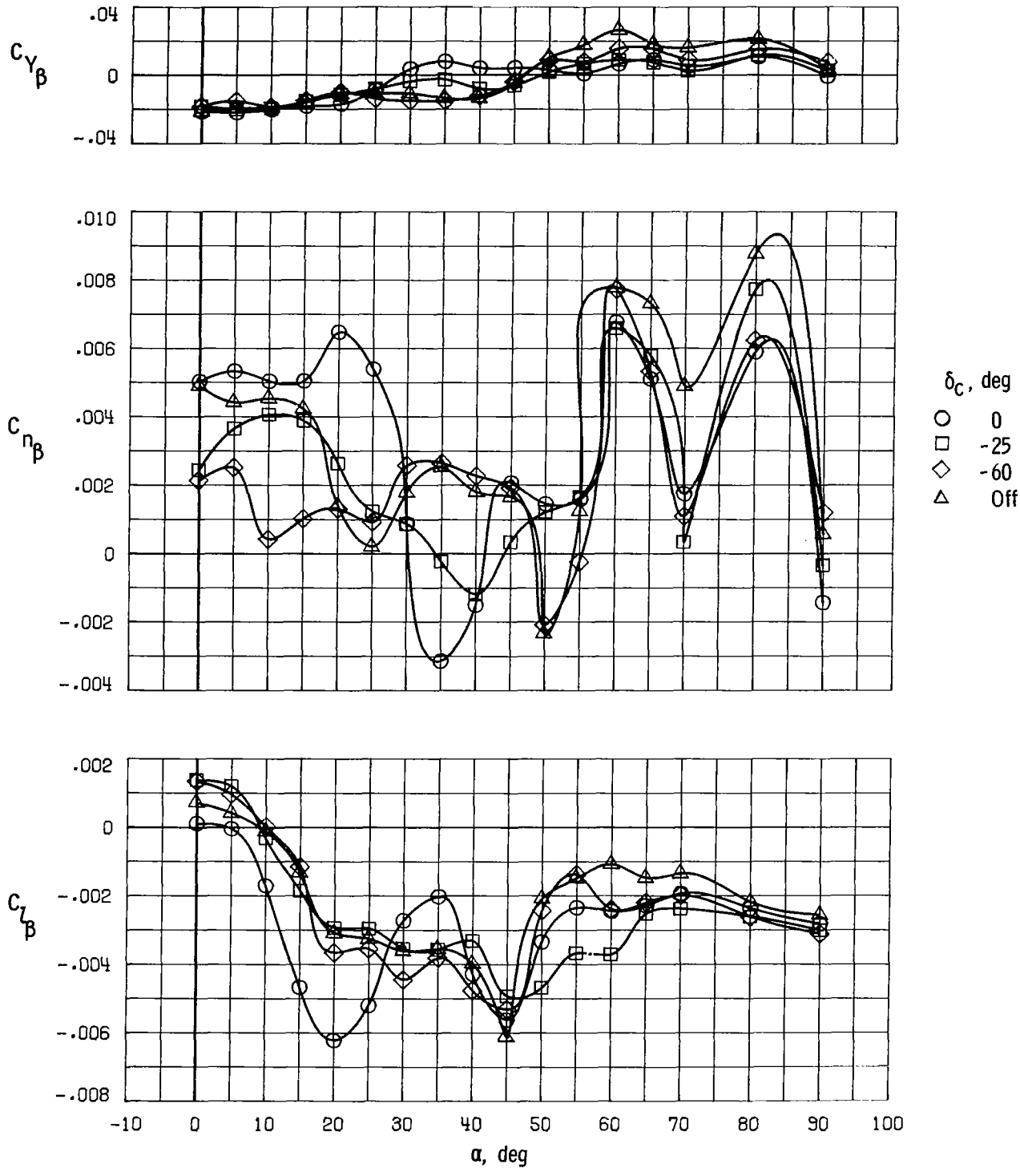

Figure 16.- Effect of canard deflection on static lateral-directional stability. $\delta_f = 17.5°$; $\delta_s = 30°$.

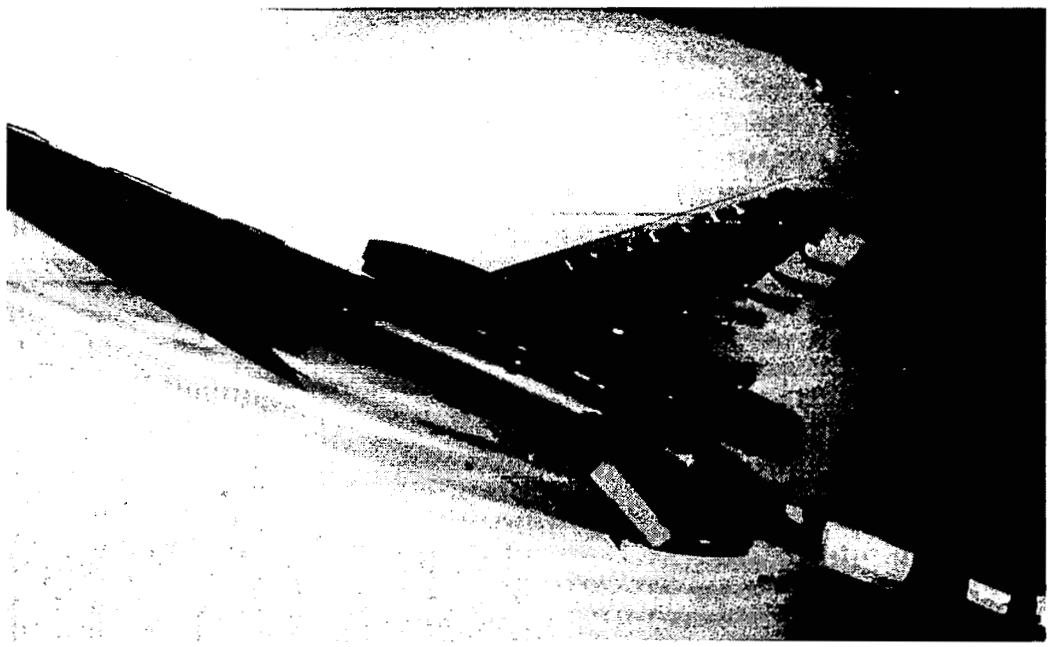

(a) Canard off.

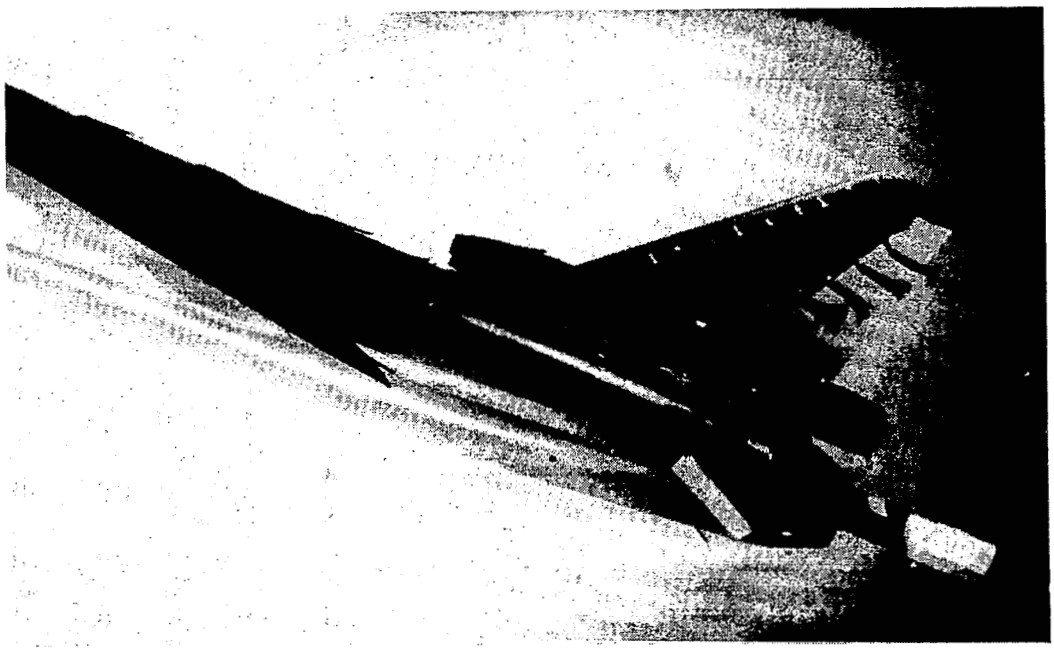

(b) Canard on. $\delta_c = 0°$.

L-83-131

Figure 17.- Tuft-flow visualization of X-29A vertical tail at $\alpha = 25°$. $\delta_f = 17.5°$; $\delta_s = 30°$.

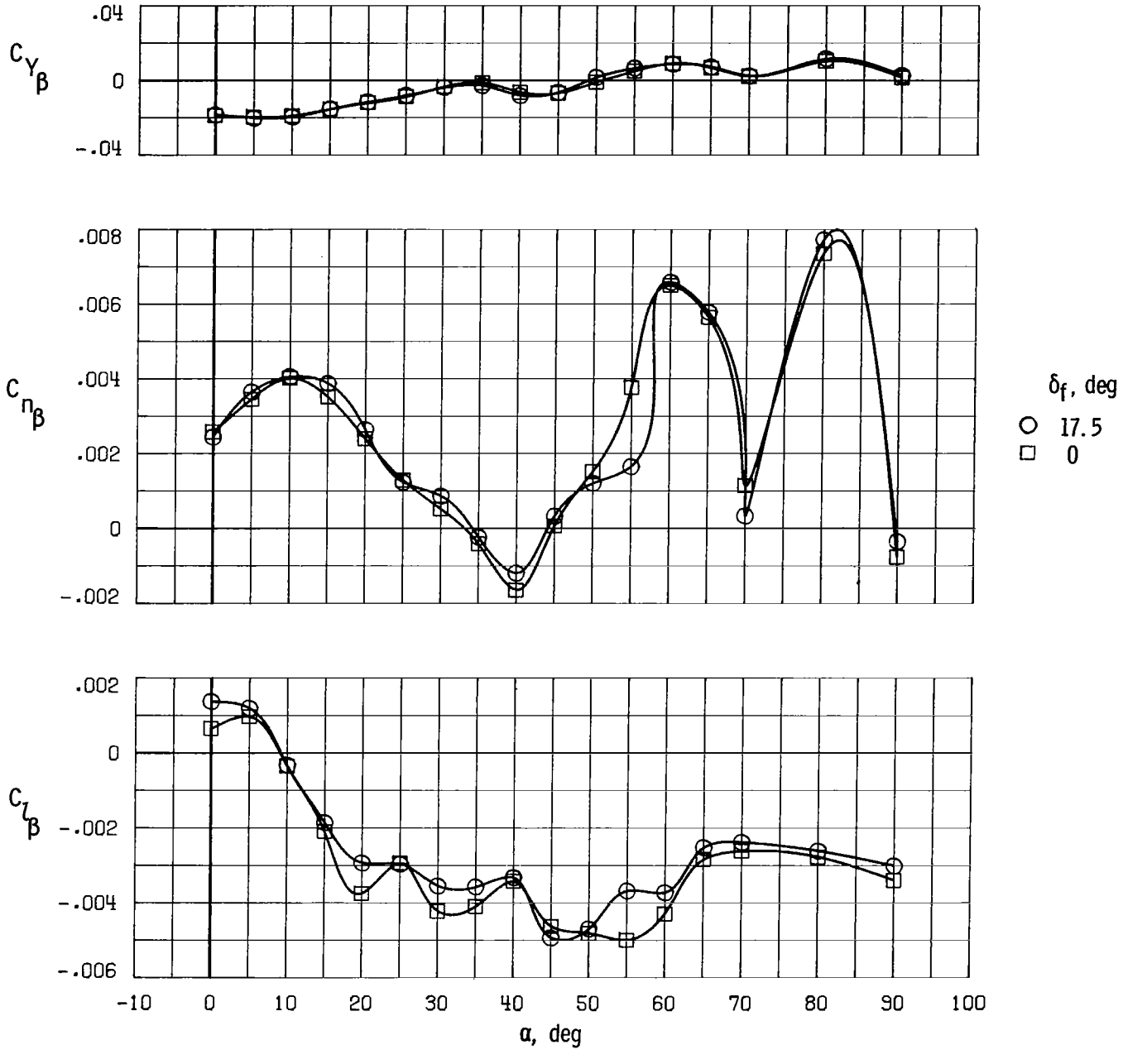

Figure 18.- Effect of flaperon deflection on static lateral-directional stability. $\delta_c = -25°$; $\delta_s = 30°$.

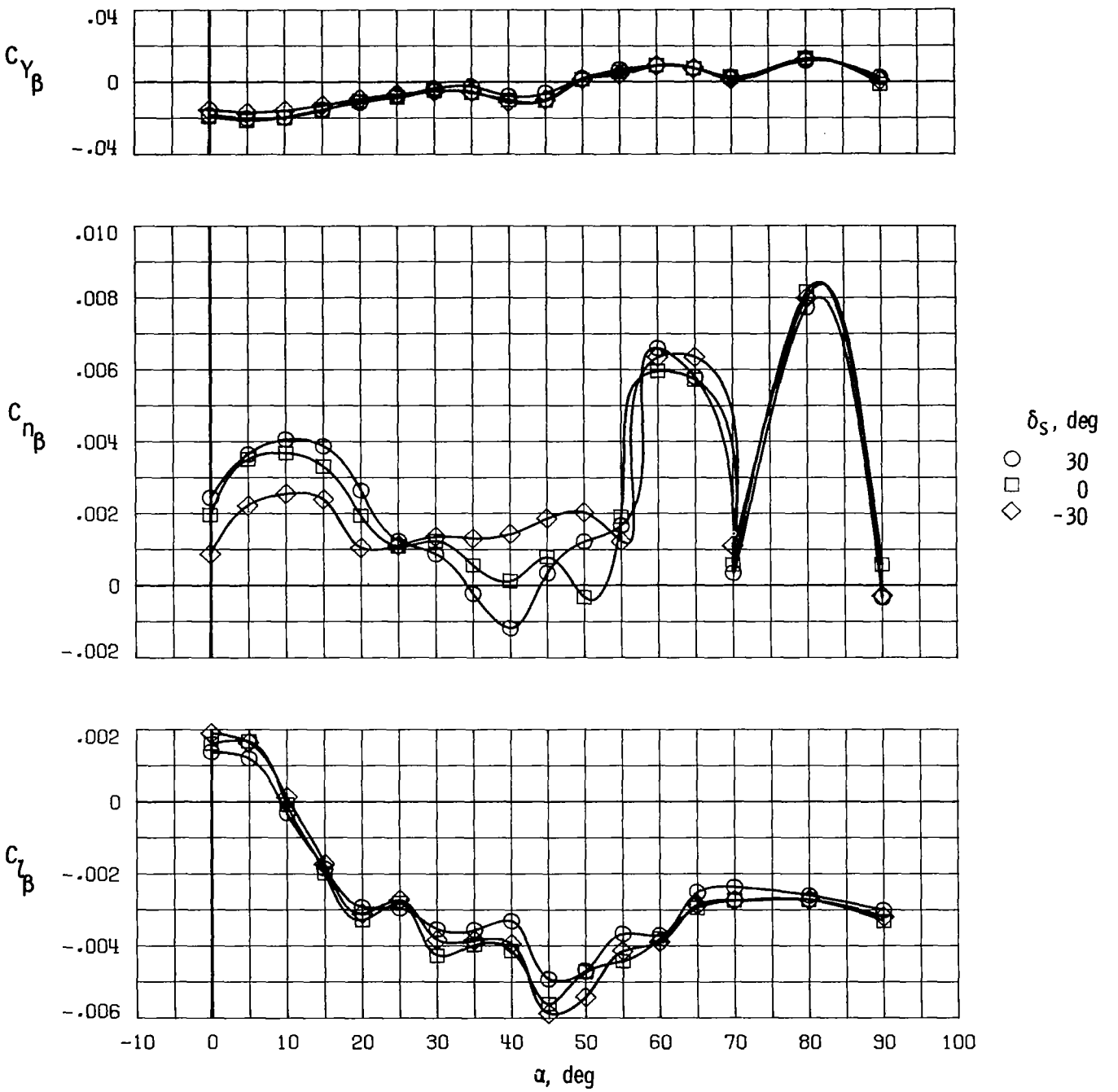

Figure 19.- Effect of strake-flap deflection on static lateral-directional stability. $\delta_c = -25°$; $\delta_f = 17.5°$.

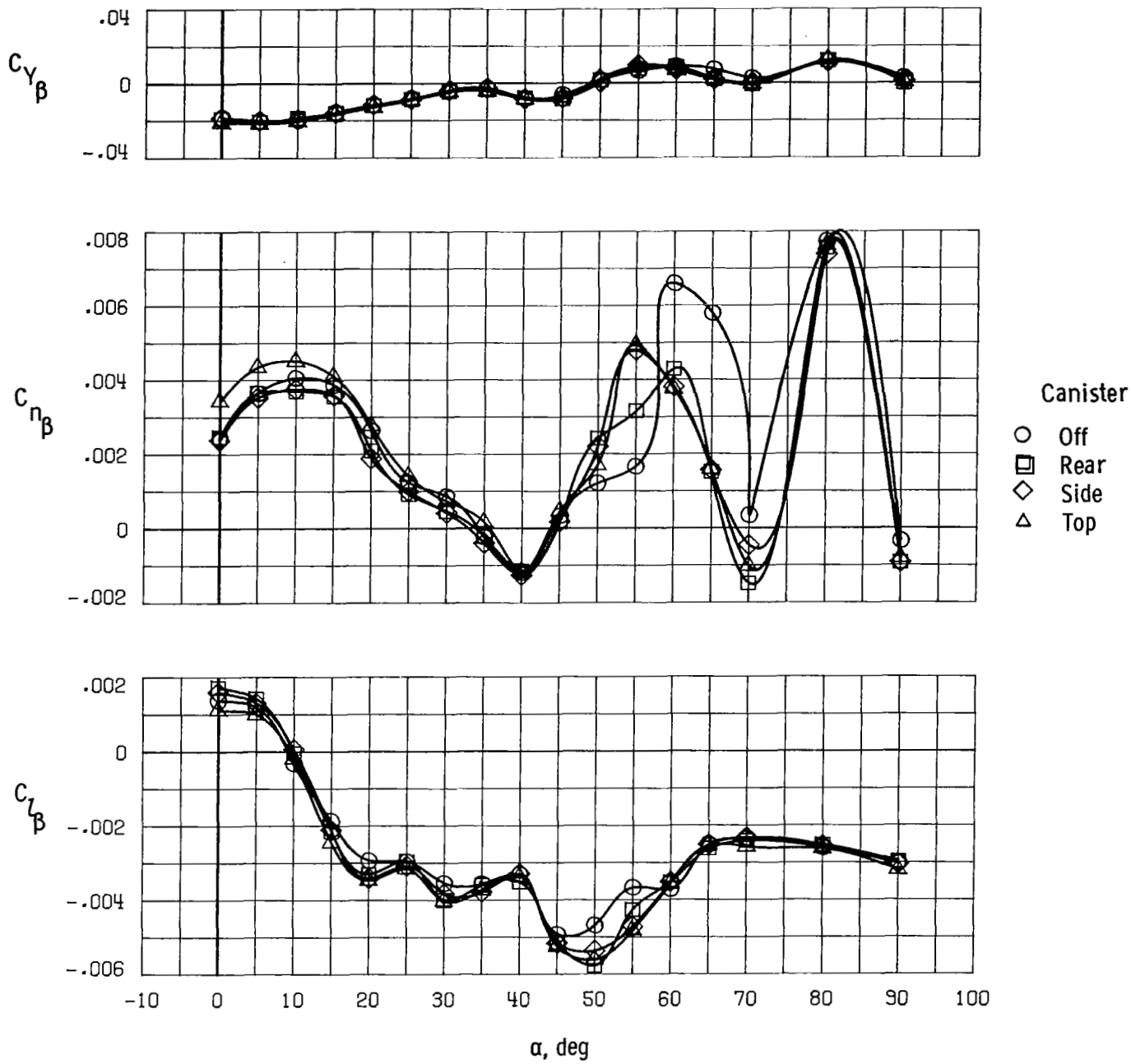

Figure 20.- Effect of spin-chute canister location on static lateral-directional stability. $\delta_c = -25°$; $\delta_f = 17.5°$; $\delta_s = 30°$.

Error

An error occurred while processing this page. See the system log for more details.

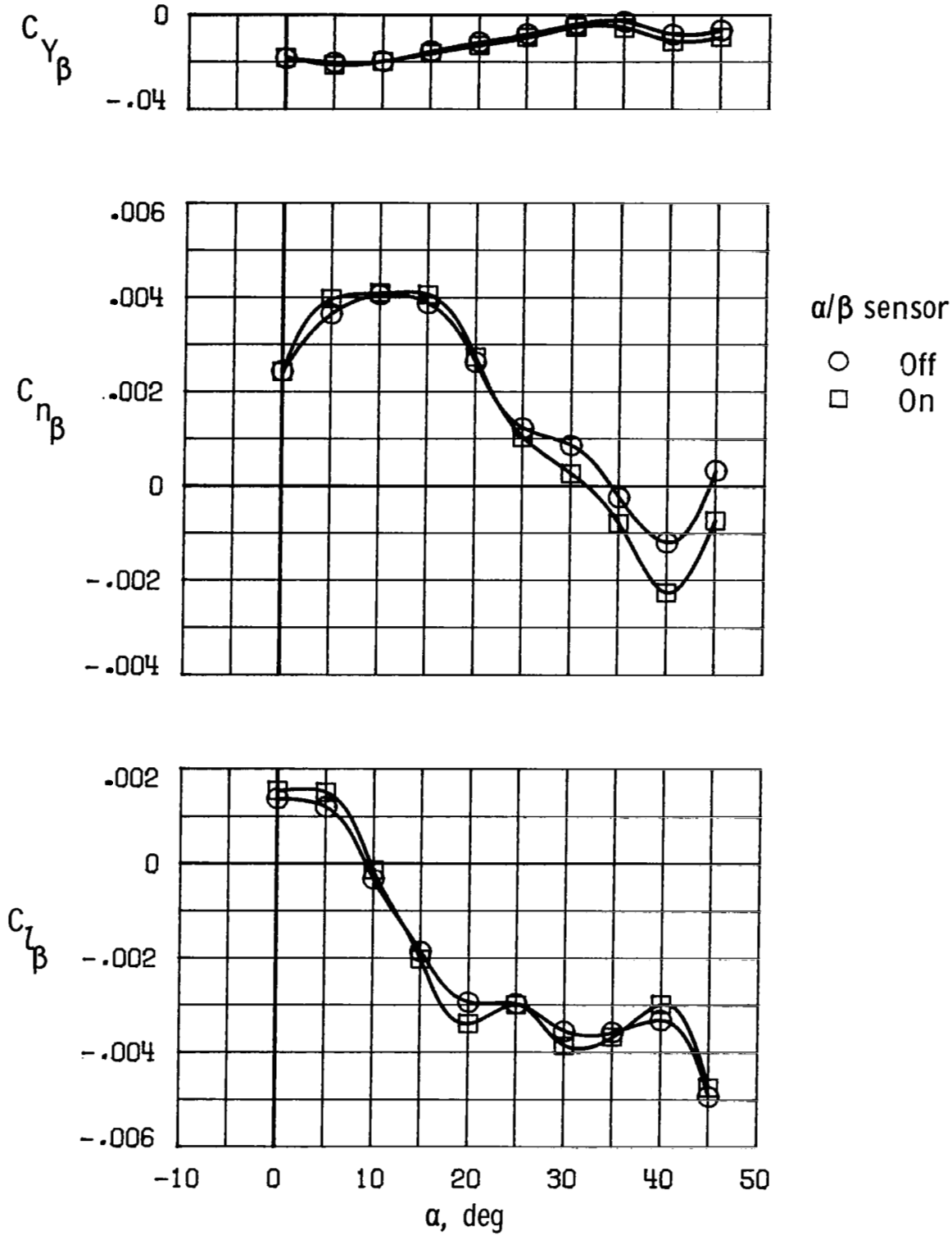

Figure 22.- Effect of boom-mounted α/β vane sensor on static lateral-directional stability. $\delta_c = -25°$; $\delta_f = 17.5°$; $\delta_s = 30°$.

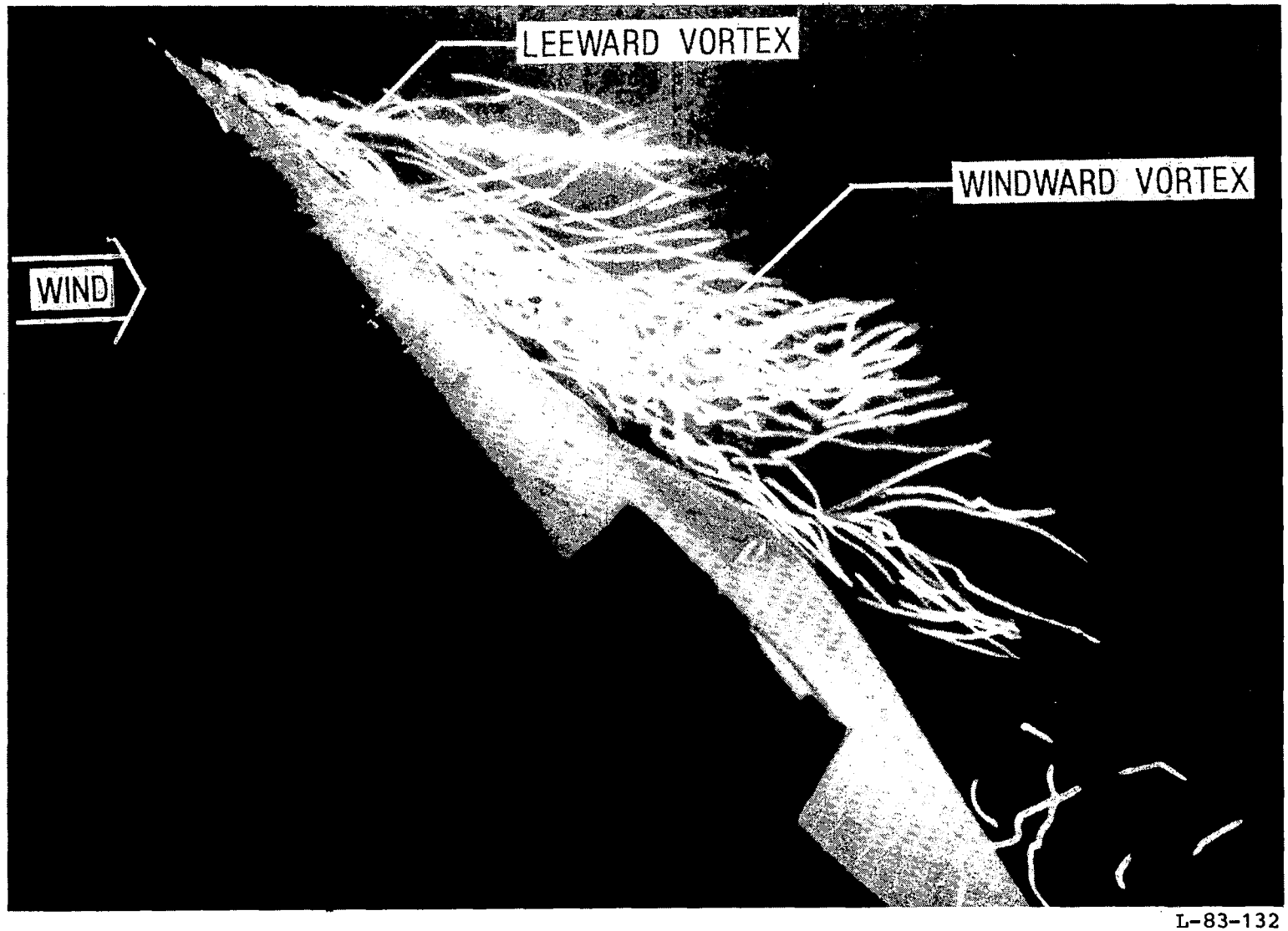

L-83-132

Figure 23.- Helium-bubble flow visualization of X-29A forebody flow at high angles of attack.

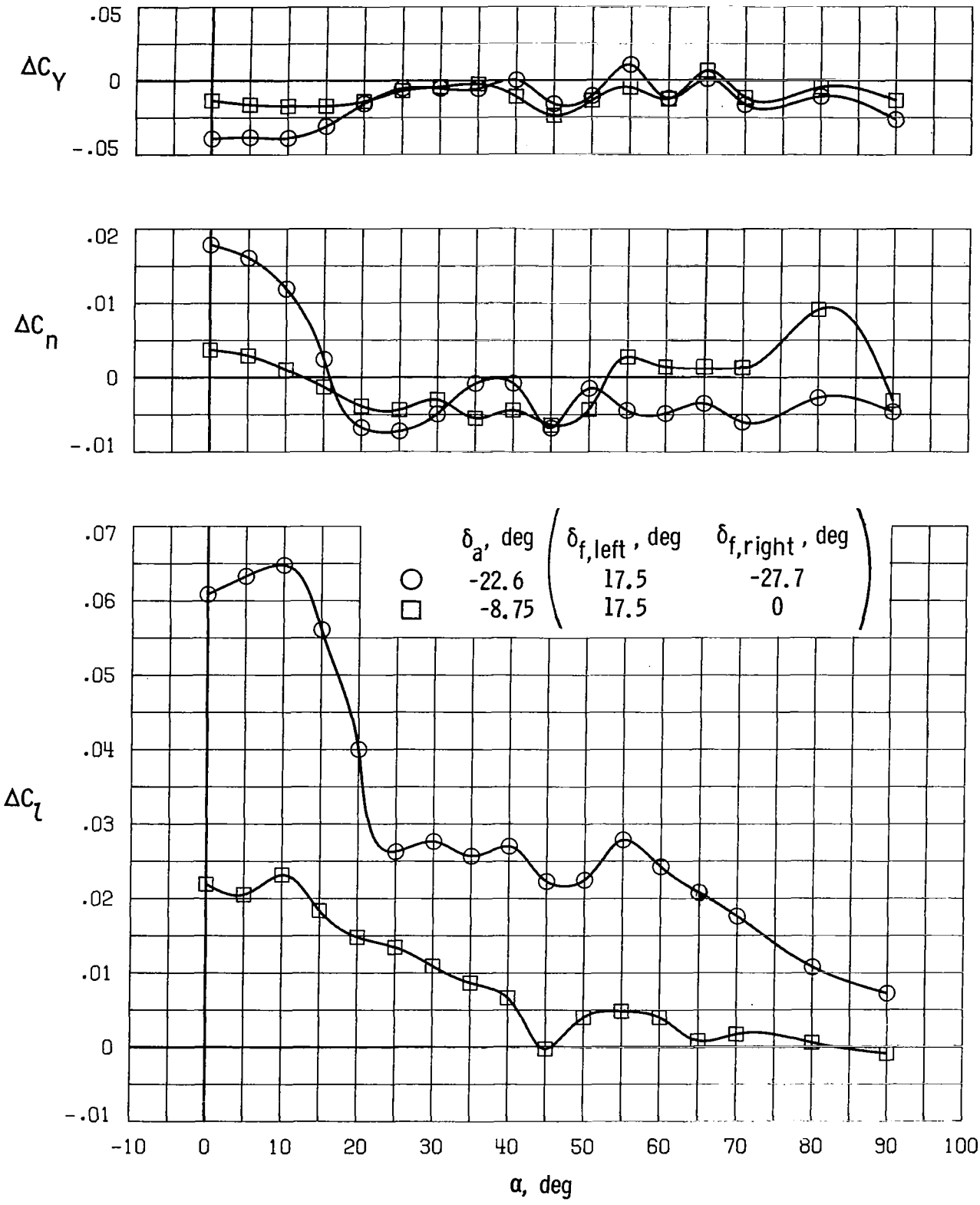

Figure 24.- Effect of aileron deflection. $\delta_c = -25°$; $\delta_s = 30°$.

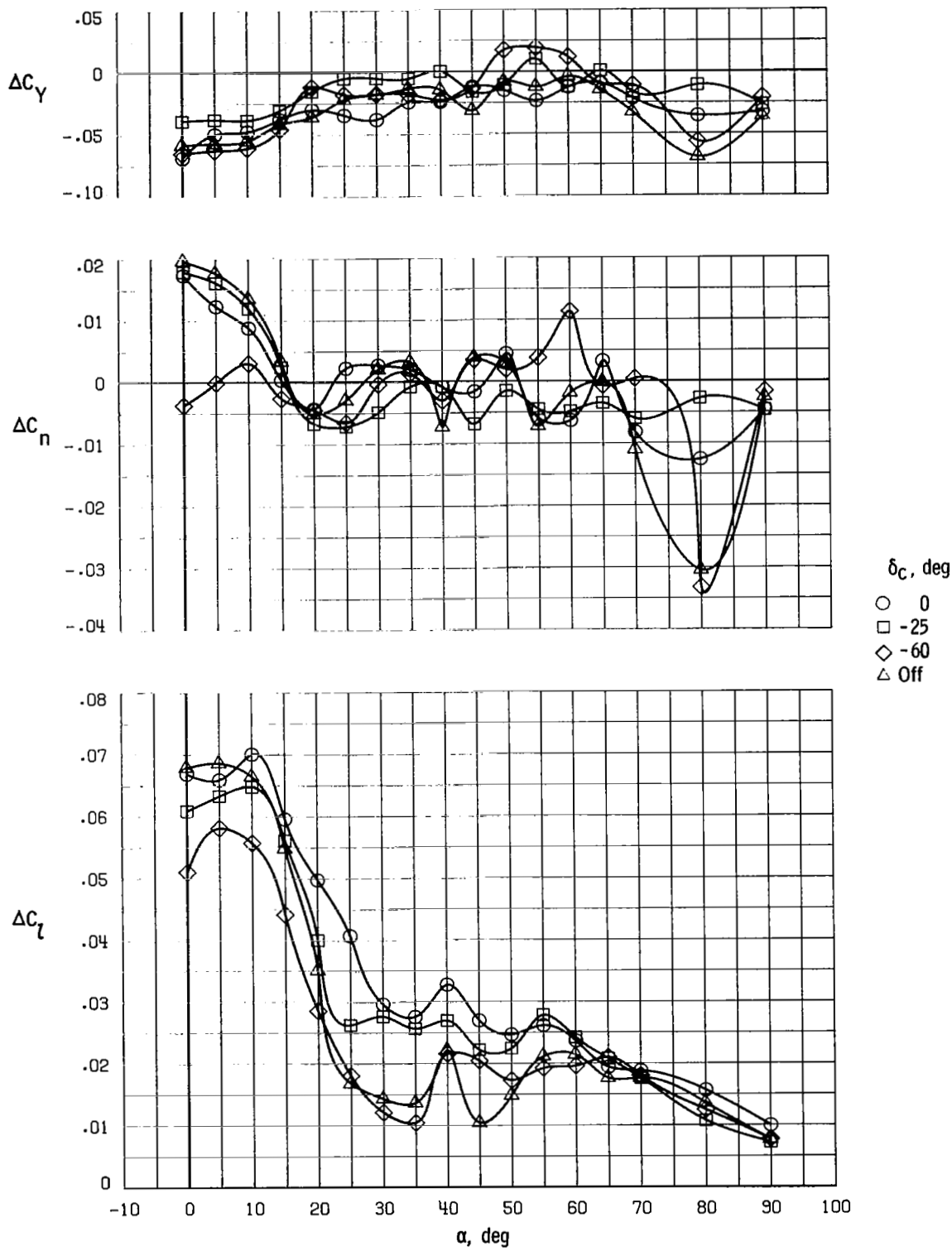

Figure 25.- Effect of canard deflection on aileron effectiveness. δ_a = -22.6° ($\delta_{f,left}$ = 17.5°; $\delta_{f,right}$ = -27.7°); δ_s = 30°.

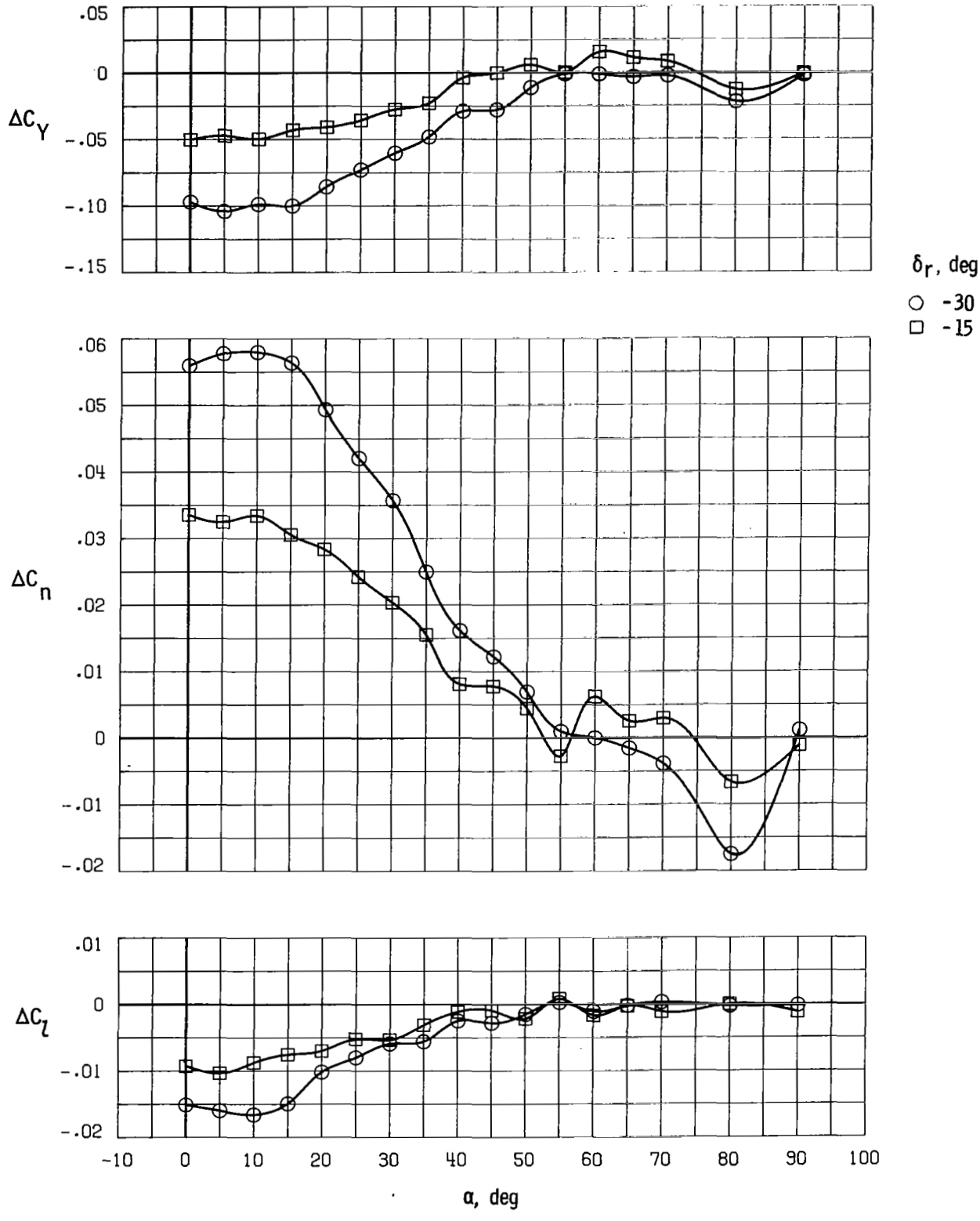

Figure 26.- Effect of rudder deflection. $\delta_c = -25°$; $\delta_f = 17.5°$; $\delta_s = 30°$.

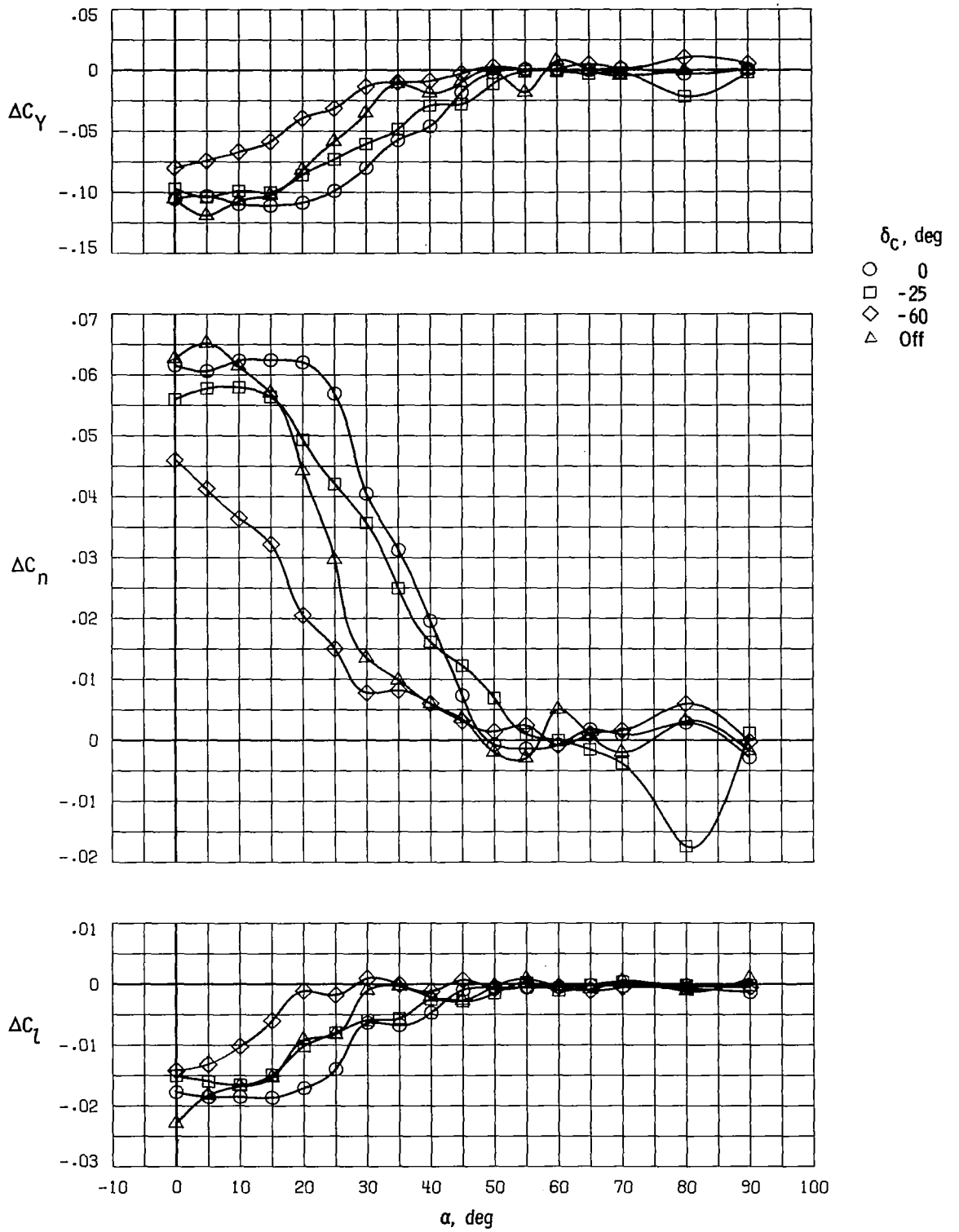

Figure 27.- Effect of canard deflection on rudder effectiveness. $\delta_r = -30°$; $\delta_f = 17.5°$; $\delta_s = 30°$.

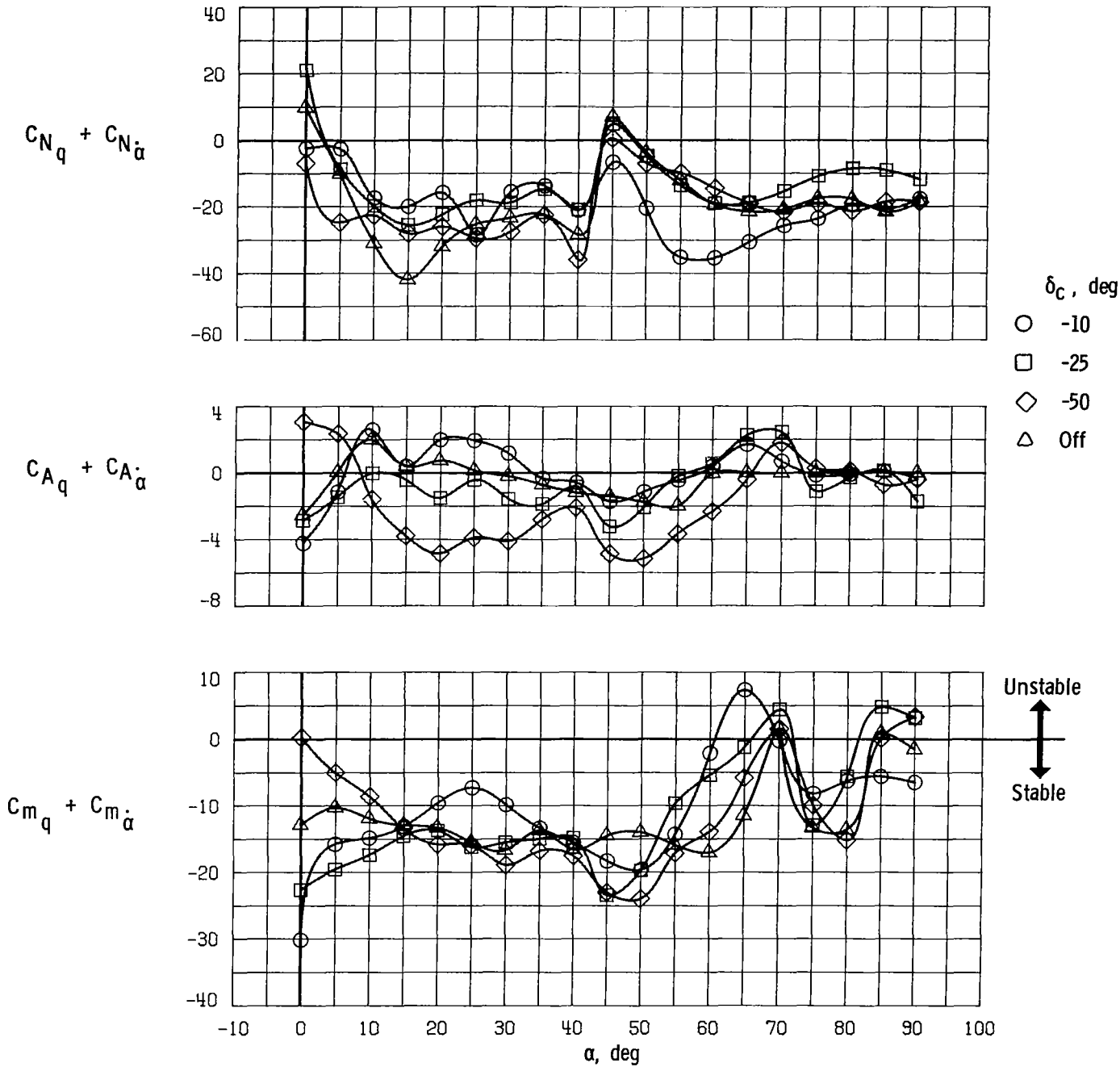

Figure 28.- Effect of canard deflection on dynamic longitudinal stability derivatives obtained during pitching-oscillation tests. $\delta_f = 20°$; $\delta_s = 30°$; $\Delta\theta = \pm 5°$.

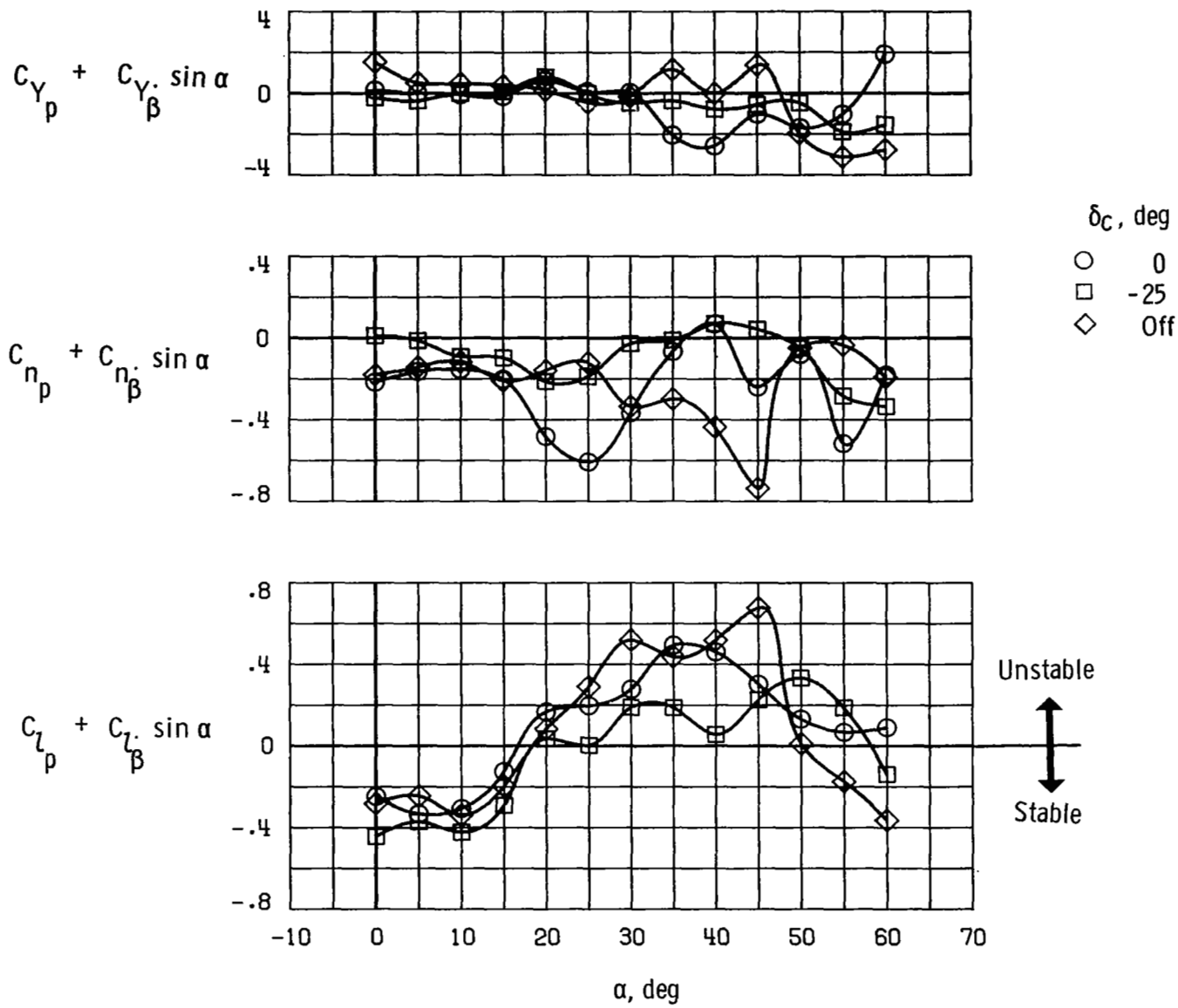

Figure 29.- Effect of canard deflection on dynamic lateral-directional stability derivatives obtained during rolling-oscillation tests. $\delta_f = 20°$; $\delta_s = 30°$; $\Delta\phi = \pm 10°$.

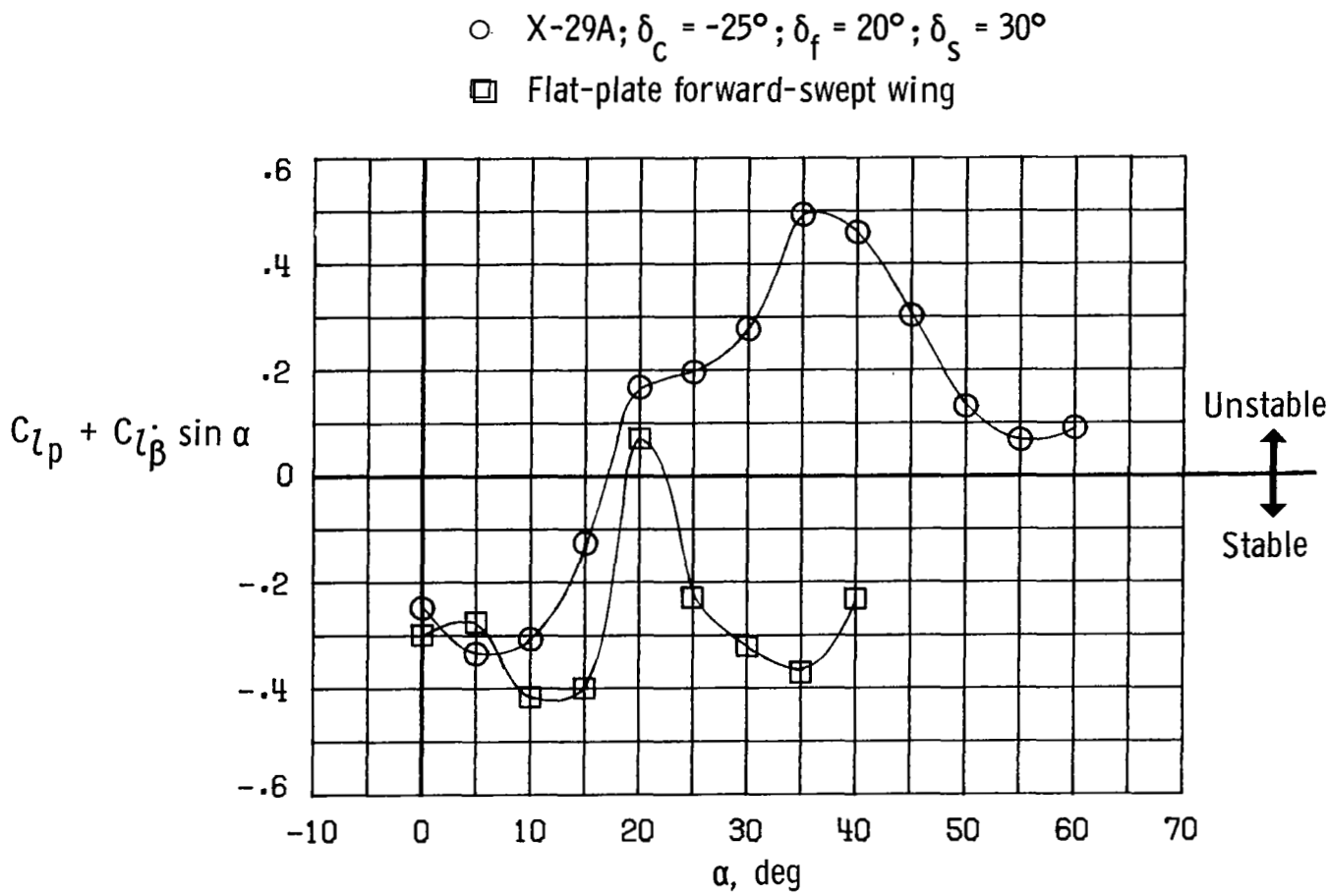

Figure 30.- Comparison of roll-damping characteristics of X-29A and flat-plate forward-swept wing. $\Delta\phi = \pm 10°$.

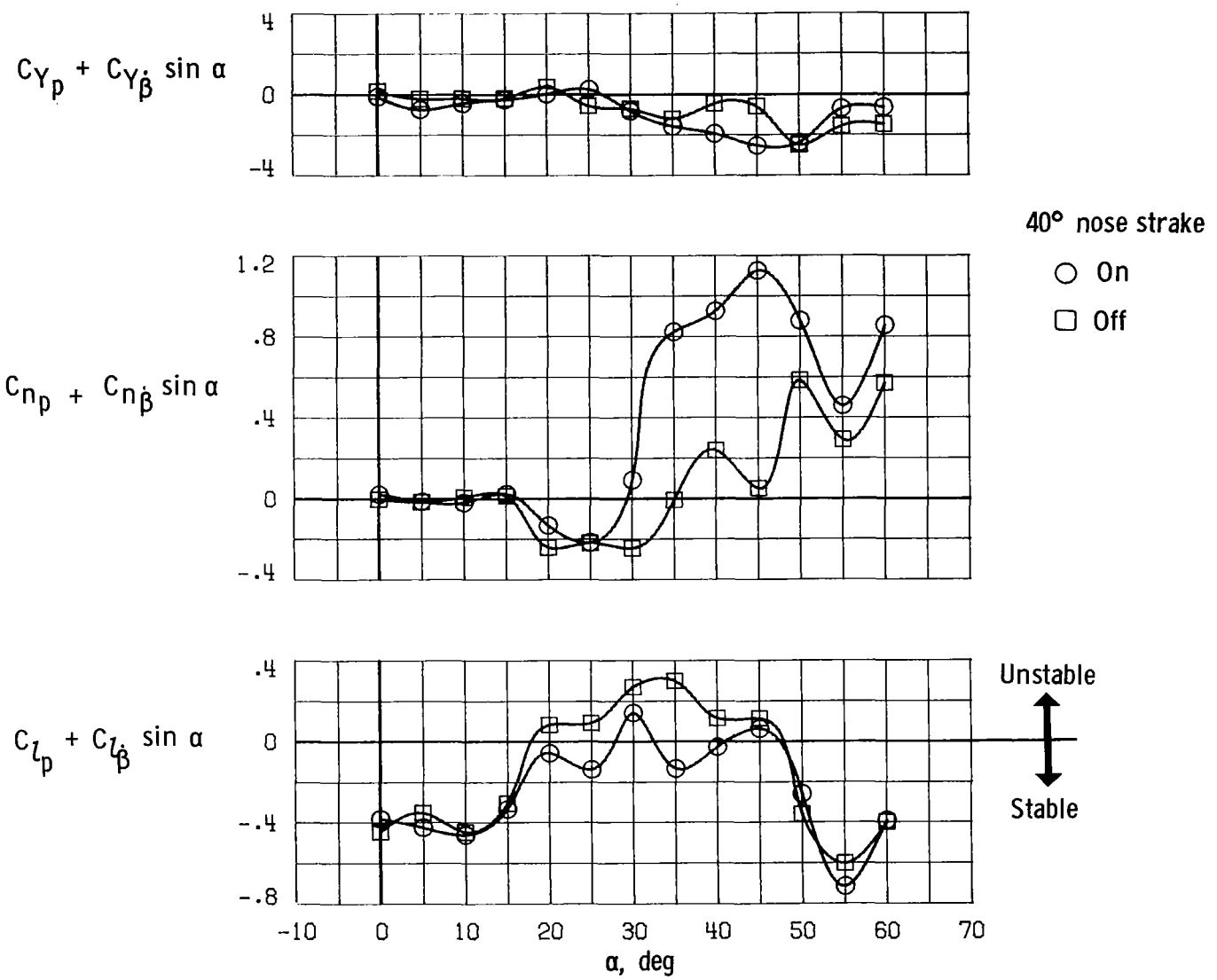

Figure 31.- Effect of 40° nose strakes on dynamic lateral-directional stability derivatives obtained during rolling-oscillation tests. $\delta_c = -25°$; $\delta_f = 20°$; $\delta_s = 30°$; $\Delta\phi = \pm 5°$.

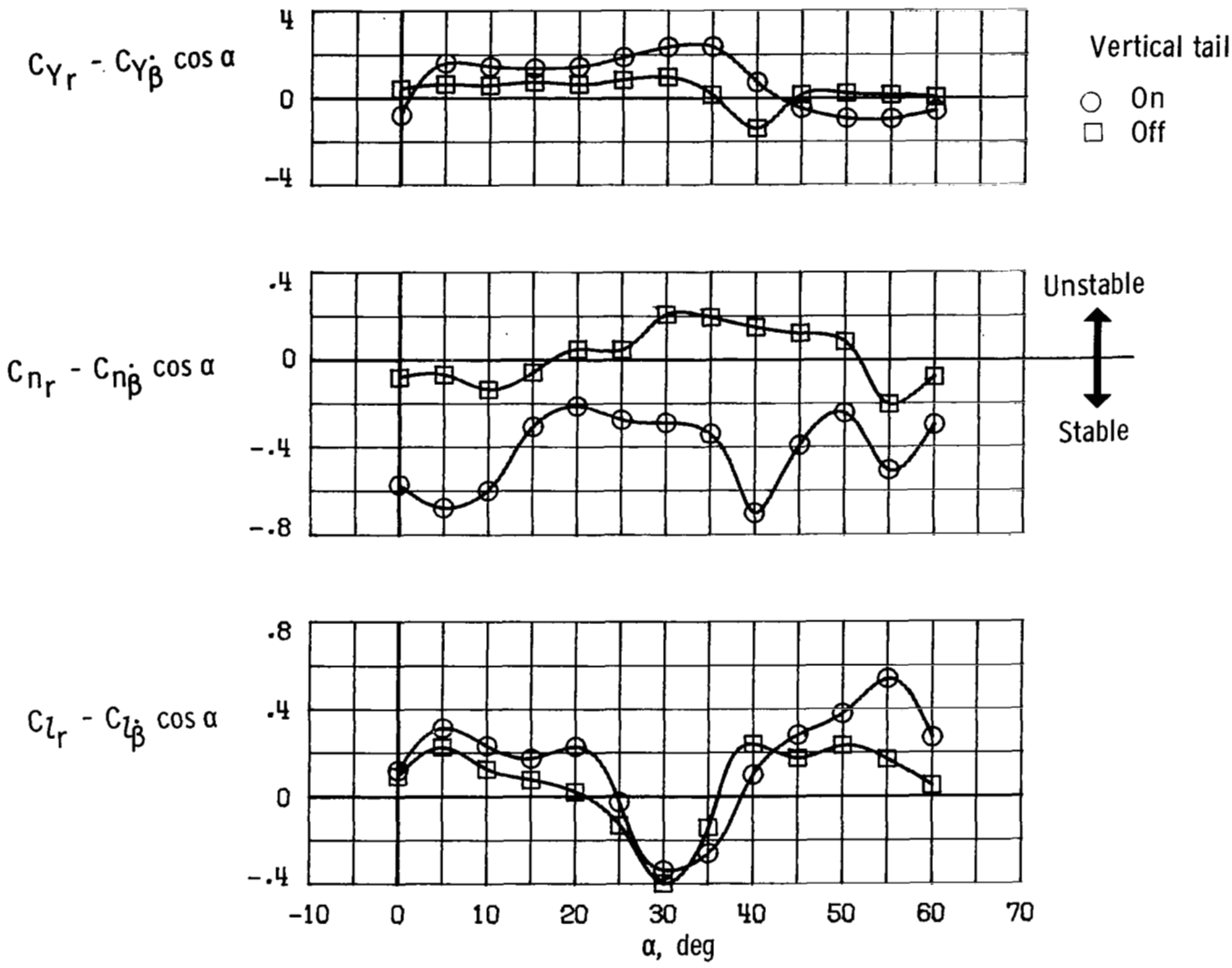

Figure 32.- Effect of vertical tail on dynamic lateral-directional stability derivatives obtained during yawing-oscillation tests. $\delta_c = -25°$; $\delta_f = 20°$; $\delta_s = 30°$; $\Delta\psi = \pm 5°$.

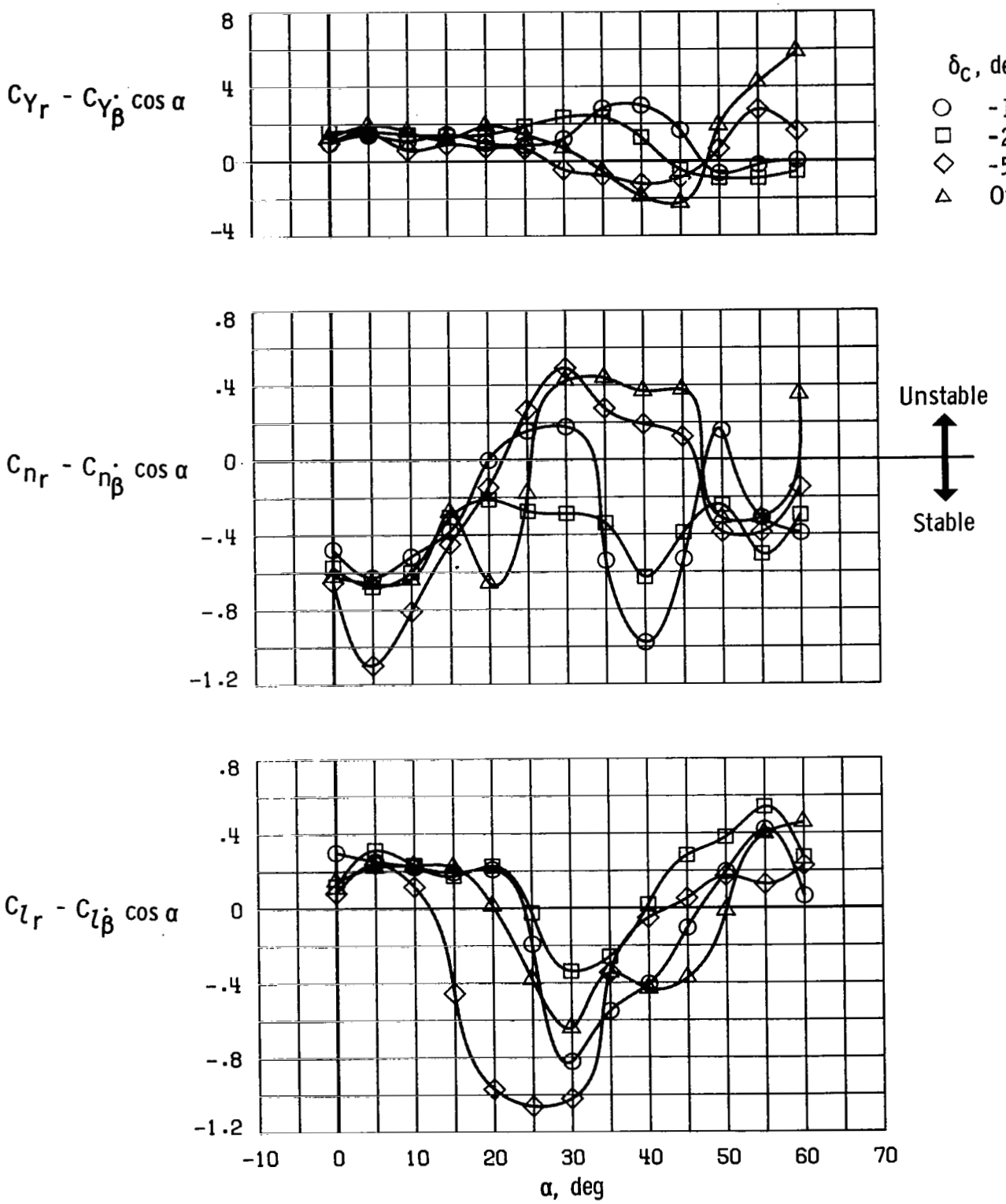

Figure 33.- Effect of canard deflection on dynamic lateral-directional stability derivatives obtained during yawing-oscillation tests. δ_f = 20°; δ_s = 30°; $\Delta\psi$ = ±5°.

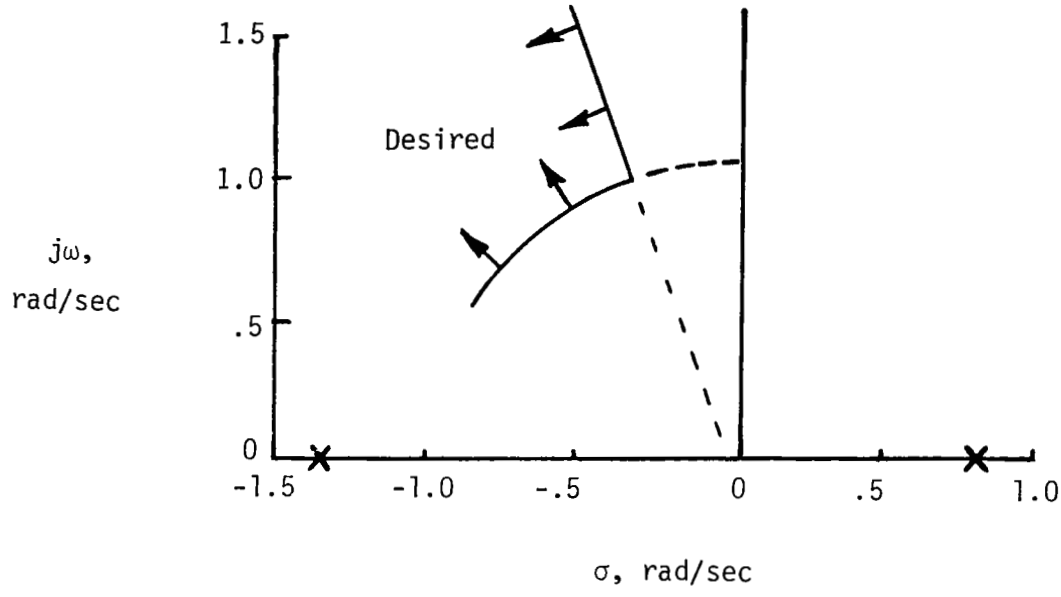

(a) Unaugmented. t_2 = 0.85 sec.

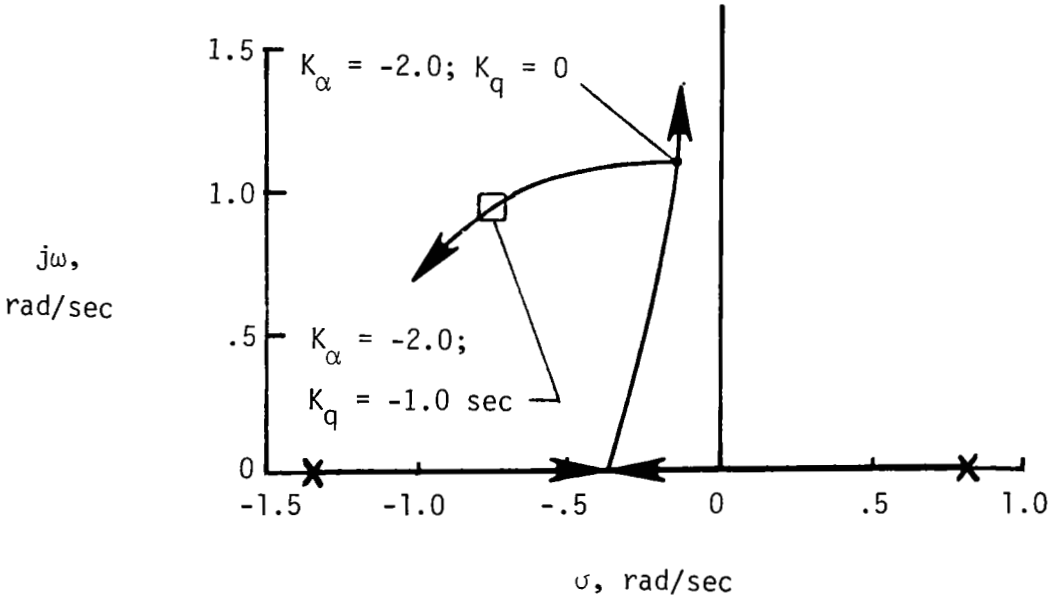

(b) Augmented. ω_n = 1.17 rad/sec; ζ = 0.65; $t_{1/2}$ = 0.91 sec.

Figure 34.- Root-locus representation of pitch-stability-augmentation, short-period characteristics with α = 30°. Values shown are for full-scale airplane.

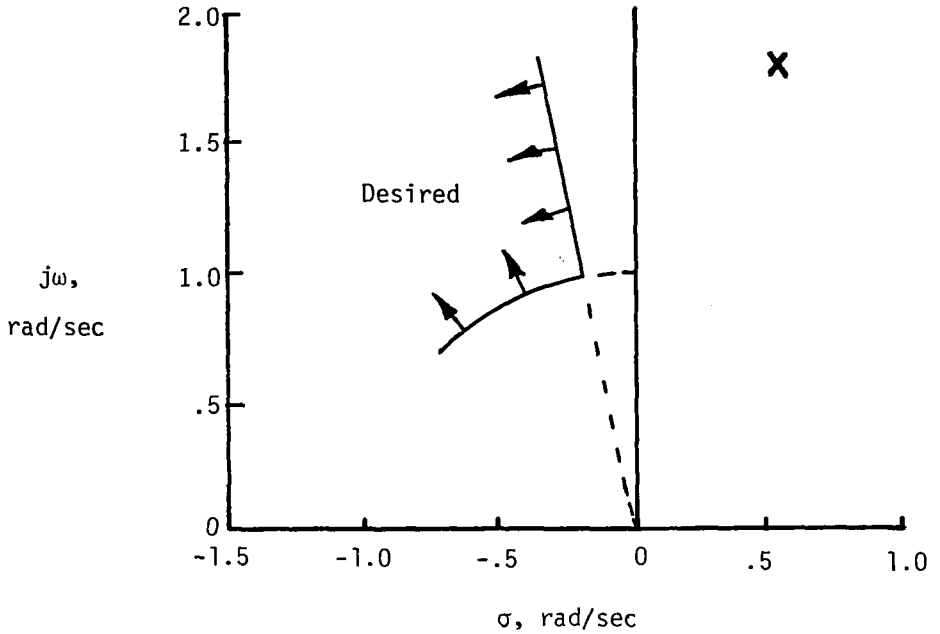

(a) Unaugmented. t_2 = 1.20 sec.

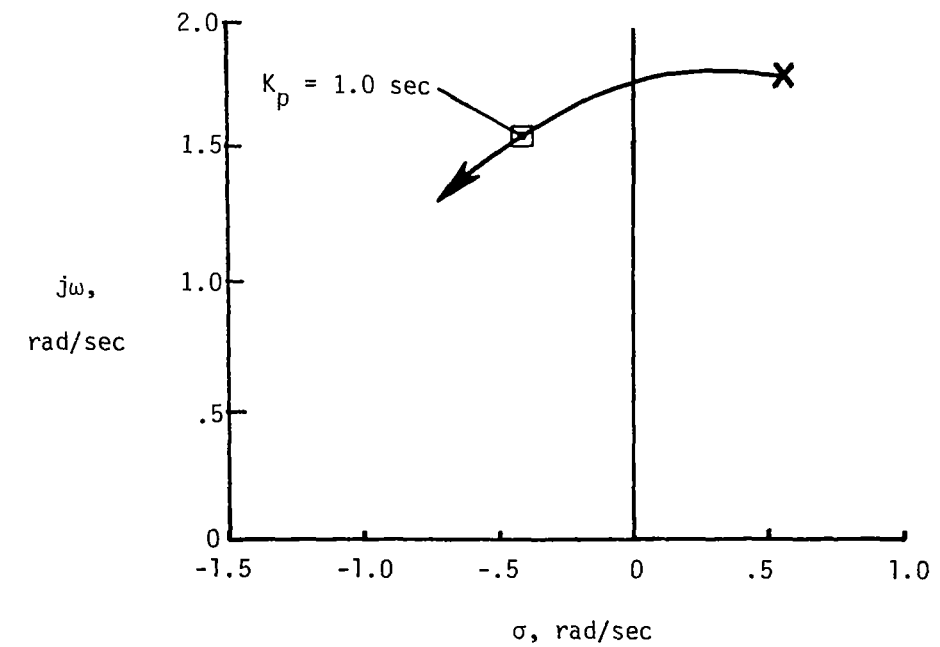

(b) Augmented. ω_n = 1.63 rad/sec; ζ = 0.26; $t_{1/2}$ = 1.65 sec.

Figure 35.- Root-locus representation of roll-stability-augmentation, Dutch roll characteristics with α = 30°. Values shown are for full-scale airplane.

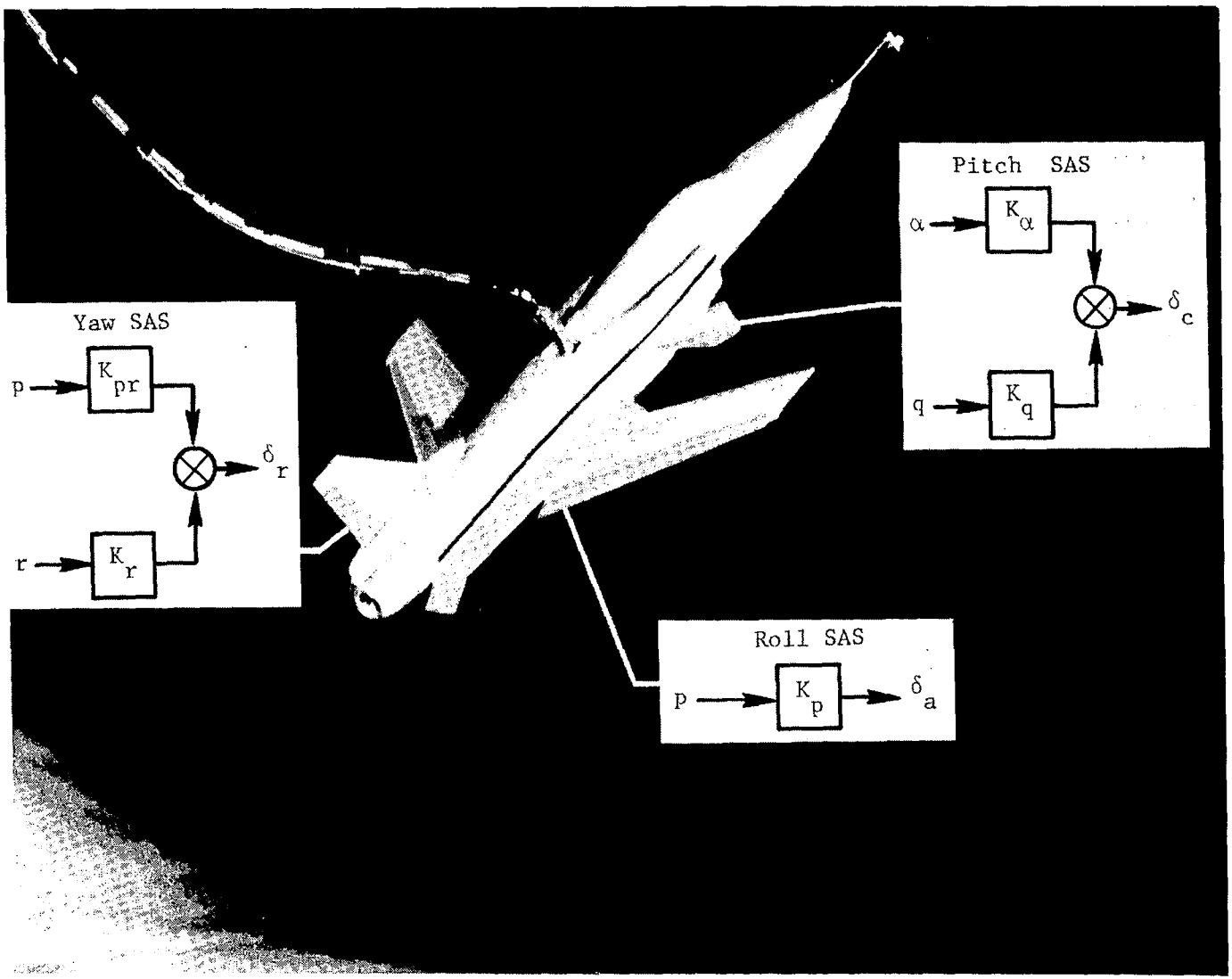

L-83-133

Figure 36.- Stability augmentation system.

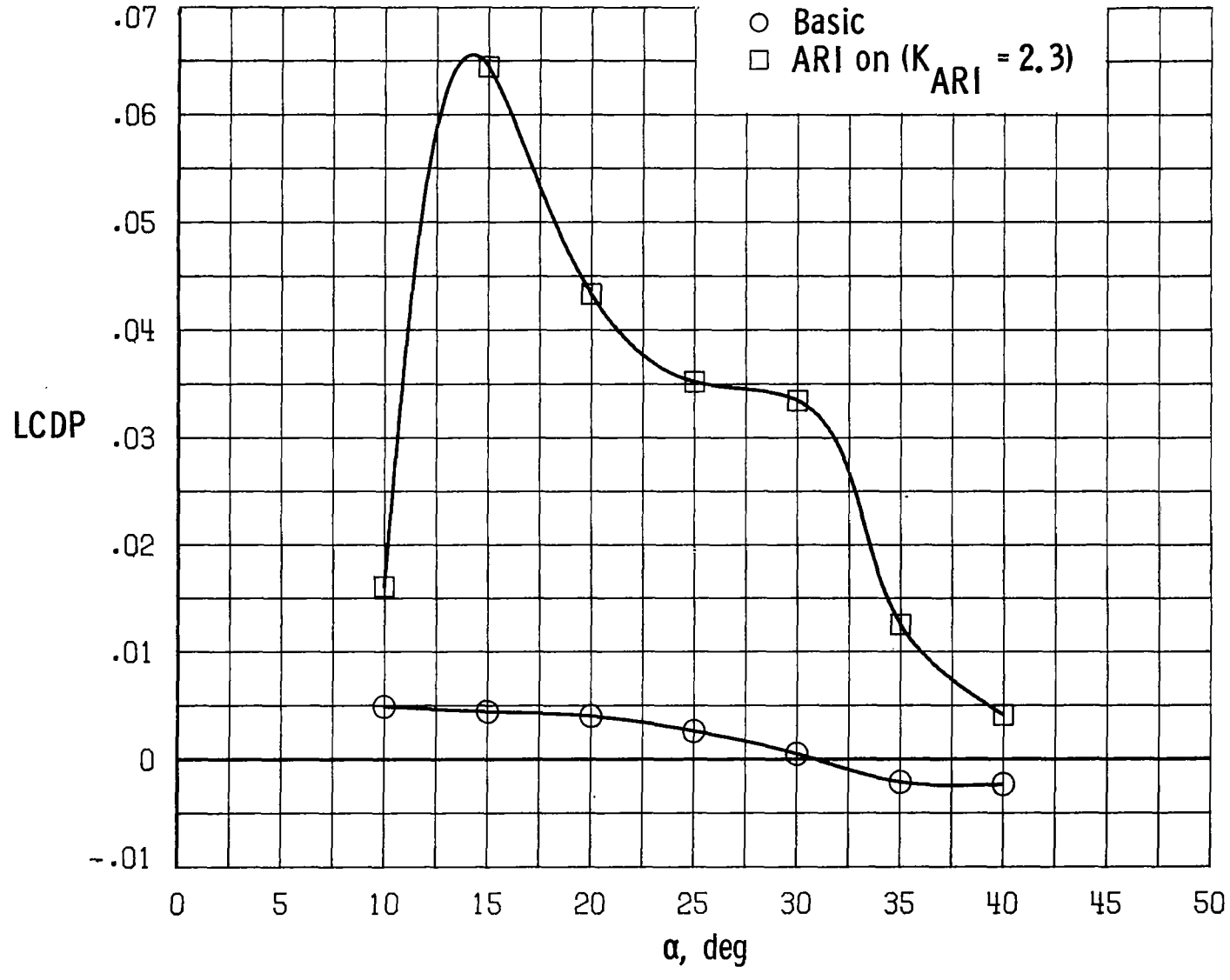

Figure 37.- Effect of ARI on lateral control divergence parameter. δ_c = Trim; δ_f = 17.5°; δ_s = 30°.

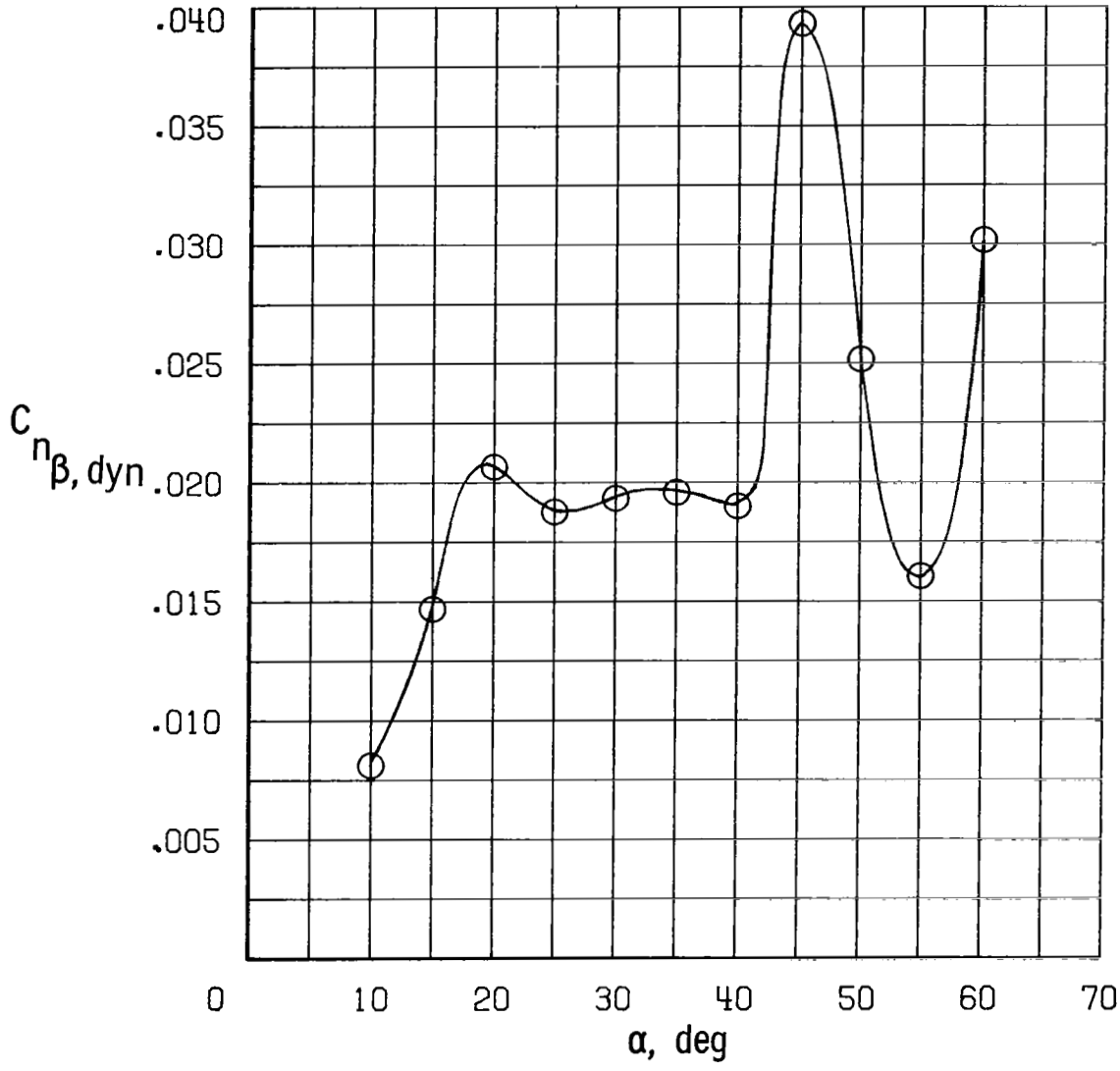

Figure 38.- Variation of $C_{n_{\beta,dyn}}$ with angle of attack. δ_c = Trim; δ_f = 17.5°; δ_s = 30°.

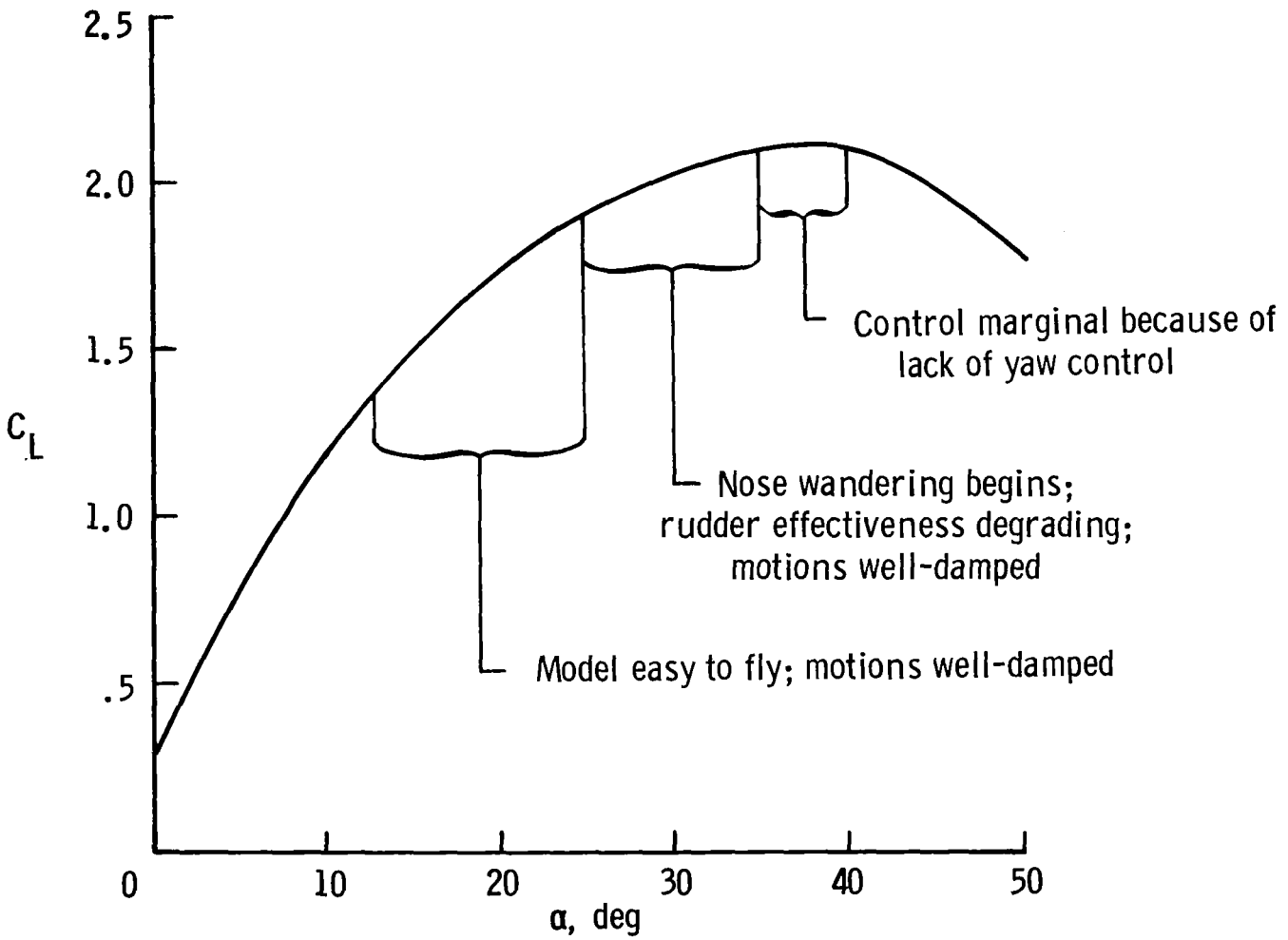

Figure 39.- Model lateral-directional flight characteristics with full augmentation.

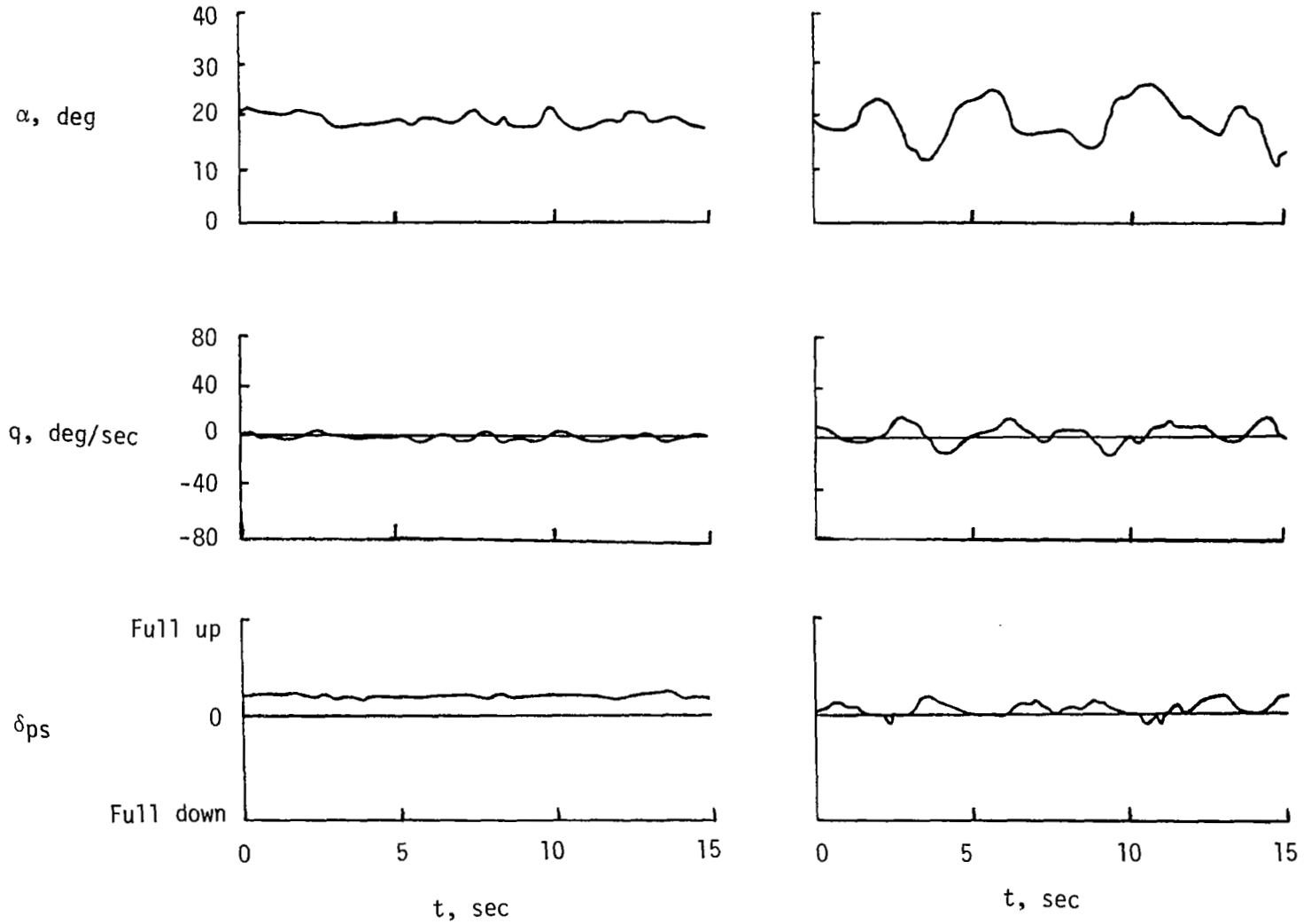

(a) Baseline SAS.

(b) Reduced-gain SAS.

Figure 40.- Effect of pitch SAS on model flight characteristics. Values shown are in model scale.

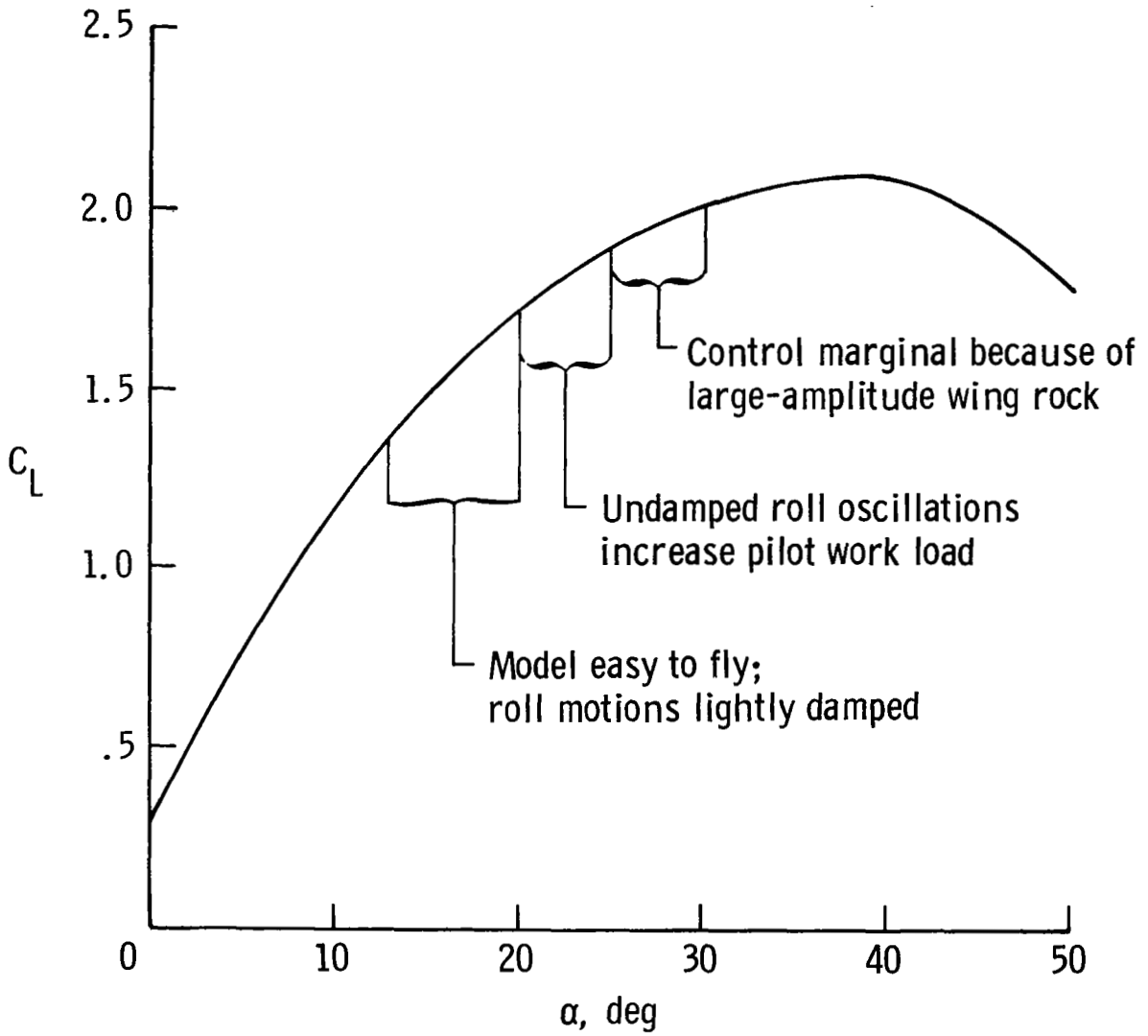

Figure 41.- Model lateral-directional flight characteristics without roll augmentation.

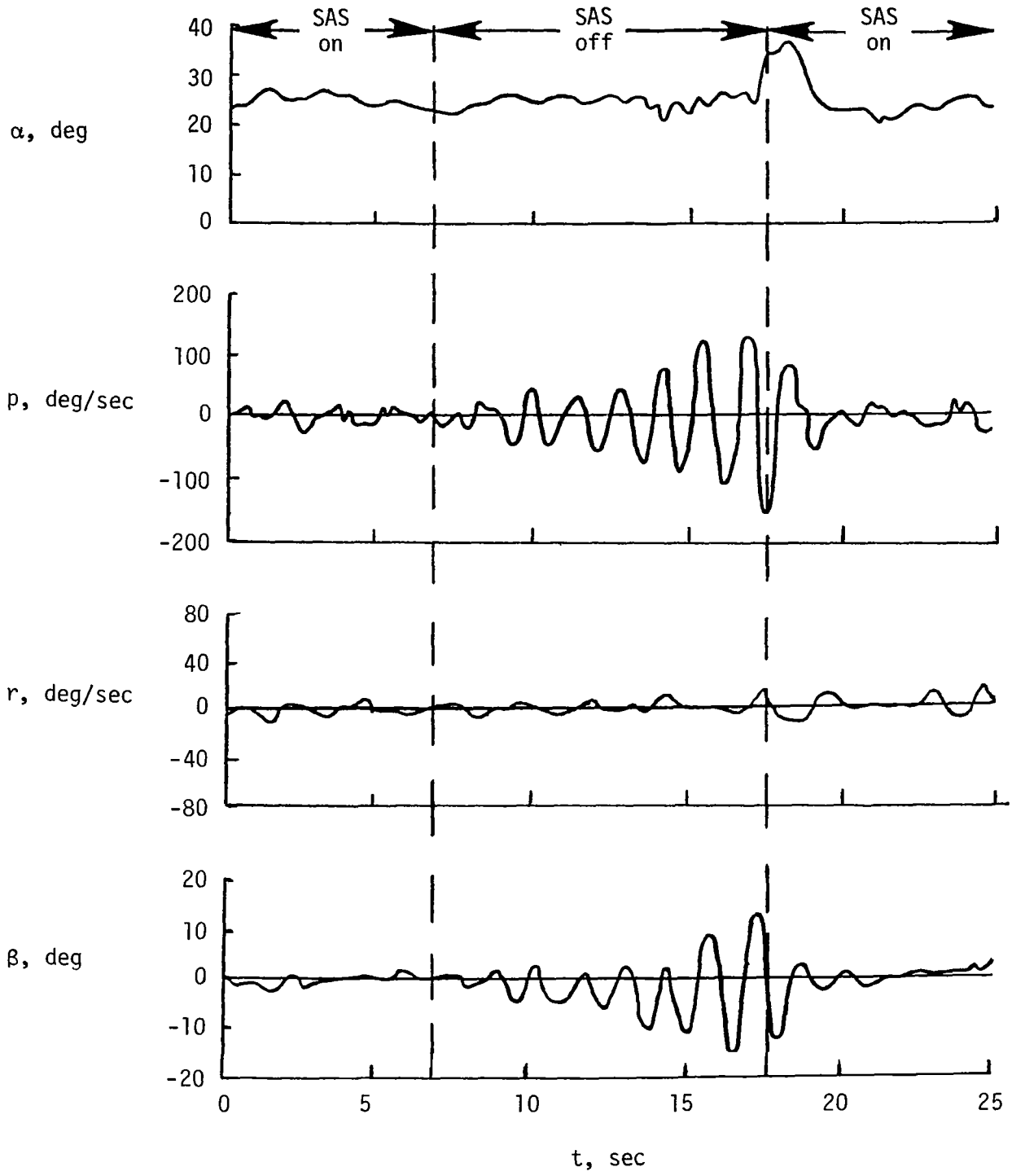

Figure 42.- Effect of roll SAS on model flight characteristics. Values shown are in model scale.

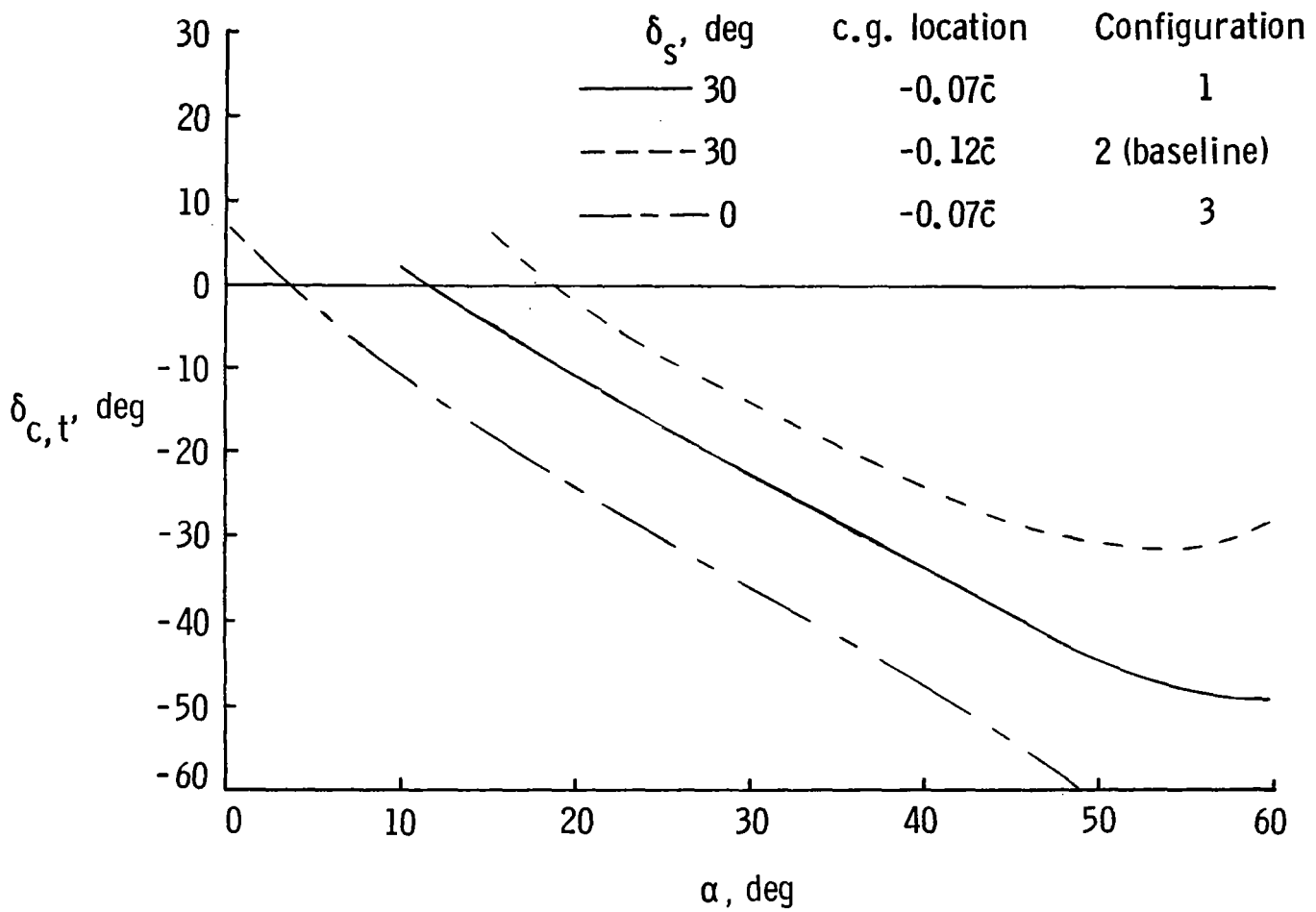

Figure 43.- Effect of c.g. location and strake-flap deflection on $\delta_{c,t}$; δ_f = 17.5°.

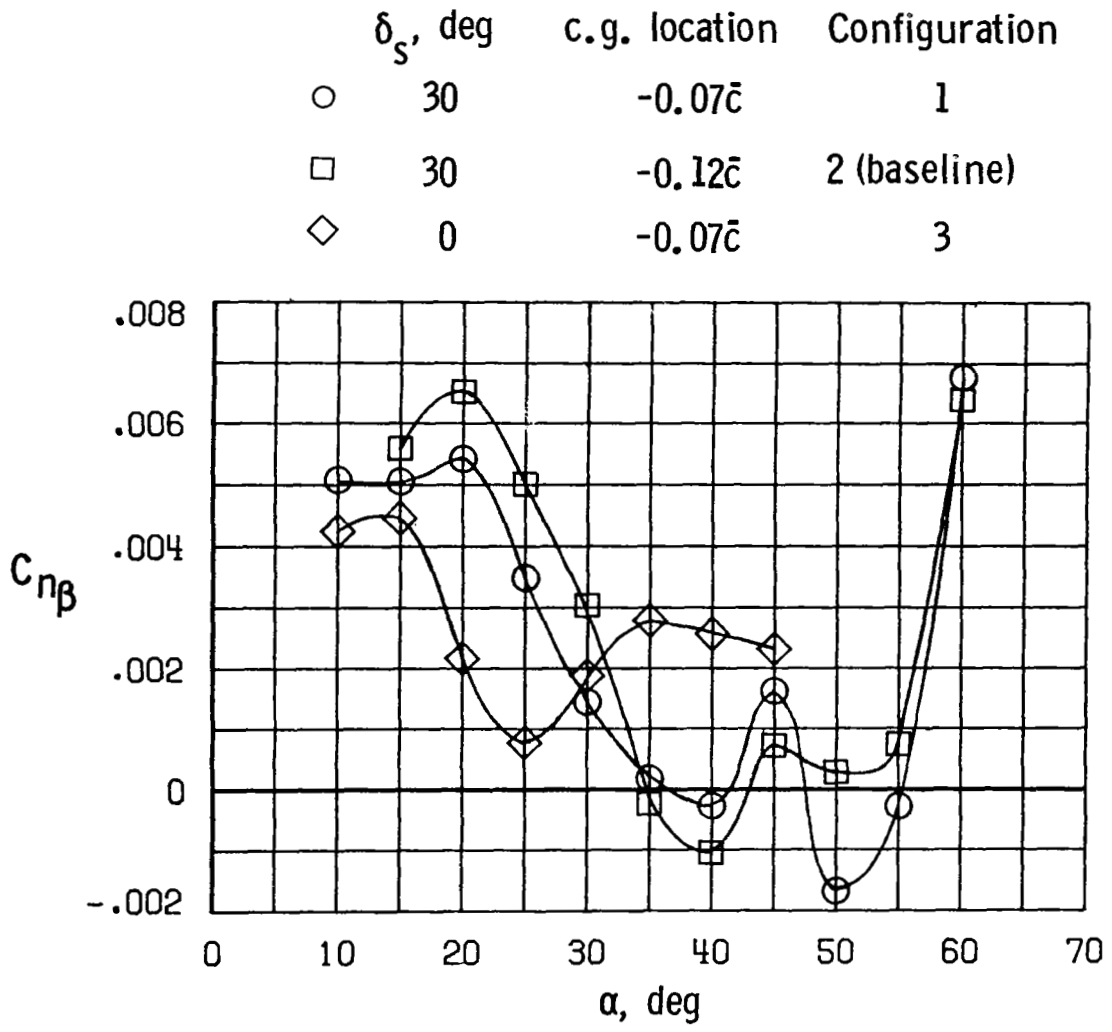

Figure 44.- Effect of strake-flap deflection and c.g. location on directional stability. δ_c = Trim; δ_f = 17.5°.

1. Report No.	2. Government Accession No.	3. Recipient's Catalog No.
NASA TP-2230		

4. Title and Subtitle	5. Report Date
WIND-TUNNEL FREE-FLIGHT INVESTIGATION OF A MODEL OF A FORWARD-SWEPT-WING FIGHTER CONFIGURATION	February 1984
	6. Performing Organization Code 505-43-13-01

7. Author(s)	8. Performing Organization Report No.
Daniel G. Murri, Luat T. Nguyen, and Sue B. Grafton	L-15602
	10. Work Unit No.
9. Performing Organization Name and Address	
NASA Langley Research Center Hampton, VA 23665	11. Contract or Grant No.
	13. Type of Report and Period Covered Technical Paper
12. Sponsoring Agency Name and Address	
National Aeronautics and Space Administration Washington, DC 20546	14. Sponsoring Agency Code

15. Supplementary Notes

16. Abstract

A wind-tunnel free-flight investigation was conducted to study the dynamic stability characteristics of a model of a forward-swept-wing fighter-airplane configuration at high angles of attack. Various other wind-tunnel techniques employed in the study included static- and dynamic- (forced-oscillation) force tests, free-to-roll tests, and flow-visualization tests. A unique facet of the study was the extreme level of static pitch instability (in excess of negative 32-percent static margin) inherent in the airframe design which precluded free-flight testing without stability augmentation in pitch. Results are presented which emphasize the high-angle-of-attack aerodynamics and the vehicle-component contributions to these characteristics. The effects of these aerodynamic characteristics on the high-angle-of-attack flying qualities of the configuration are discussed in terms of results of the wind-tunnel free-flight tests.

17. Key Words (Suggested by Author(s))	18. Distribution Statement
Forward-swept wing Relaxed static stability Dynamic stability Aircraft stability and control High angle of attack	Unclassified - Unlimited Subject Category 08

19. Security Classif. (of this report)	20. Security Classif. (of this page)	21. No. of Pages	22. Price
Unclassified	Unclassified	69	A04

For sale by the National Technical Information Service, Springfield, Virginia 22161 NASA-Langley, 1984

National Aeronautics and Space Administration

Washington, D.C.
20546

Official Business
Penalty for Private Use, $300

THIRD-CLASS BULK RATE

Postage and Fees Paid
National Aeronautics and Space Administration
NASA-451

U.S.MAIL

S I IJ,A, 840203 S00903DS
DEPT OF THE AIR FORCE
AF WEAPONS LABORATORY
ATTN: TECHNICAL LIBRARY (SUL)
KIRTLAND AFB NM 87117

NASA

POSTMASTER: If Undeliverable (Section 158 Postal Manual) Do Not Return